Correlated Nuclear and Electronic Dynamics in Photoionized Systems studied by Quantum and Mixed Quantum-Classical Approaches

Dissertation zur Erlangung des Doktorgrades des Fachbereiches Physik der Universität Hamburg

vorgelegt von

Zheng Li

aus

Chongqing

Hamburg

2014

Gutachter der Dissertation:	Dr. Oriol Vendrell Prof. Dr. Daniela Pfannkuche
Gutachter der Disputation:	Prof. Dr. Wilfried Wurth Prof. Dr. Michael Rübhausen Prof. Dr. Gabriel Bester
Datum der Disputation:	25.08.2014
Vorsitzender des Fach-Promotionsausscuhsses:	Prof. Dr. Michael Rübhausen
Leiter des Fachbereiches Physik:	Prof. Dr. Peter Hauschildt
Dekan der Fakultät für Mathematik, Informatik und Naturwissenschaften:	Prof. Dr. Heinrich Graener

Für meine Eltern und meine Familie

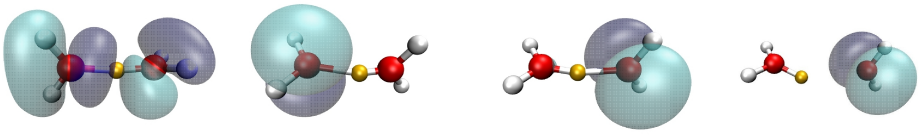

0 fs 3 fs 8 fs 30 fs

Electron hole in motion: The electron hole (blue and green surfaces) is created by extreme ultraviolet (XUV) radiation of free electron laser FLASH. Because of the repulsion between the electron hole and the proton (orange sphere), the molecule undergoes Coulomb explosion via non-Born-Oppenheimer mechanism.

Zusammenfassung

Das Aufkommen der Freie-Elektronen-Laser und hohe Harmonische Lichtquellen ermöglicht die Untersuchung der Elektronen- und Kerndynamik in Atomen, Molekülen und Festkörpern mit atomarer (räumlich) und Femtosekunden/Attosekunden (zeitlich) Auflösung. Dank der ultrahellen und ultrakurzen Lichtpulsen im Frequenzbereich von Terahertz bis harte Röntgenstrahlung, können Kern- und Elektronendynamiken im Zeitbereich von Femto- bis Attosekunden initiiert, beobachtet und kontrolliert werden. Es bedarf theoretischer Modelle, um die zugrunde liegenden Mechanismus zu beschreiben.

Diese Doktorarbeit beschäftigt sich mit der Entwicklung von theoretischen Modellen, die auf quantenmechanischer *multiconfiguration time–dependent Hartree* (MCTDH) und gemischter quanten-klassischer Methode beruhen. Diese Modellen werden zur Beschreibung der Dynamik der gasförmigen Moleküle und des stark korrelierten Elektronensystems in der Gegenwart von ultrakurzen Lichtpulsen verwendet.

Im ersten Teil dieser Arbeit liegt der Fokus auf der Bewegung der Elektronlöcher in gasförmigen molekularen Ionen, die durch Photoionisation extremer Ultraviolettstrahlung (XUV) entstehen, und mittels spektroskopischen Ansätzen beobachtet werden. Die XUV–Photonen erzeugen Elektronloch in den Valenzorbitalen, das Elektronloch, als ein positiv gelandenes Quasi–Teilchen, steht in Wechselwirkung mit den Kernen und den übringen Elektronen, und führt anschließlich zu gekoppelter Nicht–Born–Oppenheimer-Dynamik.

Basierend auf Quantenwellenpaket und gemischter quanten-klassischer Ansätze, studiere ich die Relaxationdynamik des Elektronlochs in Valenzionisierten molekularen Ionen von kleiner und mittlerer Größe. Anhand der molekularen Ionen $\left[H^+(H_2O)_n\right]^+$ zeigen wir, dass die gekoppelte Bewegeung der Elektronlöcher und Kerne mittels transienter Röntgenabsorptionsspektroskopie mit Auflösung von mehreren Femtosekunden ausgelesen werden kann. Außerdem können die XUV-Photonen in speziellen Fällen kohärentes Elektronloch erzeugen, das sein Kohärenz bis zur Zeitskala von *ca.* 1 Picosekunde behalten kann. Mittels der XUV Anregung – IR Abfrage Technik, kann man die kohärente Elektronloch–Bewegung in molekularen Ionen auflösen, und Quantenschwebung beobachten.

Im zweiten Teil studiere ich die Elektronendynamik im stark korrelierten Elektronensystem, die durch Anregung ultrakurzer Laserpulsen ausgelöst wird. Es wird mit Nachdruck an der Entwicklung eines effizienten Schemas für die Nichtgleichgewichts- dynamische molekulare Feld Theorie (DMFT) gearbeitet, die Elektronendynamik langer Zeit erfassen kann.

Alle diese Beispiele beruhen auf einem allgemeinem theoretischen Rahmen von zeitab-

hängiger Formulierung der Schrödingergleichung.

Abstract

The advent of free electron lasers and high harmonic sources enables the investigation of electronic and nuclear dynamics of molecules and solids with atomic spatial resolution and femtosecond/attosecond time resolution, using bright and ultrashort laser pulses of frequency from terahertz to hard x–ray range. With the help of ultrashort laser pulses, the nuclear and electronic dynamics can be initiated, monitored and actively controlled at the typical time scale in the femtosecond to attosecond realm. Meanwhile, theoretical tools are required to describe the underlying mechanism.

This doctoral thesis focuses on the development of theoretical tools based on full quantum mechanical multiconfiguration time–dependent Hartree (MCTDH) and mixed quantum classical approaches, which can be applied to describe the dynamical behavior of gas phase molecules and strongly correlated solids in the presence of ultrashort laser pulses.

In the first part of this thesis, the focus is on the motion of electron holes in gas phase molecular ions created by extreme ultraviolet (XUV) photoionization and watched by spectroscopic approaches. The XUV photons create electron-hole in the valence orbitals of molecules by photoionization, the electron hole, as a positively charged quasi–particle, can then interact with the nuclei and the rest of electrons, leading to coupled non-Born-Oppenheimer dynamics. I present our study on electron–hole relaxation dynamics in valence ionized molecular ions of moderate size, using quantum wave packet and mixed quantum–classical approaches, using photoionized $\left[H^+(H_2O)_n\right]^+$ molecular ion as example. We have shown that the coupled motion of the electron–hole and the nuclei can be mapped out with femtosecond resolution by core–level x–ray transient absorption spectroscopy. Furthermore, in specific cases, the XUV photon can create a coherent electron hole, that can maintain its coherence to time scales of ~ 1 picosecond. Employing XUV pump - IR probe spectroscopy, one can resolve coherent electron-hole motion in molecular ions, from which quantum beating can be observed.

In the second part of this thesis, I present our study on the electron dynamics of strongly correlated solids triggered by ultrashort laser pump. The effort is devoted to develop an efficient scheme for the nonequilibrium dynamical mean field theory (DMFT) that is able to accurately capture long time dynamics.

All these applications are treated within a general theoretical framework from time–dependent formulation of Schrödinger equation.

Contents

LIST OF PUBLICATIONS

2013 *"Correlated dynamics of the motion of proton-hole wave-packets in a photoionized water cluster"*
Z. Li, M. E. Madjet, O. Vendrell and R. Santra
Phys. Rev. Lett. **110**, 038302 (2013)

2013 *"Non-Born-Oppenheimer dynamics of the photoionized Zundel cation: A quantum wavepacket and surface-hopping study"*
Z. Li, M. E. Madjet and O. Vendrell
J. Chem. Phys. **138**, 094311 (2013);

2013 *"Ultrafast hydrogen migration in acetylene cation driven by non-adiabatic effect"*
M. E. Madjet, Z. Li and O. Vendrell
J. Chem. Phys. **138**, 094313 (2013)

2014 *"Dynamics of fluctuations in a quantum system"*
Y.-J. Chen, S. Pabst, Z. Li, O. Vendrell and R. Santra
Phys. Rev. A **89**, 052113 (2014)

2014 *"Core-level transient absorption spectroscopy as a probe of electron hole relaxation in photoionized* $H^+(H_2O)_n$ *"*
Z. Li, M. E. Madjet, O. Vendrell and R. Santra
Faraday Discussions **171** (2014)

2014 *"Coherent electron hole dynamics near a conical intersection"*
H. Timmers, Z. Li, N. Shivaram, R. Santra, O. Vendrell and A. Sandhu
Phys. Rev. Lett. **113**, 113003 (2014)

2014 *"Multiconfiguration time-dependent Hartree impurity solver for nonequilibrium dynamical mean-field theory"*
K. Balzer, Z. Li, O. Vendrell and M. Eckstein
Submitted

2014 *"Thermal and nonthermal melting of silicon under femtosecond free-electron laser pulse irradiation"*
N. Medvedev, Z. Li and B. Ziaja
Submitted

2014 *"Fragmentation dynamics of* $H^+(H_2O)_n$ *under XUV irradiation"*
Z. Li, M. E. Madjet and O. Vendrell
Manuscript in preparation

2014 *"Dynamics of glycine molecule with double valence electron holes"*
Z. Li, O. Vendrell and R. Santra
Manuscript in preparation

LIST OF DEVELOPED PROGRAMS

M-DMFT DMFT–MCTDH Interface Program

CoIn Program for Diabatization of Electronic Potentials

QDTK Co-developer for Mixed Quantum-Classical Molecular Dynamics Package

Chapter 1

Overview

The rapid technological progress of free electron lasers (FEL) and high harmonic generation (HHG) sources enables the investigation of electronic and nuclear dynamics of molecules and solids with bright and ultrashort laser pulses of frequency from terahertz to hard x–ray range.

The high energy XUV / x–ray photons with energy ranging from 0.01 to several tens of keV provide unique access to spatial resolution down to several Ångström (Å) on the atomic scale (1Å$\simeq$12 keV), due to their short de Broglie wavelength. The FEL and HHG sources producing high energy light pulses provide further access to temporal resolution down to attosecond–femtosecond (10^{-18}–10^{-15} s) time scales. With the help of ultrashort laser pulses, the nuclear and electronic dynamics can be initiated, monitored and actively controlled at the typical time scale in the femtosecond to attosecond realm.

This doctoral thesis focuses on developing theoretical tools and concepts based on full quantum mechanical multiconfiguration time–dependent Hartree (MCTDH) and mixed quantum classical approaches, which can be applied to describe the dynamical behavior of gas phase molecules and strongly correlated solids in the presence of ultrashort laser pulses.

Chapter 3 describes the dynamics of gas phase molecules in the presence of ultrashort extreme ultroviolet (XUV) laser pulses.

Specifically, this chapter is devoted to study the dynamics in molecules following photoionization. Photoionization is probably the most usual phenomena, when atoms and molecules are exposed to the XUV or x–ray radiation. A thorough understanding of the follow–up processes in the photoionized atoms and molecules is crucial to experiments studying them using x–ray or XUV light, for example, the x–ray imaging, crystallography,

or XUV / x–ray pump-probe experiments.

Besides, the photoionized molecules are a natural lab for studying charge transfer in the microscopic scale. Since charge transfer processes in molecules can be an essential ingredient for a wide scope of natural phenomena and applications, for example charge transport in molecular electronics, biological functions of proteins, it is definitely intriguing to study the molecular charge transfer using novel light sources, and make molecular movies in which the moving electron holes and protons are the actors.

The electron hole left by the ionized electron can be seen as a positively charged quasi particle, which can be driven to move in the molecule by other charged particles due to Coulomb force, e.g. protons, electrons or another electron hole, or by the dynamical correlation of electrons. Consider a single photoionization of an N-electron molecule: provided that the light pulse has sufficient spectral width to cover several electronic states, immediately after photoionization the remaining $N-1$ electrons in the molecule are no longer at an eigenstate, instead their wave function is a superposition of several $(N-1)$-electron states, and is by the principle of quantum mechanics non–stationary. The interplay of these $(N-1)$-electron states consequently leads to the effective motion of the electron hole within the molecule.

In Section 3.1 the ultrafast fragmentation of the Zundel cation $H^+(H_2O)_2$ after photoionization is studied by quantum-dynamics with the MCTDH method and by surface-hopping approaches. A picture emerges in which the correlated motion of the electron hole and the shared proton leads to localization of the two positively charged entities at opposite sides of the Zundel dication in less than 10 fs followed by Coulomb explosion. Electronic non-adiabatic effects play a crucial role in the fragmentation dynamics. The photoionization spectrum of the cluster between 20 to 24 eV is calculated quantum-dynamically and its features explained. Two- and three-body fragmentation channels accessible by outer-valence ionization are also calculated and the branching ratios as a function of ionization energy are discussed. A good agreement between the quantum-dynamical treatment and surface-hopping is obtained for observables for which both methods are applied.

Section 3.2 addresses a fundamental request of experimentally monitoring the coupled nuclear and electronic dynamics associated to charge transfer processes in complex molecules and materials, with transient x-ray absorption spectroscopy

We study the dynamics of an electron hole created by photoionization in the valence states of protonated water clusters and its anti-correlated motion with the proton in the hydrogen bond network, due to the intrinsic Coulomb repulsion. We show that key aspects of the electron hole dynamics can be mapped to core level transient x-ray absorption spectra with femtosecond resolution.

Chapter 4 deals with a slightly different scenario for electron hole dynamics, in which the electron hole is electronically coherent. In this chapter, I will present the joint experimental theoretical study on the real-time evolution of a long-lived coherent electron hole following valence ionization of a molecule, which remains an unexplored facet of the charge transfer phenomena. Here we investigate the coherent motion of an electron hole wavepacket created near a conical intersection in photoionized CO_2. We resolve the oscillation of the electron hole density between σ and π character, driven by the coupled bending and asymmetric stretch vibrations of the molecule. We quantify the mixing between electron hole states and find that the degree of electronic coherence decreases with time due to rotational thermal dephasing. Our results demonstrate the sensitivity of ultrafast XUV spectroscopy in probing the inner workings of coherent charge migration dynamics occurring in nature.

In Chapter 5, I present the study of electron dynamics in strongly correlated solids by pump–probe technique, which can reveal profound features of many–body electronic system occuring in real time, e.g. the emergence of quasi–particles on femtosecond time scale. Besides, the solids pumped by laser can exhibit intriguing properties and hidden phases in nonequilibrium state, which are not manifested in equilibrium. For example, one can induce insulator–metal transition or superconductor phase transition using ultrashort laser pulses.

The strongly correlated solids itself are also intriguing systems, in which the Coulomb correlation between electrons dominates the electronic interactions. Due to the pronounced many–body effects in the strongly correlated solids, their electronic structure cannot be correctly described by energy band theory based on independent particle picture. Moreover, the concept of strongly correlated solids cover a wide scope of materials of fundamental and practical importance, for example the Mott insulators and high-T_c superconductors. Thus, there is a persistent effort in the past decade devoted to understand the physical nature of this family of materials.

The dynamical mean field theory is a state-of-the-art framework that is aimed at solving the electronic structure of strongly correlated solids beyond the independent particle picture of energy band theory.

Our effort is devoted to developing an efficient scheme based on multiconfiguration time–dependent Hartree (MCTDH) method to bring nonequilirbium dynamical mean field theoretical description of strongly correlated electron dynamics in solids to a long time scale, which is crucial to the simulation of experiments that use ultrashort laser pulses to study the strongly correlated solids.

Chapter 2

Introduction to Theoretical Framework

In this chapter, I present the theoretical framework that serves as a basis for the study of coupled electron–nuclei dynamics of gas phase molecules and strongly correlated solids in the presence of ultrashort laser pulses.

For time–independent Hamiltonians, the time–dependent and time–independent formulation of quantum mechanics can be seen as equivalent and dual pictures connected by Fourier transformation. However, in the case where an enormous number of eigenstates is involved, time–dependent approaches can be advantageous, because one can avoid to explicitly solve the wave functions of these eigenstates. Instead, one can treat them conveniently in the wave packet pictures, as one can simultaneously pack these eigenstates in a single wave packet [1]. In case if the system is exposed to strong time-dependent perturbations, for example the system is pumped by a laser pulse, time-dependent treatment becomes indispensable. Besides, the time-dependent formulation of quantum mechanics also offers a more straightforward connection to classical mechanics.

In the present work, the time–dependent formalism is chosen preferably to study the molecular and electronic dynamics in gas phase molecules and solids with strong electron correlations. For this purpose the multiconfiguration time–dependent Hartree (MCTDH) and non–adiabatic surface hopping approaches are applied to solve the dynamical problems quantum mechanically and quantum–classically. The MCTDH and surface hopping methods are introduced in Section 2.2 and 2.3 respectively. Both methods are applied to simulate the molecular systems with non–Born–Oppenheimer electron–nuclei dynamics, which I present in Secton 2.1.

2.1 Non-Born-Oppenheimer dynamics

To give a brief introduction to non–Born–Oppenheimer dynamics, one could start from the factorized electronic and nuclear wave function of the molecule for the given full molecular Hamiltonian,

$$\begin{aligned} H(\mathbf{q},\mathbf{Q}) &= -\sum_a \frac{1}{2M_a}\nabla_a^2 - \frac{1}{2m}\sum_i \nabla_i^2 \\ &+ \sum_{j>i}\frac{1}{|\mathbf{q}_i-\mathbf{q}_j|} - \sum_{ai}\frac{Z_a}{|\mathbf{Q}_a-\mathbf{q}_i|} + \sum_{a>b}\frac{Z_aZ_b}{|\mathbf{Q}_a-\mathbf{Q}_b|} \\ &= T_{\mathrm{N}} + V_{\mathrm{e}} + V_{\mathrm{ee}} + V_{\mathrm{eN}} + V_{\mathrm{NN}}\,, \end{aligned} \tag{2.1}$$

where $\mathbf{q}$ and $\mathbf{Q}$ are the electronic and nuclear coordinates, m and M_a are the electronic and nuclear masses, respectively. The full molecular Hamiltonian can be written in the form of a sum of the nuclear kinetic energy and the rest terms as *electronic Hamiltonian*.

$$H_{\mathrm{mol}} = \frac{1}{2}\nabla_Q^2 + H_{\mathrm{e}} = T_{\mathrm{N}} + H_{\mathrm{e}}\,. \tag{2.2}$$

where $\vec{\nabla}_Q$ is the mass weighted nuclear gradient over all nuclear coordinates, T_{N} is the nuclear kinetic energy operator and $H_{\mathrm{e}} = V_{\mathrm{e}}+V_{\mathrm{ee}}+V_{\mathrm{eN}}+V_{\mathrm{NN}}$ is the electronic Hamiltonian.

In the original formulation of M. Born and R. Oppenheimer [2, 3], the molecular wave function is factorized as

$$\Psi(\mathbf{q},\mathbf{Q}) = \sum_n \chi_n(\mathbf{Q})\varphi_n(\mathbf{q},\mathbf{Q}), \tag{2.3}$$

where n is the index of electronic states.

In the case the basis functions $\{\varphi_n(\mathbf{q},\mathbf{Q})\}$ form a complete set of eigenfunctions for the electronic Hamiltonian H_{e}, i.e. $\{\varphi_n(\mathbf{q},\mathbf{Q})\}$ satisfy electronic Schrödinger equation

$$H_{\mathrm{e}}\varphi_n(\mathbf{q},\mathbf{Q}) = V_n(\mathbf{Q})\varphi_n(\mathbf{q},\mathbf{Q})\,, \tag{2.4}$$

and completeness condition

$$\begin{aligned} \langle\varphi_m|\varphi_n\rangle &= \delta_{mn} \\ \sum_n |\varphi_n\rangle\langle\varphi_n| &= 1\,, \end{aligned} \tag{2.5}$$

the set of basis functions $\{\varphi_n(\mathbf{q},\mathbf{Q}),\chi_n(\mathbf{Q})\}$ defines a closed representation for any given molecular wave function $\Psi(\mathbf{q},\mathbf{Q})$, which is called the *adiabatic representation*.

Using Eq. 2.3 and 2.4, we have the Schrödinger equation for nuclei in the adiabatic representation, which we use to simulate photoionized molecules in chapter 3, and that describes the nuclei in a manifold of coupled electronic states,

$$\left[T_{\mathrm{N}}(\mathbf{Q}) + V_m(\mathbf{Q})\right] \chi_m(\mathbf{Q}) + \sum_n \Lambda_{mn}(\mathbf{Q}) \chi_n(\mathbf{Q}) = E \chi_m(\mathbf{Q}) \,, \tag{2.6}$$

where the kinetic non–Born–Oppenheimer coupling Λ_{mn} couples different states $|\varphi_m\rangle$ and $|\varphi_n\rangle$ via nuclear gradient $\vec{\nabla}_Q$,

$$\begin{aligned} \Lambda_{mn}(\mathbf{Q}) &= -\left\langle \varphi_m \left| \vec{\nabla}_Q \right| \varphi_n \right\rangle \cdot \vec{\nabla}_Q + \frac{1}{2} \left\langle \varphi_m \left| \nabla_Q^2 \right| \varphi_n \right\rangle \\ &= -\vec{\Lambda}^{(1)}_{mn} \cdot \vec{\nabla}_Q + \frac{1}{2} \Lambda^{(2)}_{mn} \,. \end{aligned} \tag{2.7}$$

Setting $\Lambda_{mn} = 0$ defines the Born–Oppenheimer approximation, which could be analogously viewed as assuming frictionless motion of nuclei in the electron cloud. One can easily observe this fact, because the leading term describing non–Born–Oppenheimer electron–nuclei coupling in the Hamiltonian ,$-\left\langle \varphi_m \left| \vec{\nabla}_Q \right| \varphi_n \right\rangle \cdot \vec{\nabla}_Q$, is proportional to momentum of nuclei $\mathbf{P} = -i\vec{\nabla}_Q$, namely proportional to the velocity of nuclei $\mathbf{v}_Q$, such that

$$-\left\langle \varphi_m \left| \vec{\nabla}_Q \right| \varphi_n \right\rangle \cdot \vec{\nabla}_Q = \gamma_{\mathrm{f}}(\mathbf{Q}) \cdot \mathbf{v}_Q \,, \tag{2.8}$$

which is classically a non–conservative term describing friction between electrons and nuclei in the formalism of non–canonical Hamiltonian mechanics [4], and $\gamma_{\mathrm{f}}(\mathbf{Q})$ is a molecular geometry dependent friction coefficient.

As stated by Born and Oppenheimer in their seminal literature [2], the ratio of excitation energies for electronic and nuclear degrees of freedom has the order of $\mathcal{O}(10^2)$, thus the nuclear excitation can be approximately decoupled from electronic excitations, i.e. their motions are decoupled, and the term Λ_{mn} inducing electronic transitions with nuclear motion can be accordingly neglected in many cases. One can readily see this by comparing the typical electronic, vibrational and rotational energy scales, which lie in the ultraviolet ($\sim$ 10 eV), infrared ($\sim$ 100 meV) and far–infrared ($\sim$ 1 meV) regimes respectively. From dimension analysis, one can find the relation $E_{\mathrm{vib}} \simeq \sqrt{\frac{m}{M}} E_{\mathrm{e}} \simeq 10^{-2} E_{\mathrm{e}}$ and $E_{\mathrm{rot}} \simeq \frac{m}{M} E_{\mathrm{e}} \simeq 10^{-4} E_{\mathrm{e}}$, with $\frac{m}{M} \sim \mathcal{O}(10^{-4})$ being the electron nucleus mass ratio, because

$$\begin{aligned} E_{\mathrm{vib}} &= \hbar\omega \simeq \sqrt{\frac{1}{mM}} \frac{\hbar^2}{a^2} \\ E_{\mathrm{rot}} &= \frac{\hbar^2 j^2}{2I} \simeq \frac{\hbar^2}{2Ma^2} \\ E_{\mathrm{e}} &\simeq \frac{\hbar^2}{ma^2} \,, \end{aligned} \tag{2.9}$$

where a is the length scale of a molecule, the playground for nuclei and electrons.

However, the electrons and nuclei in nature are indeed coupled with each other, as they move simultaneously in the molecules. Especially, when two electronic states come close, or degenerate due to molecular symmetry, the coupling between electrons and nuclei can become so large or even infinite, that the kinetic energy of the nuclei can excite the electronic degrees of freedom. It is easy to observe this fact, since the derivative coupling term can be recast in the form using Hellmann Feynman theorem [5],

$$\vec{\Lambda}^{(1)}_{mn} = \left\langle \varphi_m \left| \vec{\nabla}_Q \right| \varphi_n \right\rangle = \frac{\left\langle \varphi_m \left| \vec{\nabla}_Q H_{\mathrm{e}} \right| \varphi_n \right\rangle}{V_n - V_m}, \text{ for } m \neq n \tag{2.10}$$

and it diverges if $V_n = V_m$, i.e. when the n-th and m-th electronic states are degenerate, the Hamiltonian in adiabatic represention is singular. In this case, one has to include the Λ_{nm} coupling, which introduces nuclear motion mediated electronic transition, namely the non–Born–Oppenheimer effect. The non-adiabatic energy transfer between nuclear and electronic systems is absent in the Born–Oppenheimer approximation.

In this thesis, non–Born–Oppenheimer effect is incorporated as an essential ingredient of all *ab initio* simulation, because one could find that the non–Born–Oppenheimer effect can manifest itself significantly in the highly excited molecular ions containing electron holes produced by photoionisation. Without incorporating the non–Born–Oppenheimer effect, the results from *ab initio* simulation can be qualitatively incorrect, as I will present in chapter 3.

For this purpose, one has to properly handle the singularities appearing in the non–Born–Oppenheimer Hamiltonian (Eq. 2.10) in the adiabatic representation. A well established technique to remove the singularities in the non–Born–Oppenheimer Hamiltonian is the so-called *diabatization scheme* [5].

The diabatization procedure can be schematically viewed as a linear rotation U of nuclear basis functions $\{\chi_n(\mathbf{Q})\}$ subject to the Born–Oppenheimer factorization *ansatz* (Eq. 2.3) $\Psi(\mathbf{q},\mathbf{Q}) = \sum_{n=1}^{N} \chi_n(\mathbf{Q})\varphi_n(\mathbf{q},\mathbf{Q})$ to a new set of nuclear basis functions $\{\eta_n(\mathbf{Q})\}$ as,

$$\chi = U\eta\,, \tag{2.11}$$

where $\chi = (\chi_1, \cdots, \chi_N)^T$ and $\eta = (\eta_1, \cdots, \eta_N)^T$. Replacing Eq. 2.11 into the Schrödinger equation (Eq. 2.6), one finds

$$\begin{aligned} - & \frac{1}{2} U \nabla_Q^2 \eta - (\vec{\nabla}_Q U + \vec{\Lambda}^{(1)} U) \cdot \vec{\nabla}_Q \eta \\ + & \left[VU - \frac{1}{2} \left(\nabla_Q^2 U + 2\vec{\Lambda}^{(1)} \cdot \vec{\nabla}_Q U + \Lambda^{(2)} U \right) \right] \eta = EU\eta\,. \end{aligned} \tag{2.12}$$

As we know from Eq. 2.10, that $\vec{\Lambda}^{(1)}$ in the second term on the left hand side of Eq. 2.12 is diverging at the conical intersection. With the linear rotation U, one can readily remove this singularity by choosing specific nuclear coordinate $\mathbf{Q}$–dependent local transformation matrices $U(\mathbf{Q})$, such that the second term in Eq. 2.12 vanishes [6], i.e.

$$\vec{\nabla}_Q U(\mathbf{Q}) + \vec{\Lambda}^{(1)} U(\mathbf{Q}) = 0\,. \tag{2.13}$$

Such a local $\mathbf{Q}$–dependent transformation $U(\mathbf{Q})$ is called *diabatization transformation*, and the new set of nuclear basis $\{\eta_n(\mathbf{Q})\}$ spans the *diabatic representation*.

It has been shown [7] that Eq. 2.13 has non–trivial solution $U(\mathbf{Q})$, which guarantees that the diabatization transformation is well defined. Moreover, one can further show that the term $\frac{1}{2}\left(\nabla_Q^2 + 2\vec{\Lambda}^{(1)} \cdot \vec{\nabla}_Q + \Lambda^{(2)}\right) U = \frac{1}{2}\left(\vec{\nabla}_Q + \vec{\Lambda}^{(1)}\right)^2 U$ in Eq. 2.12 should also vanish, provided the diabatization condition (Eq. 2.13) is satisfied. Inserting Eq. 2.13 into Eq. 2.12, one could readily find

$$\left[-\frac{1}{2} U \nabla_Q^2 + VU\right] \eta = EU\eta\,. \tag{2.14}$$

It is straightforward to show that the diabatization transformation matrix U is orthogonal [7], because $\vec{\Lambda}^{(1)\dagger} = -\vec{\Lambda}^{(1)}$, we have

$$\begin{aligned} \vec{\nabla}_Q U + \vec{\Lambda}^{(1)} U &= 0 \\ \vec{\nabla}_Q U^\dagger - U^\dagger \vec{\Lambda}^{(1)} &= 0\,. \end{aligned} \tag{2.15}$$

From Eq. 2.15 one finds

$$U^\dagger \vec{\nabla}_Q U + (\vec{\nabla}_Q U^\dagger) U = \vec{\nabla}_Q (U^\dagger U) = 0\,, \tag{2.16}$$

thus $U^\dagger U = C$, where C is a constant. Given a normalization factor $1/\sqrt{C}$ to U, one can have a unitary diabatization matrix U, such that the *Schrödinger equation in diabatic representation* reads,

$$\left[-\frac{1}{2}\nabla_Q^2 + U^\dagger V U\right] \eta = E\eta\,. \tag{2.17}$$

Based on the discussion above, the coupled electronic nuclear Hamiltonian for molecules can be given as

$$\mathbf{H} = T_\mathrm{N}\mathbf{1} + \mathbf{W}\,, \tag{2.18}$$

where T_N is the nuclear kinetic energy operator (KEO) and $\mathbf{W}(\mathbf{Q}) = U^\dagger(\mathbf{Q}) V(\mathbf{Q}) U(\mathbf{Q})$ is the potential energy matrix in diabatic representation. The technical details to implement the diabatic transformation using a regularized diabatization scheme will also be presented in Section 3.1.2, with a concrete example of constructing a singularity–free

non–Born–Oppenheimer Hamiltonian for Zundel cation $H^+(H_2O)$. The regularized diabatization scheme we applied is a different strategy than directly solving Eq. 2.13, which is only practical for very small molecules.

With the singularity–free Hamiltonian in hand, the molecular system is in principle completely characterized, the key step forward is to solve the equations of motion associated with the molecular Hamiltonian, in order to retrieve the dynamics of electrons and nuclei of the molecule.

Before switching the topic to practical solutions of dynamics subject to the coupled electronic nuclear Hamiltonian of molecules, it is worth to mention the recent effort by E. K. U. Gross *et al.* [8, 9, 10], to construct singularity–free full molecular Hamiltonian without invoking the Born–Oppenheimer factorization *ansatz* (Eq. 2.3 and 2.4). Instead of using eigenfunctions $\{\varphi_n(\mathbf{q},\mathbf{Q})\}$ subject to electronic Hamiltonian H_e to expand the molecular wave function, the authors adopt a new set of basis functions $\{\Psi^N_\mathrm{mol}(\mathbf{q},\mathbf{Q})\}$, where $\Psi^N_\mathrm{mol}(\mathbf{q},\mathbf{Q})$ is the N-th eigenstate of the full molecular Hamiltonian H_mol (Eq. 2.2), such that $H_\mathrm{mol}\Psi^N_\mathrm{mol}(\mathbf{q},\mathbf{Q}) = E_N\Psi^N_\mathrm{mol}(\mathbf{q},\mathbf{Q})$. $\Psi^N_\mathrm{mol}(\mathbf{q},\mathbf{Q})$ can be factorized as a single product $\Psi^N_\mathrm{mol}(\mathbf{q},\mathbf{Q}) = \chi_N(\mathbf{Q})\Phi_N(\mathbf{q},\mathbf{Q})$, where $\Phi_N(\mathbf{q},\mathbf{Q})$ satisfies the partial normalization condition, $\int d\mathbf{q}\,|\Phi_N(\mathbf{q},\mathbf{Q})|^2 = 1$.

With the new *exact factorization ansatz*, the authors are able to show that the exact electronic wave functions $\Phi_N(\mathbf{q},\mathbf{Q})$ are perfectly smooth for any finite value of nuclear mass M, such that the Hamiltonian singularities appearing in the Born–Oppenheimer adiabatic representation occur only in the Born–Oppenheimer limit $M \to \infty$ [10], i.e. the electron nucleus mass ratio $\frac{m}{M} \to 0$, and the motion of electrons and nuclei is completely decoupled. It should be an attractive direction to develop novel theoretical schemes for non–Born–Oppenheimer dynamics based on the exact factorization representation [9].

The following Sections 2.2 and 2.3 are devoted to introduce the method I applied in my Ph.D. work to handle to the time–dependent Schrödinger equation, using quantum mechanical wave packet and mixed quantum–classical surface hopping approaches.

2.2 Multiconfiguration time-dependent Hartree

The MCTDH method [11, 12, 13], which we employ to simulate the non-Born-Oppenheimer electron–nuclei dynamics of molecular ions in chapter 3, and to solve the nonequilibrium DMFT impurity model for strongly correlated materials in chapter 5, is a general framework that provides highly efficient solutions to the time-dependent Schrödinger equation.

The MCTDH *ansatz* for the wave function can be written as

$$\begin{aligned}\Psi(q_1,\ldots,q_f,t) &\equiv \Psi(Q_1,\ldots,Q_p,t)\\ &= \sum_{j_1}^{n_1}\cdots\sum_{j_p}^{n_p} A_{j_1,\cdots,j_p}(t)\prod_{\kappa=1}^{p}\varphi_{j_\kappa}^{(\kappa)}(Q_\kappa,t)\\ &= \sum_{J} A_J\Phi_J, \end{aligned} \tag{2.19}$$

where f denotes the number of degrees of freedom and p the number of MCTDH combined modes. Combined modes are effective degrees of freedom containing several correlated coordinates, whose time–dependent basis functions are grouped together, and propagated in a multidimensional subspace which they belong to. Suppose a combined mode $Q_\kappa = \{q_{1_\kappa},\cdots,q_{d_\kappa}\}$ contains d_κ primitive coordinates q_{i_κ}, which is a subset of f degrees of freedom $\{q_1,\cdots,q_f\}$, the mode combined SPFs $\varphi_{j_\kappa}^{(\kappa)}(Q_\kappa,t)$ are given as a multiconfigurational expansion in terms of the time–independent primitive basis functions by

$$\varphi_{j_\kappa}^{(\kappa)}(Q_\kappa,t) = \sum_{i_{1_\kappa}}^{N_{1_\kappa}}\cdots\sum_{i_{d_\kappa}}^{N_{d_\kappa}} B_{j_\kappa;i_{1_\kappa}\cdots i_{d_\kappa}}^{(\kappa)}\chi_{i_{1_\kappa}}^{(\kappa,1)}(q_{1_\kappa})\cdots\chi_{i_{d_\kappa}}^{(\kappa,d_\kappa)}(q_{d_\kappa})\,. \tag{2.20}$$

Introducing combined modes helps to reduce effective degrees of freedom from f to p, with $p<f$, and provide access to rearrange correlated coordinates into groups of strongly coupled modes.

The key ingredient of the MCTDH *ansatz* is the introduction of time–dependent basis functions, denoted as $\varphi_{j_\kappa}^{(\kappa)}(Q_\kappa,t)$ in Eq. 2.19. In the *standard* TDSE method, which is developed since 1970's, the wave function is expanded directly with the time–independent primitive basis,

$$\Psi(q_1,\ldots,q_f,t) = \sum_{j_1}^{N_1}\cdots\sum_{j_f}^{N_f} A_{j_1,\cdots,j_f}(t)\prod_{\kappa=1}^{f}\chi_{j_\kappa}^{(\kappa)}(Q_\kappa)\,, \tag{2.21}$$

One can directly observe the improvement of MCTDH method compared to the *standard* TDSE method from the difference between Eq. 2.19 and Eq. 2.21. The improvement of MCTDH lies in two aspects. *Firstly*, in the standard method (Eq. 2.21) there are N_κ time–independent basis $\chi_{j_\kappa}^{(\kappa)}(Q_\kappa)$, for the κth degree of freedom, and in the MCTDH *ansatz* (Eq. 2.19) there are n_κ variationally optimal time–dependent basis, called single-particle functions (SPF). For the κth combined mode, as I will introduce in the following, the number of basis functions required to represent the time–dependent wave function is substantially smaller in MCTDH *ansatz* than that in the standard method, such that $n_\kappa \ll N_\kappa$. *Secondly*, the MCTDH *ansatz* has less degrees of freedom than that of the standard method, i.e. $p<f$, thanks to the mode combination.

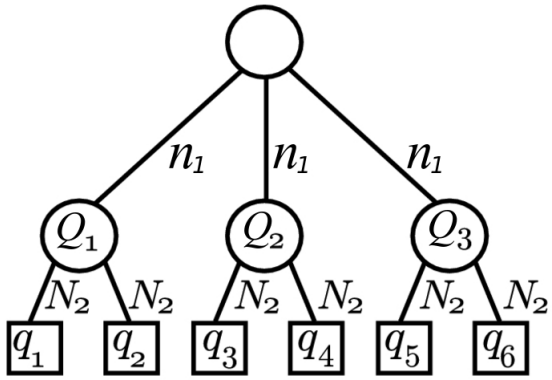

Figure 2.1: Tree structure of the MCTDH wavefunction of a system with 6 degrees of freedom, where q_i are the coordinates. The coordinates are combined in groups of two. N_2 refers to the number of time–independent primitive basis functions or grid points. n_1 is the number of the time–dependent basis, i.e. the single particle functions (SPFs), for each combined mode. This figure is taken from Ref. [15]. Copyright © 2011 American Institute of Physics (AIP).

The A-vector $A_J \equiv A_{j_1,\cdots,j_p}$ denotes the MCTDH expansion coefficients and the configurations Φ_J are products of the time-dependent SPFs. The SPFs are finally represented by linear combinations of time-independent primitive basis functions, which can be grid basis of various types. The contracted structure of the MCTDH wave function can be illustratively viewed with a tree diagram as sketched in Fig. 2.1 [14, 15]. In the tree diagram, the time-dependent wave function is represented by two layers of basis functions, the upper layer consists of time-dependent SPFs that can follow the wave function, and the bottom layer contains the support of static primitive basis functions, whose linear combinations represent the SPFs.

Fig. 2.2 illustrates how a moving two–particle correlated wave function $\Psi(x, y, t)$ is represented by the time–dependent basis (the SPFs) that follow it. Correlation of the wave function manifests itself by the fact that the wave function can only be represented by a sum of products of basis functions, instead of a single product of functions $\varphi_j(x,t)\varphi_k(y,t)$

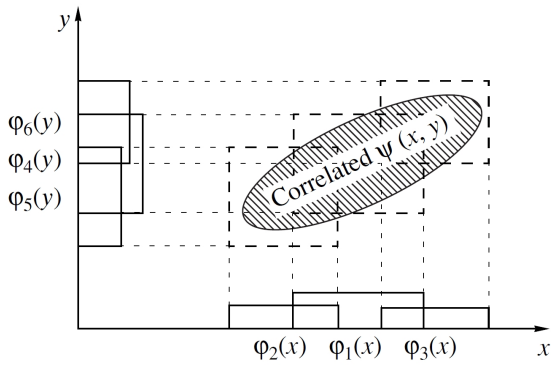

Figure 2.2: Representing a correlated wave function $\Psi(x, y)$ by covering its support with sum of products of single particle functions (SPFs) $\varphi_i(x)\varphi_j(y)$. Because the correlated $\Psi(x, y)$ is not aligned along the coordinate axes, several SPF products are required to cover its support. This figure is taken from Ref. [16]. Copyright © 2005 American Physical Society (APS).

in the uncorrelated case. Pictorially [16], the correlated wave function $\Psi(x,y,t)$ should not align along the coordinate axes, while the product functions $\varphi_j(x,t)\varphi_k(x,t)$ are always aligned with the axes. Several product functions are required to cover the support of $\Psi(x,y,t)$. In the dynamical problem, the wave function will change its position and shape in the (x,y) plane. The MCTDH philosophy is to let the time–dependent SPFs $\varphi(t)$ to variationally move as linear combination of the static primitive basis, in order to optimally cover the moving wave function $\Psi(t)$. Provided the correlation does not considerably increase, roughly the same number of temporally self–adjusted SPFs suffice during the entire time window of the relevant dynamics.

Following the pictorial sketch of MCTDH method above, one sees immediately the necessity to guide the time evolution of the time–dependent basis functions (SPFs), so that they can evolve in an optimal way to find and cover the support of the moving wave function. This task is done by the MCTDH equations of motion, which ensure the motion of time–dependent basis to be variationally optimal to follow the time–dependent wave function. The MCTDH equations of motion for expansion coefficients A_J and time–dependent SPF basis Φ_J are derived from the Dirac-Frenkel variation principle and read [11]

$$\begin{aligned} i\dot{A}_J &= \sum_L \langle \Phi_J \left| H \right| \Phi_L \rangle A_L \,, \\ i\dot{\varphi}^{(\kappa)} &= (1-P^{(\kappa)})(\rho^{(\kappa)})^{-1}\langle \mathbf{H} \rangle^{(\kappa)} \varphi^{(\kappa)} \,, \end{aligned} \tag{2.22}$$

where a vector notation, $\varphi^{(\kappa)} = (\varphi_1^{(\kappa)}, \cdots, \varphi_{n_\kappa}^{(\kappa)})^T$, is used. In Eq. 2.22, the projector $P^{(\kappa)}$ on the space spanned by the SPF for the κth degree of freedom is defined as,

$$P^{(\kappa)} = \sum_{j=1}^{n_\kappa} \left| \varphi_j^{(\kappa)} \right\rangle \left\langle \varphi_j^{(\kappa)} \right| . \tag{2.23}$$

It can be deduced that in the case $n_\kappa = N_\kappa$, namely the number of SPFs matches the number of the underlying primitive basis, the MCTDH equations of motion (Eq. 2.22) are reduced to that of standard TDSE method, since $P^{(\kappa)} = 1$ and $i\dot{\varphi}^{(\kappa)} = 0$.

By defining single–hole function $\Psi_l^{(\kappa)}$ as linear combination of Hartree products of $(f-1)$ SPFs without the SPFs for the κth degree of freedom Q_κ

$$\begin{aligned} \Psi_l^{(\kappa)} &= \sum_{j_1} \cdots \sum_{j_{\kappa-1}} \sum_{j_{\kappa+1}} \cdots \sum_{j_f} A_{j_1 \cdots j_{\kappa-1} l j_{\kappa+1} \cdots j_f} \\ &\quad \times \varphi_{j_1}^{(1)} \cdots \varphi_{j_{\kappa-1}}^{(\kappa-1)} \varphi_{j_{\kappa+1}}^{(\kappa+1)} \cdots \varphi_{j_f}^{(f)} , \end{aligned} \tag{2.24}$$

one can write the means–field $\langle H \rangle^{(\kappa)}$ and density matrix $\rho^{(\kappa)}$ in compact forms as,

$$\langle H \rangle_{jl}^{(\kappa)} = \left\langle \Psi_j^{(\kappa)} \right| H \left| \Psi_l^{(\kappa)} \right\rangle , \tag{2.25}$$

and

$$\rho_{jl}^{(\kappa)} = \left|\Psi_j^{(\kappa)}\right\rangle\left\langle\Psi_l^{(\kappa)}\right| = \sum_{j_1}\cdots\sum_{j_{\kappa-1}}\sum_{j_{\kappa+1}}\cdots\sum_{j_f} A^*_{j_1\cdots j_{\kappa-1}jj_{\kappa+1}\cdots j_f} A_{j_1\cdots j_{\kappa-1}lj_{\kappa+1}\cdots j_f}. \tag{2.26}$$

The computational gain of the MCTDH method is acquired via keeping the number of SPF basis optimally small compared to the underlying primitive basis, i.e., the so-called MCTDH contraction effect. Because the SPFs are variationally optimal as inherently guaranteed by the MCTDH equations of motion, they are ensured to evolve temporally in an optimal manner to represent the time-dependent wave function, intuitively the time-dependent SPF basis can follow the moving wave function. Therefore often a rather small number of SPFs allows for an accurate representation of wave packet. In comparison, the standard time-dependent Schrödinger equation (TDSE) method based on time-independent basis sets requires much more basis functions to cover the entire area in Hilbert space the wave function has explored during the whole dynamical process. Therefore, for Schrödinger equation of a system with f degrees of freedom, MCTDH leads to the scaling of number of configurations n^f, where n SPFs are used for each degrees of freedom. Although the exponential scaling of order f remains, but to much lower base n than the standard TDSE method using time–independent primitive basis functions, whose configuration space dimension scales on the order of N^f, with $N \gg n$. As I have discussed for the MCTDH *ansatz* (Eq. 2.19), the efficiency can be further enhanced by combining the several correlated degrees of freedom into physical modes Q_i. One obtains this way a smaller number of effective degrees of freedom $p < f$ in Eq. 2.22, leading to further reduction in the number of configurations, but the time–dependent basis functions that have to be propagated are multidimensional. It is favorable to find mode–combination schemes that provide an optimal balance between the computational effort of propagating the expansion coefficients of configurations, the A–vector, and the effort of propagating multidimensional SPFs. A natural solution to efficient propagation of multidimensional SPFs is to treat the multidimensional SPFs in Eq. 2.20 as a time–dependent wave function-like object, and expand the SPF further using time–dependent basis, instead of using time–independent primitive basis as in Eq. 2.20.The resulting scheme is called the multi–layer multiconfiguration time-dependent Hartree (ML-MCTDH) method [14, 15, 17], where the level of basis function expansion is dubbed the *layer*. The efficiency enhancement can be easily understood, because in the ML-MCTDH scheme, the mode combined multidimensional SPFs are themselves represented by the deeper layer of time–dependent basis functions, the additional configuration space dimension reduction can be readily deduced from the MCTDH contraction effect.

In a general framework, one can view the standard time-dependent Schrödinger equa-

tion (TDSE) method with time-independent basis functions as a single layer scheme, because the wave function is directly represented by the layer of static primitive basis functions. In a same manner, the MCTDH itself can be viewed as a 2–layer scheme, which consists of the time–independent primitive basis as bottom layer and one additional layer of time–dependent SPF basis. In this perspective, it is natural to understand that by adding layers of basis functions to the MCTDH representation, i.e. with the family of ML-MCTDH methods with more than two layers of basis functions, one can further enhance the efficiency of the method [14, 15, 17]. In an N-layer MCTDH scheme, the time-dependent wave function is represented by $N-1$ layers of time-dependent basis functions, such that the i-th layer serves the role as time–dependent and variationally optimal basis functions to support linear expansion of basis in the upper $(i-1)$-th layer, while finally supported by the N-th bottom layer of static primitive basis.

The solution of the MCTDH equations of motion demands an efficient evaluation of the mean fields at every time step. For this purpose we have employed the constant mean field (CMF) scheme [11], which allows us to update the mean field $\langle \mathbf{H} \rangle^{(\kappa)}$ only after a defined time step longer than the integration step. The CMF approximation is valid as long as the time-dependent Hamiltonian does not undergo considerable changes within the time interval on which the mean field is kept constant. For a time-dependent Hamiltonian, the CMF time step should be shorter than the temporal feature of the Hamiltonian. For time-independent Hamiltonian, a larger SPF orbital space generally allows longer CMF time steps, because the mean field does not vary less drastically in time.

Furthermore, to treat the coupled potential energy operator appearing in most molecular applications, the Hamiltonian is represented as a sum of products of single mode operators, via the `POTFIT` method [11, 18, 19], which allows to bring general electronic potentials into product form comprised of basis functions called *single-particle potentials* (SPPs). With the `POTFIT` procedure, the potential energy operator defined on the set of grid points $\left\{ Q_{i_\kappa}^{(\kappa)} \right\}$ for f degrees of freedom can be approximated with chosen a set expansion orders m_k as

$$V(Q_{i_1}^{(1)}, \cdots, Q_{i_f}^{(f)}) \simeq \sum_{j_1=1}^{m_1} \cdots \sum_{j_f=1}^{m_f} C_{j_1 \cdots j_f} v_{j_1}^{(1)}(Q_{i_1}^{(1)}) \cdots v_{j_f}^{(f)}(Q_{i_f}^{(f)}) \,. \tag{2.27}$$

The advantage of representing the Hamiltonian as a sum of products of single mode operators is to circumvent the multi–dimensional integration when evaluating the Hamiltonian matrix elements $\langle \Phi_J | \, H \, | \Phi_L \rangle$ and mean fields $\langle H \rangle_{jl}^{(\kappa)} = \left\langle \Psi_j^{(\kappa)} \middle| \, H \, \middle| \Psi_l^{(\kappa)} \right\rangle$. The direct evaluation of Hamiltonian matrix elements and mean fields requires f-fold and $(f-1)$-fold spatial integrations, respectively, which can rapidly hit the computational barrier.

Expressing the Hamiltonian in the single–particle operator product form as

$$H = \sum_{\kappa=1}^{f} h^{(\kappa)} + \sum_{r=1}^{s} c_r \prod_{\kappa=1}^{f} h_r^{(\kappa)} , \tag{2.28}$$

the Hamiltonian matrix elements and mean fields involve now only a set of 1-fold integrations, which can be efficiently evaluated. For example, using Eq. 2.28, one can readily find the expression of Hamiltonian matrix elements as

$$\langle \Phi_J | \, H \, | \Phi_L \rangle \;=\; \sum_{\kappa=1}^{f} \left\langle \varphi_{j_\kappa}^{(\kappa)} \right| h^{(\kappa)} \left| \varphi_{l_\kappa}^{(\kappa)} \right\rangle + \sum_{r=1}^{s} c_r \prod_{\kappa=1}^{f} \left\langle \varphi_{j_\kappa}^{(\kappa)} \right| h_r^{(\kappa)} \left| \varphi_{l_\kappa}^{(\kappa)} \right\rangle , \tag{2.29}$$

where $h^{(\kappa)}$ and $h_r^{(\kappa)}$ denote the single–particle operators building up the separable and correlated part of the Hamiltonian, respectively.

In most applications in molecular physics, the kinetic energy operator has normally the required form as Eq. 2.28, and the `POTFIT` procedure can transform the multidimensional electronic potential energy operator into the sum of single–particle operator products, as illustrated in Eq. 2.27. Explicitly, the operators $h^{(\kappa)}$ and $h_r^{(\kappa)}$ in Eq. 2.29 would correspond to kinetic energy operator $t^{(\kappa)}$ and single–particle potentials (SPPs) $v_{r_\kappa}^{(\kappa)}(Q_{i_\kappa}^{(\kappa)})$.

With the MCTDH machinery introduced above, one is allowed to access the coupled electronic nuclear dynamics of molecules of medium size with fully quantum mechanical description. However, for many molecules containing tens or even more atoms, the full quantum mechanical treatment is not within reach due to computational barrier. One has to invoke newtonian mechanics, in a classical or semi–classical manner, in order to study the dynamics of large molecules. The development in this direction leads to a family of mixed quantum–classical surface hopping approaches, as presented in the next section.

2.3 Mixed quantum-classical dynamics

The mixed quantum–classical scheme is based on the nuclear trajectories guided by newtonian equation, while the electronic forces on the nuclei are acquired by quantum mechanical treatment. The dynamical phase space distribution of the system can be approximately reconstructed from a swarm of trajectories, as sketched in Fig. 2.3

To determine the motion of nuclei according to newtonian equations, the key ingredient is the force on the nuclei, which should be acquired from *ab initio* electronic potentials in the mixed quantum–classical scheme. To establish the connection of quantum mechanical electronic potentials and classical force on the nuclei, the natural linker would be the Ehrenfest theorem and the *correspondence principle* of quantum mechanics.

2.3.1 From quantum to classical mechanics – the Ehrenfest theorem

The time derivative of expectation value of a given operator $\mathcal{O}$ reads,

$$\frac{d}{dt}\langle\mathcal{O}\rangle = \frac{1}{i\hbar}\langle[\mathcal{O}, H]\rangle + \left\langle\frac{\partial\mathcal{O}}{\partial t}\right\rangle . \tag{2.30}$$

For time-independent operators in Schrödinger picture, $\left\langle\frac{\partial\mathcal{O}}{\partial t}\right\rangle = 0$. Applying Eq. 2.30 to the position and momentum operators leads to the Ehrenfest theorem [20].

For the nuclei moving in the electronic potential $V(\mathbf{Q})$, the Hamiltonian of nuclear motion is simply given in terms of nuclear canonical coordinates $(\mathbf{Q}, \mathbf{P})$ in phase space,

$$H(\mathbf{Q}, \mathbf{P}, t) = \frac{\mathbf{P}^2}{2M} + V(\mathbf{Q}) . \tag{2.31}$$

Applying the Ehrenfest theorem, the *classical* force on the nuclei subject to the Newton's second law can be expressed in the quantum mechanical context as,

$$\frac{d}{dt}\langle\mathbf{P}\rangle = \frac{1}{i\hbar}\langle[\mathbf{P}, H]\rangle = \frac{1}{i\hbar}\langle[\mathbf{P}, V(\mathbf{Q})]\rangle ,$$

given $\mathbf{P} = -i\hbar\vec{\nabla}_Q$ and nuclear wave function $|\chi\rangle$, evaluating the commutator in the right-hand side of Eq. 2.32 gives the expression of force $\mathbf{F}$ on the nuclei,

$$\begin{aligned}\frac{d}{dt}\langle\mathbf{P}\rangle &= \langle\chi|V(\mathbf{Q})|\vec{\nabla}_Q\chi\rangle - \langle\chi|\vec{\nabla}_Q(V(\mathbf{Q})|\chi\rangle) \\ &= -\langle\chi|(\vec{\nabla}_Q V(\mathbf{Q}))|\chi\rangle \\ &= -\left\langle\vec{\nabla}_Q V(\mathbf{Q})\right\rangle = \langle\mathbf{F}\rangle ,\end{aligned} \tag{2.32}$$

meanwhile

$$\begin{aligned}\frac{d}{dt}\langle\mathbf{Q}\rangle &= \frac{1}{i\hbar}\langle[\mathbf{Q}, H]\rangle \\ &= \frac{1}{i\hbar}\left\langle\left[\mathbf{Q}, \frac{\mathbf{P}^2}{2M}\right]\right\rangle = \frac{1}{M}\langle\mathbf{P}\rangle\end{aligned} \tag{2.33}$$

closes the derivation of the Ehrenfest theorem.

It is worth to note the conceptual transition from classical to quantum realm illustrated by the Ehrenfest theorem [1, 21, 22]. Despite the similarity, Eq. 2.32 does not necessarily describe particles that obey Newton's second law. A complete classical analogy of Newton's second law for a specific coordinate component should read,

$$\frac{d}{dt}\langle P_i\rangle = -\frac{\partial\langle V(\mathbf{Q})\rangle}{\partial\langle Q_i\rangle} , \tag{2.34}$$

instead of given in quantum mechanics as in Eq. 2.32, which states

$$\frac{d}{dt}\langle P_i\rangle = -\left\langle \frac{\partial V(\mathbf{Q})}{\partial Q_i}\right\rangle . \tag{2.35}$$

Obviously the relation

$$\frac{\partial \langle V(\mathbf{Q})\rangle}{\partial \langle Q_i\rangle} = \left\langle \frac{\partial V(\mathbf{Q})}{\partial Q_i}\right\rangle \tag{2.36}$$

does not necessarily hold, unless the wave function of the particle corresponds to a function of single point support in phase space, namely, one assumes a classical point particle.

To illustrate this fact, one could take one-dimensional model Hamiltonian with potential

$$V(Q) = \frac{1}{n}kQ^n, \tag{2.37}$$

as an example. It is easy to show that for a harmonic potential with $n = 2$, one has

$$\left\langle \frac{\partial V(Q)}{\partial Q}\right\rangle = k\langle Q\rangle = \frac{\partial \langle V(Q)\rangle}{\partial \langle Q\rangle}, \tag{2.38}$$

Ehrenfest theorem gives *almost* Newton's second law despite of the uncertainty relation between position and momentum. Such a quantum-classical particle corresponds to the coherent state wave packet introduced by E. Schrödinger [23], in order to establish the transition from quantum to classical mechanics. The coherent state, with minimum uncertainty $\Delta Q\Delta P = \hbar/2$, is a quantum state that is closest to a classical state. However for $n > 2$, Eq. 2.36 does not generally hold, e.g. for $n = 3$, one finds that

$$\begin{aligned} \left\langle \frac{\partial V(Q)}{\partial Q}\right\rangle &= k\langle Q^2\rangle \\ \frac{\partial \langle V(Q)\rangle}{\partial \langle Q\rangle} &= k\langle Q\rangle^2 . \end{aligned} \tag{2.39}$$

It is clear that in quantum mechanics $\langle Q^2\rangle = \langle Q\rangle^2$ does not necessarily hold, it is only valid if the wave function reduces to a function of single point support in the phase space, namely with zero uncertainty. It implies that quantum and classical mechanics meet at the limit of $\hbar \to 0$, or equivalently of large quantum number $n \to \infty$, since Bohr's quantization condition assumes the product of n and $\hbar$ is fixed at an appropriate classical action such that $n\hbar = S$, e.g. for electron in the hydrogen atom $n\hbar = J$, where J is the angular momentum of the electron.

For a general potential $V(Q)$, one can expand $V(Q)$ at the center of the wave packet $Q = \langle Q\rangle$, denoting $\Delta Q = Q - \langle Q\rangle$, one has

$$\frac{\partial V}{\partial Q} = \frac{\partial V(Q)}{\partial \langle Q\rangle} + \Delta Q\frac{\partial^2 V(Q)}{\partial \langle Q\rangle^2} + \frac{1}{2}\Delta Q^2\frac{\partial^3 V(Q)}{\partial \langle Q\rangle^3} + \cdots . \tag{2.40}$$

Because $\langle \Delta Q \rangle = \langle Q - \langle Q \rangle \rangle = \langle Q \rangle - \langle Q \rangle = 0$, one finds

$$\left\langle \frac{\partial V}{\partial Q} \right\rangle = \frac{\partial V(Q)}{\partial \langle Q \rangle} + \frac{1}{2} \left\langle \Delta Q^2 \right\rangle \frac{\partial^3 V(Q)}{\partial \langle Q \rangle^3} + \cdots . \tag{2.41}$$

So the general condition for viewing Eq. 2.34 as analogue of classical newtonian equation, namely the Ehrenfest equation of motion $\langle F(Q) \rangle = \left\langle \frac{\partial V(Q)}{\partial Q} \right\rangle$ can be approximated by newtonian equation of motion $F(\langle Q \rangle) = -\frac{\partial V(Q)}{\partial \langle Q \rangle}$, is

$$\frac{\partial V(Q)}{\partial \langle Q \rangle} \gg \frac{1}{2} \left\langle \Delta Q^2 \right\rangle \frac{\partial^3 V(Q)}{\partial \langle Q \rangle^3} . \tag{2.42}$$

It is easy to find the condition in Eq. 2.42 holds for potential $V(Q) = \frac{1}{2} Q^2$, because in this case $\frac{\partial^3 V}{\partial Q^3} = 0$.

In a practical view, the Ehrenfest theorem can be seen as valid in the case if the size of the wave packet is smaller than the typical size on which the potential function changes. It guarantees that the expectation values of position and momentum follow approximately a classical trajectory.

2.3.2 Mixed quantum-classical dynamics

In the context of mixed quantum-classical dynamics, one treats the coupled electronic nuclear dynamics in molecules by solving the equations,

$$\begin{aligned} i \frac{\partial}{\partial t} \Psi(\mathbf{q}; \mathbf{Q}(t)) &= H_{\mathrm{e}} \Psi(\mathbf{q}; \mathbf{Q}(t)) \\ \mathbf{F} &= M \ddot{\mathbf{Q}}(t) , \end{aligned} \tag{2.43}$$

where $\mathbf{Q}(t)$ represents a classical trajectory of the nuclei. Assume the molecular wave function can be expanded with electronic eigenstates $\{|\varphi_j\rangle\}$

$$\Psi(\mathbf{q}; \mathbf{Q}(t)) = \sum_j C_j(t) \varphi_j(\mathbf{q}; \mathbf{Q}(t)) , \tag{2.44}$$

inserting Eq. 2.44 into Eq. 2.43, and multiplying from the left by $\varphi_k^*(\mathbf{q}; \mathbf{Q}(t))$ one has

$$i \dot{C}_k(t) = \sum_l C_l(t) \left[H_{kl}(\mathbf{Q}(t)) - i \langle \varphi_k | \dot{\varphi}_l \rangle \right] , \tag{2.45}$$

where $H_{kl} = \langle \varphi_k | H_{\mathrm{e}} | \varphi_l \rangle$. Using the chain rule $\frac{\partial}{\partial t} \equiv \frac{dQ}{dt} \frac{\partial}{\partial Q}$, Eq. 2.45 can be finally recast into

$$\begin{aligned} i \dot{C}_k(t) &= \sum_l C_l(t) \left[H_{kl}(\mathbf{Q}(t)) - i \langle \varphi_k | \frac{\partial}{\partial Q} | \varphi_l \rangle \dot{\mathbf{Q}} \right] \\ &= \sum_l C_l(t) \left[H_{kl}(\mathbf{Q}(t)) - i \mathbf{d}_{kl} \cdot \dot{\mathbf{Q}} \right] , \end{aligned} \tag{2.46}$$

where $\mathbf{d}_{kl} \equiv \langle\varphi_k| \frac{\partial}{\partial Q} |\varphi_l\rangle$. The non-adiabatic coupling matrix elements $\sigma_{JI} = \dot{\mathbf{Q}} \cdot \mathbf{d}_{JI} = \left\langle \phi_J \middle| \frac{\partial \phi_I}{\partial t} \right\rangle$ can be calculated numerically by a finite difference from the overlap of wave functions [24, 25, 26]

$$\sigma_{JI}(t + \Delta t/2) = \frac{1}{2\Delta t} \left[\langle \phi_J(t) | \phi_I(t + \Delta t) \rangle - \langle \phi_J(t + \Delta t) | \phi_I(t) \rangle \right] \tag{2.47}$$

with linear interpolation within an integration time step Δt.

The central task remaining to the mixed quantum–classical scheme is to efficiently evaluate the force $\langle \mathbf{F} \rangle$ from evolving molecular wave function $\Psi(\mathbf{q}; \mathbf{Q}(t))$, which depends on the molecular geometry $\mathbf{Q}(t)$ and electronic coordinates $\mathbf{q}$. This seemingly easy task is however not trivial at all, especially when multiple electronic states are involved in the coupled non–Born–Oppenheimer nuclear electronic dynamics. When a set of coupled electronic states $\{|\varphi_n\rangle\}$ are involved in the dynamics, one can express the force acting on nuclei in the adiabatic representation in terms of electronic density matrix ρ as

$$\begin{aligned} \langle \mathbf{F} \rangle &= -\langle \Psi | \vec{\nabla}_Q H_\mathrm{e}(\mathbf{q}, \mathbf{Q}(t)) | \Psi \rangle \\ &= -\sum_{kl} \rho_{kl} \langle \varphi_k | \vec{\nabla}_Q H_\mathrm{e} | \varphi_l \rangle \\ &= -\sum_{k} \rho_{kk} \vec{\nabla}_Q E_k + \sum_{kl} \rho_{kl} (E_k - E_l) \mathbf{d}_{kl} \,, \end{aligned} \tag{2.48}$$

with the relation

$$\begin{aligned} \vec{\nabla}_Q \langle \varphi_k | H_\mathrm{e} | \varphi_l \rangle &= \vec{\nabla}_Q E_l \delta_{kl} \\ &= \langle \varphi_k | \vec{\nabla}_Q H_\mathrm{e} | \varphi_l \rangle + \langle \vec{\nabla}_Q \varphi_k | \varphi_l \rangle E_l + \langle \varphi_k | \vec{\nabla}_Q \varphi_l \rangle E_k \\ &= \langle \varphi_k | \vec{\nabla}_Q H_\mathrm{e} | \varphi_l \rangle + (E_k - E_l) \mathbf{d}_{kl} \,, \end{aligned} \tag{2.49}$$

where E_k is the energy of k-th electronic eigenstate, and $\langle \vec{\nabla}_Q \varphi_k | \varphi_l \rangle = -\langle \varphi_k | \vec{\nabla}_Q \varphi_l \rangle$. Eq. 2.48 leads to a family of mixed quantum classical methods, dubbed Ehrenfest dynamics, which has been applied for nuclear dynamics of molecules [27], however it may not always give faithful description of coupled electronic nuclear dynamics.

The reason lies in the fact that in the Ehrenfest dynamics scheme one assumes the force can be evaluated as an averaged quantity from all electronic states during the entire dynamical process, which is adequate for solids, because the time scale for the electronic states to dephase is inverse proportional to the energy spacing between electronic states [28], i.e. the typical time scale τ_{ik} for two electronic states $|\varphi_i\rangle$ and $|\varphi_k\rangle$ to dephase from a superposition state is $\tau_{ik} \propto \frac{\hbar}{|V_{ii} - V_{kk}|}$.

In solids, the energy space between electronic states in the energy bands can be infinitely small, and all potential energy surfaces are with almost parallel geometry with each other,

which is on the line with the assumptions made in the Ehrenfest dynamics. However, in the molecular case, when the molecular geometry is beyond the region of electronic degeneracy, or conical intersection, the dephasing between the electronic states can rapidly occur on the femtosecond time scale, comparable to the dynamical process itself. Thus, although the force acting on the nuclei can be evaluated as an averaged quantity from all relevant electronic states, when the potentials of adjacent electronic states comes close or degenerate, e.g. in the vicinity of conical intersection, the nuclei of the molecule would however most of the time only experience the force given by a single electronic state wave function $\langle \mathbf{F} \rangle = -\langle \varphi_k | \vec{\nabla}_Q V(\mathbf{Q}) | \varphi_k \rangle$ at a certain time. A successful mixed quantum–classical scheme to evaluate the force acting on nuclei in the molecular case is the surface-hopping approach.

The fewest-switches surface hopping (FSSH) scheme is one of the most popular methodologies to treat quantum-classical non–Born–Oppenheimer dynamics in molecules [29]. The FSSH scheme generally keeps the number of switching between electronic states to be min-

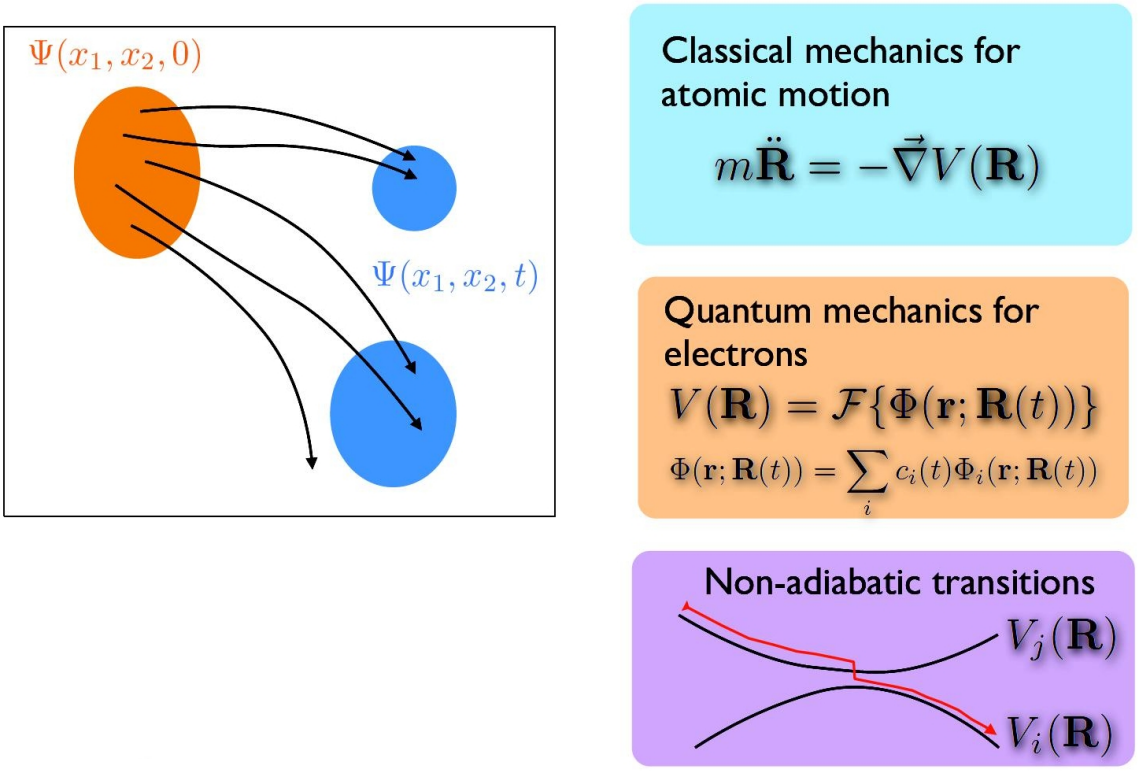

Figure 2.3: The sketch of the trajectory based mixed quantum–classical scheme. The time evolution of 2D model can be reconstructed from a swarm of trajectories, while the electronic potentials and the non–adiabatic switch of electronic states are described in an *ab initio* manner.

imal (hence, *fewest switches*), with the following probability g_{IJ} for the hopping from the I^{th} state to the J^{th} state within the time interval $[t, t+dt]$ [24],

$$g_{IJ}(t, t+dt) = -2\int_{t}^{t+dt} d\tau \frac{\Re\left[C_J(\tau)C_I^*(\tau)\dot{\mathbf{Q}}\cdot\mathbf{d}_{JI}\right]}{C_I^*(\tau)C_I(\tau)}\,. \tag{2.50}$$

Suppose ζ is a uniform random number between 0 and 1. A hopping event is invoked when the following inequality

$$\sum_{K\leq J-1} g_{IK}^{\alpha} < \zeta < \sum_{K\leq J} g_{IK}^{\alpha}\,, \tag{2.51}$$

as well as the energy conservation condition are satisfied. In our implementation of fewest-switches surface hopping scheme, the momentum of the nuclei are corrected immediately after the hopping by

$$\mathbf{p} \rightarrow \mathbf{p} + \mathbf{n}\left(\frac{\mathbf{n}M^{-1}\mathbf{p}}{\mathbf{n}M^{-1}\mathbf{n}}\right)\left(1 - \sqrt{1 - 2\Delta E\frac{\mathbf{n}M^{-1}\mathbf{n}}{(\mathbf{n}M^{-1}\mathbf{p})^2}}\right)\,, \tag{2.52}$$

in order to conserve total energy and angular momentum, where M is the mass matrix, $\mathbf{n} = \mathbf{g}/|\mathbf{g}|$, and $\mathbf{g}$ is the gradient of the energy gap $\mathbf{g} = \vec{\nabla}_{\mathbf{Q}}(E_J - E_I)$ [30].

Instead of FSSH, the Landau-Zener scheme [31, 32, 33] is an alternative way to implement surface hopping method. In the Landau-Zener scheme, the electronic population dynamics is fully determined by local topologies of the potential energy surfaces. The quantum-classical Landau-Zener formula for transition probability between adiabatic electronic states I and J is

$$P_{I,J}^{\mathrm{LZ}} = \exp\left(-2\pi\frac{{\Delta E_{IJ}^{\mathrm{a}}}^2}{\hbar|\dot{\mathbf{Q}}\cdot\vec{\nabla}\Delta E_{IJ}^{\mathrm{d}}|}\right)\,, \tag{2.53}$$

where $\vec{\nabla}\Delta E_{IJ}^{\mathrm{d}}$ is the gradient of the energy difference between two diabatic electronic states I and J, and $\Delta E_{IJ}^{\mathrm{a}}$ is the energy difference between two adiabatic electronic states I and J. It is natural to expect that the transition probability should be maximized for a small energy gap and a large slope of the PESs as they come close. The implementation we used here for the Landau-Zener approach closely follows that of Jones *et al.* [31]. In the practical implementation of the Landau-Zener scheme, the trajectory is monitored until a minimum in the gap is found, and one then uses the Landau-Zener formula (Eq. 2.53) to treat the hopping between electronic states.

Both the Landau-Zener and the fewest-switches schemes guarantee that the nuclei feel the force on a single electronic PES when the system leaves the interaction regions of strong non-adiabatic coupling. This scenario is physically consistent with the fact that

in experiment the outgoing molecular fragments should be generally observed to sit on a single electronic state at the asymptotic region, rather than to maintain superposition of electronic states.

For the purpose of studying the influence of dimensionality to the surface-hopping quantum-classical dynamics, we applied the `RATTLE` scheme [34] to impose internal constraints on motions of atomic nuclei. In this way, we can precisely study the same reduced dimensionality model by both surface hopping and quantum dynamics of reduced dimensional models.

Working with Cartesian coordinates, the rigid constraints are maintained by introducing implicit forces based on Lagrange multipliers. The equation of motion for the atom i thus reads

$$m_i \ddot{\mathbf{Q}}_i = \mathbf{F}_i + \mathbf{G}_i \,, \tag{2.54}$$

where $\mathbf{F}_i$ is the inherent force from electronic potential energy surface, and $\mathbf{G}_i$ is the force acting on the atom i in order to satisfy the constraints. $\mathbf{G}_i$ is given by

$$\mathbf{G}_i = -\sum_{\alpha} \lambda_{i\alpha} \vec{\nabla}_i \sigma_{i\alpha}(\{\mathbf{Q}(t)\}) \,, \tag{2.55}$$

where $\sigma_{i\alpha}\{\mathbf{Q}(t)\} = 0$ are the set of general holonomic constraints imposed on atom i, which could be functions of either Cartesian or internal coordinates while their Cartesian derivatives $\vec{\nabla}_i \sigma_{i\alpha}(\{\mathbf{Q}(t)\})$ are evaluated by a stable numerical differentiation, and $\lambda_{i\alpha}$ are time-dependent Lagrange multipliers associated with the force of constraints, which are determined by the iterative procedure of Andersen [34]. Since the constraint forces are by construction always orthogonal to the velocity vectors of atomic nuclei, they do not impose any work to the molecular system, and the total energy conservation is guaranteed.

2.3.3 QDTK package

`QDTK` (quantum-classical dynamics toolkit) is a program package developed in our group. It is a modularized program based on Python and Fortran programming languages. The `QDTK` package consists of two major modules, i.e. the full quantum dynamics module, which is designed to treat the wave packet dynamics using MCTDH method, and the mixed quantum-classical dynamics module, which involves implementation of methods introduced in this section. I have contributed to the `QDTK` package to implement the fewest-switches surface-hopping scheme [29] and Ehrenfest dynamics scheme with electronic dephasing [28].

The mixed quantum classical dynamics module has the following basic functions,

- Initial condition sampling for nuclear position and momentum.

- Surface hopping dynamics.
- Ehrenfest dynamics with electronic dephasing.
- Evaluation of physical observables from trajectories, so far we have implemented a module to compute transient absorption spectra, and to determine reaction channels.

The initial conditions for the molecules were sampled from a Boltzman distribution in the phase space on the certain electronic PES. We have also considered sampling from a Wigner distribution of the ground vibrational state [35]. For practical implementation, we have adopted the orthant sampling scheme [36].

The implementation of surface hopping and Ehrenfest dynamics is based on a modularized programming model, in which the modules are to the maximum extent decoupled from each other. For example, the integration of newtonian equation stands as an independent module, while the force on the nuclei is determined from the surface hopping or Ehrenfest dynamics module, when either of the modules is embedded in a main program constructed by the user.

As the dynamics develops, the program records for each trajectory the positions and momenta of nuclei, as well as the electronic state at certain time step and the electronic wave function, from which physical observables can be constructed.

In the mixed quantum-classical treatment, the electronic structures are solved *on-the-fly* with external call to the `MOLCAS` *ab initio* quantum chemistry package [37], from which one could acquire necessary quantities for propagating nuclear trajectories, e.g. the force acting on the nuclei, the overlap matrix used to compute non-adiabatic coupling matrix element (Eq. 2.47). From the `MOLCAS` program we also acquire the electronic wave function, which we use for constructing physical observables subject to concrete applications.

2.4 Electronic structure

As we see from the previous sections, either quantum mechanical or mixed quantum–classical scheme needs high quality description of electronic structure, since the electronic wave function is the crucial ingredient to provide electronic potential and the force on the nuclei.

The electronic strucutre theory of molecules emerged almost immediately after the advent of quantum mechanics, following the pioneering work of F. London and W. Heitler

to explain the nature of chemical bonding of H_2 molecule in 1927, and has been a vibrant field ever since.

In a general perspective, the *ab initio* electronic structure methods can be categorised into two families, one is wave function based techniques, which includes the Hartree-Fock and various post Hartree-Fock methods, and another is electron density based techniques, a representative method in this family is density functional theory. In this thesis, for the study of photoionized molecules, we rely on the wave function based techniques, specifically on the Hartree-Fock-Koopmans and complete active space self consistent field (CASSCF) methods, because we are mainly dealing with electronic structure of ionic states of molecules. For this purpose, we need *ab initio* electronic structure methods that are suitable to treat excited state of electronic configurations containing electron hole.

The self-consistent solution of the Hartree-Fock (HF) equations for an N-electron closed shell system

$$\hat{f}|\phi_j\rangle = \epsilon_j|\phi_j\rangle \tag{2.56}$$

provides the set of occupied molecular orbitals $|\phi_j\rangle$ of the anti-symmetrized wavefunction $|\Psi_0\rangle$ corresponding to the HF ground electronic state as well as their orbital energies ϵ_j. $\hat{f}$ is the Fock operator consisting of the one-body terms of the electronic Hamiltonian and the mean-field potential, which depends on all occupied orbitals. The HF energy for the ground state of the N-electron system is

$$E_{\mathrm{HF}} = \langle\Psi_0|\hat{H}_e|\Psi_0\rangle \tag{2.57}$$

where $\hat{H}_e$ is defined in Eq. 2.2. Within this context, Koopmans' theorem shows that

$$\begin{aligned} -\epsilon_j &= \langle\Psi_j|\hat{H}_e|\Psi_j\rangle - E_{\mathrm{HF}} && (2.58)\\ &= E_j - E_{\mathrm{HF}} && (2.59) \end{aligned}$$

where $|\Psi_j\rangle = \hat{c}_j|\Psi_0\rangle$ is an $(N-1)$-electron state constructed from the HF solution by removing an electron from the j-th orbital, $\hat{c}_j$ is the annihilation operator for the j-th orbital and E_j is an approximate eigenenergy through first order in many-body perturbation theory. If one accepts $|\Psi_j\rangle$ as an approximation to the j-th electronic eigenstate of the $(N-1)$-electron system, then the negative energies of the occupied orbitals obtain the meaning of ionization potentials, which constitutes Koopmans' approximation. Within this approximation, the energy of the j-th ionic state is simply $E_j = E_{\mathrm{HF}} - \epsilon_j$, which requires for its evaluation only one ground state HF calculation, with the self-consistent orbitals obtained from Eq. 2.56, $\langle\Psi_i|\hat{H}_e|\Psi_j\rangle = E_j\delta_{ij}$. Therefore, in a configuration interaction sense and within the one-hole space, the $|\Psi_j\rangle$ configuration represents the best possible approximation to the j-th $(N-1)$-electron state. Of course, this is still an approximation

to the true eigenstate. For example, orbital relaxation effects caused by the increased total charge and the contribution of two-hole one-particle configurations, which becomes crucial to describe inner-valence holes, are neglected. Nonetheless, the adoption of Koopmans' approximation provides a qualitative approach and a feasible alternative to describe the electronic structure and nuclear dynamics evolving within the large manifold of tens or even hundreds of $(N-1)$-electron outer-valence states accessible upon photoionization of medium sized molecules and clusters.

In order to satisfy the demand to perform on-the-fly dynamics (forces are computed as trajectories evolve) in the mixed quantum–classical scheme, one needs an efficient evaluation of the gradient of the electronic energy with respect to nuclear displacements. For non-adiabatic dynamics the coupling terms between electronic states are needed as well. HF energy gradients are implemented in the majority of quantum chemistry packages and are calculated from the derivatives of one- and two-body integrals and the molecular orbital coefficients [38]. All that is needed to calculate $\frac{\partial E_j}{\partial \lambda}$, where λ represents an atomic displacement, is the derivative of the corresponding orbital energy $\frac{\partial \epsilon_j}{\partial \lambda}$, which is calculated from the same integral derivatives as the total $\frac{\partial E_{\mathrm{HF}}}{\partial \lambda}$. In our calculations, we use the multiconfigurational capabilities of the `MOLCAS` [37] package to generate the electronic wavefunctions $|\Psi_j\rangle$ with the orbitals from a previous HF calculation and then obtain the energy gradient for this single configuration.

The disadvantage of Hartree-Fock theory is the missing of electron correlation effect. In the Hartree-Fock theory, the electronic wave function is approximated by a single Slater determinant. Exact wave functions, however, cannot generally be expressed as single determinant. Since the single-determinant approximation does not take into account Coulomb correlation, it leads to a total electronic energy that is always above the energy from the exact solution. The energy difference $\Delta E = E_{\mathrm{HF}} - E_{\mathrm{exact}}$ is called the correlation energy E_{corr}.

A general solution to capture the electronic correlation effect is the family of post Hartree-Fock methods, the complete active space self-consistent field (CASSCF) method used in this thesis is a member of post Hartree-Fock methods family, which can be viewed as a variation of multi-configurational self-consistent field (MCSCF) method.

To describe the electron correlation effect beyond the Hartree-Fock-Koopmans level for an $(N-1)$-electron system, one could firstly follow the configuration interaction (CI) scheme. In the CI scheme, one introduces the Slater determinents of various electronic configurations, dubbed configuration state functions (CSFs), of higher order excitations into the wave function *ansatz*, i.e. the wave function for a certain eigenstate of the $(N-1)$-

electron system can be constructed from the N-electron wave function Ψ_0 as

$$\begin{aligned} \left|\Psi^{(N-1)}\right\rangle &= \left(\underbrace{\sum_i \hat{E}_i}_{\text{1h}} + \underbrace{\sum_{a,j<k} \hat{E}^a_{jk}}_{\text{2h1p}} + \cdots \right) |\Psi_0\rangle \\ &= \sum_I C_I \, |\Psi_I\rangle \ , \end{aligned} \tag{2.60}$$

where

$$\begin{aligned} \hat{E}_i \, |\Psi_0\rangle &= C_i \hat{c}_i \, |\Psi_0\rangle \\ \hat{E}^a_{jk} \, |\Psi_0\rangle &= C^a_{ij} \hat{c}^\dagger_a \hat{c}_j \hat{c}_k \, |\Psi_0\rangle \ . \end{aligned} \tag{2.61}$$

Indices $i, j, k, \cdots$ denote occupied orbitals, whereas indices a indicate virtual (unoccupied) orbitals.

In a general MCSCF framework, one obtains the corresponding electronic energies by variational optimisation of both CI expansion coefficients C_I and molecular orbitals $|\phi_j\rangle$ in the CSFs with a self-consistent procedure. The MCSCF procedure subject to wave function *ansatz* in Eq. 2.60 is known as the restricted active space self-consistent field (RASSCF) method, since one restricts the number of electrons and electron holes in certain orbital subspaces, called the active space.

As expressed in Eq. 2.60, in the RASSCF scheme, the quality of electronic structure for molecular ionic states can be systematically improved. Starting from the Hartree-Fock-Koopmans wave function, which involves the one hole (1h) configuration, one may improve the quality of truncated CI expansion by adding accordingly the two-hole-one-particle (2h1p) and three-hole-one-particle (3h2p) configurations to it, in order to more accurately describe the dynamical correlation effect. A 2h1p configuration, for example, means that one electron has been removed accompanied by an excitation of another electron into an unoccupied orbital.

Without restricting the types of electronic excitations in the active space, one could extend the RASSCF method to the complete active space SCF (CASSCF) method [39], where the linear combination of all possible CSFs that arise from a particular number of electrons in a particular number of orbitals (active space). For example, one might define CASSCF(n,m) for a molecule, where n valence electrons are distributed between all configurations that can be constructed from m occupied and virtual molecular orbitals.

Besides, the algebraic diagrammatic construction (ADC) [40], which combines configuration interaction with perturbation theory, could be adopted for our purpose to treat the electronic structure of ionic states.

Same as the Hartree-Fock-Koopmans calcualtion, all CASSCF calculations involved in this thesis were performed with the quantum chemistry package `MOLCAS` [37].

2.5 Bibliography

[1] D. Tannor, *Introduction to Quantum Mechanics: A Time-Dependent Perspective* (Macmillan, 2007).

[2] M. Born and J. R. Oppenheimer, Ann. Phys. **389**, 457 (1927).

[3] M. Born and K. Huang, *Dynamical Theory of Crystal Lattices* (Oxford University Press, 1954).

[4] F. Riewe, Phys. Rev. E **53**, 1890 (1996).

[5] G. A. Worth and L. S. Cederbaum, Annu. Rev. Phys. Chem. **55**, 127 (2004).

[6] Z. H. Top and M. Baer, J. Chem. Phys. **66**, 1363 (1977).

[7] M. Baer, Chem. Phys. Lett. **35**, 112 (1975).

[8] A. Abedi, N. T. Maitra, and E. K. U. Gross, Phys. Rev. Lett. **105**, 123002 (2010).

[9] A. Abedi, F. Agostini, Y. Suzuki, and E. K. U. Gross, Phys. Rev. Lett. **110**, 263001 (2013).

[10] S. K. Min, A. Abedi, K. S. Kim, and E. K. U. Gross, arXiv:1402.0227 .

[11] M. H. Beck, A. Jäckle, G. A. Worth, and H.-D. Meyer, Phys. Rep. **324**, 1 (2000).

[12] H.-D. Meyer, F. Gatti, and G. Worth, eds., *Multidimensional Quantum Dynamics: MCTDH theory and its applications* (Wiley-VCH, 2009).

[13] G. A. Worth, M. H. Beck, A. Jäckle, and H.-D. Meyer, The MCTDH Package, Version 8.2, (2000). H.-D. Meyer, Version 8.3 (2002), Version 8.4 (2007), Version 8.5 (2014). See http://mctdh.uni-hd.de.

[14] U. Manthe, J. Chem. Phys. **128**, 164116 (2008).

[15] O. Vendrell and H.-D. Meyer, J. Chem. Phys. **134**, 044135 (2011).

[16] J. Caillat, J. Zanghellini, M. Kitzler, O. Koch, W. Kreuzer, and A. Scrinzi, Phys. Rev. A **71**, 012712 (2005).

[17] H. Wang and M. Thoss, J. Chem. Phys. **131**, 024114 (2009).

[18] A. Jäckle and H.-D. Meyer, J. Chem. Phys. **104**, 7974 (1996).

[19] A. Jäckle and H.-D. Meyer, J. Chem. Phys. **109**, 3772 (1998).

[20] P. Ehrenfest, Zeitschrift für Physik **45**, 455 (1927).

[21] C. G. Torre, *Lecture Notes in Quantum Mechanics* (Utah State University, 2008).

[22] J.-Y. Zeng, *Introduction to Quantum Mechanics* (Science Press, 2000).

[23] E. Schrödinger, Naturwissenschaft **14**, 664 (1926).

[24] S. Hammes-Schiffer and J. C. Tully, J. Chem. Phys. **101**, 4657 (1994).

[25] E. Fabiano, T. W. Keal, and W. Thiel, Chem. Phys. **349**, 334 (2008).

[26] J. Pittner, H. Lischka, and M. Barbatti, Chem. Phys. **356**, 147 (2009).

[27] A. Castro and E. K. U. Gross, J. Phys. A: Math. Theor. **47**, 025204 (2014).

[28] M. D. Hack and D. G. Truhlar, J. Chem. Phys. **114**, 9305 (2001).

[29] J. C. Tully, J. Chem. Phys. **93**, 1061 (1990).

[30] M. S. Topaler, T. C. Allison, D. W. Schwenke, and D. G. Truhlar, J. Phys. Chem. A **102**, 1666 (1998).

[31] G. A. Jones, B. K. Carpenter, and M. N. Paddon-Row, J. Am. Chem. Soc. **120**, 5499 (1998).

[32] A. I. Voronin, J. M. C. Marques, and A. J. C. Varandas, J. Phys. Chem. A **102**, 6057 (1998).

[33] E. Tapavicza, U. Tavernelli, C. Rothlisberger, C. Fillipi, and M. E. Casida, J. Chem. Phys. **129**, 124108 (2008).

[34] H. C. Andersen, J. Comput. Phys. **52**, 24 (1983).

[35] G. H. Peslherbe, H. Wang, and W. L. Hase, Adv. Chem. Phys. **105**, 171 (1999).

[36] L. Sun and W. L. Hase, J. Chem. Phys. **133**, 044313 (2010).

[37] V. Veryazov, P.-O. Widmark, L. Serrano-Andres, R. Lindh, and B. Roos, Int. J. Quantum Chem. **100**, 626 (2004).

[38] P. Pulay, G. Fogarasi, F. Pang, and J. E. Boggs, J. Am. Chem. Soc. **101**, 2550 (1979).

[39] B. O. Roos, P. R. Taylor, and P. E. M. Siegbahn, Chem. Phys. **48**, 157 (1980).

[40] J. Schirmer, Phys. Rev. A **26**, 2395 (1982).

Chapter 3

Non-Born-Oppenheimer Electronic-Nuclear Dynamics of Gas Phase Molecules Ionized by XUV Laser

The advent of bright light sources to produce ultrashort laser pulses in the extreme ultraviolet (XUV) and x-ray regime enables us to study the photoionization and its follow-up processes involving valence and core shell electrons of molecules.

The photoionized molecules carry an electron hole in them, the interaction of the electron hole with nuclei and the remaining electrons can have profound impact on various physical, chemical, and biological processes. A prominent example is the self protection mechanism of DNA against the photo-damage of sunshine [1].

In chapter 3, I present the study concerning the motion of electron holes created in the molecule by photoionization. Section 3.1 describes the electron hole dynamics in molecular ions that are produced by XUV free electron laser. In Section 3.2, I show a possible route to explicitly track the electron hole motion using transient x-ray absorption spectroscopy.

3.1 Correlated proton-hole dynamics in $H^+(H_2O)_n^+$

The profound effect of non-adiabatic interactions between electronic states on the time-evolution of molecular systems has been in the central focus of excited state chemical

dynamics [2, 3, 4, 5, 6, 7, 8, 9, 10, 11, 12, 13, 14, 15, 16, 17]. The non-radiative decay of excited electronic states when a molecule approaches conical intersections or avoided crossings can result in a significant amount of energy redistribution into the vibrational modes, or even in isomerization or fragmentation processes. Electronically excited molecules and clusters can be produced in various ways. One possibility is by strong-field ionization, in which several photons have to be absorbed before an electron leaves the system. This results in systems that are close to the ground electronic state of the ion. Another possibility is by one-photon absorption of extreme ultra-violet (XUV) or x-ray photons. This leaves the system potentially in a highly excited electronic state, which can even autoionize if the electronic energy is above the next ionization threshold of the system at hand. There is a large body of knowledge related to the dynamics and spectroscopic characterization of excited molecular systems after photoabsorption and photoionization [18, 19]. However, not so much is known about the nuclear dynamics and the role of non-adiabatic effects unfolding after XUV one-photon ionization of weakly bound clusters, for example of water molecules [20, 21, 22]. In the case of weakly bound clusters, the charge produced by the ionization process may lead to a fast fragmentation of the system and to fast charge redistributions related to both electronic and nuclear degrees of freedom. Since clusters under such conditions may often fragment, non-Born-Oppenheimer (non-BO) effects lead to irreversible electronic relaxation processes in which the electronic excitation energy ends up as kinetic energy of the fragments.

For a theoretical treatment of such non-adiabatic dynamics, two essential ingredients are required. First, a set of reliable potential energy surfaces (PES) of the valence excited electronic states of the ionic system and their couplings, and second, an efficient approach to calculate the motion of atomic nuclei on that PES. Quantum mechanical wavepacket methods have established a rigorous basis for fully understanding the mechanisms of molecular processes [23, 24]. However, in order to treat medium- or large-size molecular systems fully quantum mechanically, one has to often make compromises to reduce the dimensionality due to limitations in computational power, or to introduce model Hamiltonians. Even though it is possible to break the exponential scaling of wavepacket methods with e.g. the ML-MCTDH approach, these methods are still difficult to apply to non-model Hamiltonians [25]. If one is ready to compromise in the description of nuclear quantum effects, trajectory based approaches working in a Cartesian space, either based on Gaussian wavepackets [24], semiclassical [26] or mixed quantum-classical [27] approaches provide efficient computational strategies to treat medium to large molecular systems in full dimensionality. However, one must realize that their reliability may break down for processes out of their scope of applicability [28].

In our study, the Coulomb explosion of the protonated water dimer $H^+(H_2O)_2$ after

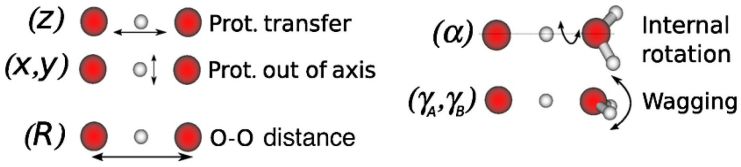

Figure 3.1: Schematic representation of the seven internal nuclear coordinates used in the wave packet propagation showing in each case the relevant atoms. This figure is taken from Ref. [30]. Copyright © 2013 American Physical Society (APS).

ionization by XUV radiation has been investigated using quantum wavepacket and a mixed quantum-classical surface-hopping approach. Experiments on this fragmentation process had been performed at the free-electron laser (FEL) FLASH [29], which provides an established reference for our theoretical simulation.

3.1.1 Adiabatic potential energy surfaces of the $H_5O_2^{2+}$dication

For the quantum-dynamical calculations of $H_5O_2^{2+}$, the system is described by a mixed set of polyspherical Jacobi-valence coordinates. The definition of the polyspherical coordinates is described in detail in previous work of some of us [31]. The chosen coordinate system is known to be advantageous for treating large amplitude motions [32]. The set of polyspherical vectors is shown in Fig. 3.2. From the full set of 15 nuclear coordinates that describe the geometry of the cluster, we choose a reduced set of 7 coordinates consisting of $\{x, y, z, R, \alpha, \gamma_A, \gamma_B\}$, as illustrated in Fig. 3.1, where R is the distance between oxygen atoms of the two water monomers, the Cartesian coordinates (x, y, z) describe the position of the central proton with origin set at the center of mass of the two oxygen atoms, and α (internal relative rotation) and $\gamma_{(A,B)}$ (waggings) represent the Euler angles defining the relative orientation of the two water monomers. The internal degrees of freedom of the water monomers and their rocking motion, which possess higher moment of inertia than that of wagging motion, were chosen to be frozen at the equilibrium positions in the Franck-Condon region, namely in the vicinity of ground state geometry. We also adopt the definition of the dimensionless z coordinate [33]

$$z \mapsto \frac{z}{R - 2d_0}, \tag{3.1}$$

which in this case with large separations of the monomers is crucial in order to adequately avoid molecular configurations with the central proton unphysically close to the oxygen atoms. In Eq. 3.1, d_0 is chosen to be the covalent radius of the oxygen atom, 0.65Å.

We proceed by calculating the adiabatic PES on the 7D grid of the coordinates men-

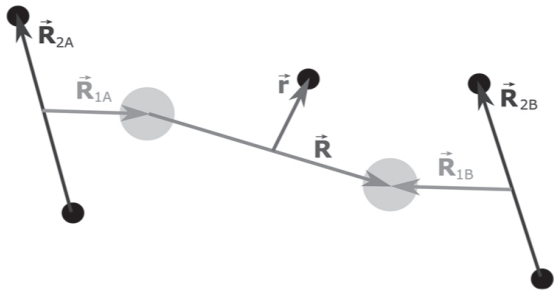

Figure 3.2: Mixed Jacobi-valence description of the $H_5O_2{}^{2+}$system. The two big circles represent the position of the oxygen atoms, while the small circles represent the positions of the hydrogen atoms. This figure is taken from Ref. [34]. Copyright © 2013 American Institute of Physics (AIP).

tioned above. As detailed in the next section, we then diabatize *point-by-point* based only on the energy values on the grid. We apply this strategy instead of e.g. using a vibronic-coupling Hamiltonian with a fixed expansion point because of the large amplitude motions taking place during the fragmentation. Due to the very large number of points in the 7D grid we construct adiabatic *ab initio* potential energy surfaces (PES) for the ionized states of $H_5O_2{}^{2+}$using a high level–low level approach

$$V_i(\mathbf{Q}) = V_{i,\text{high}}(\mathbf{a}; x, y, z, R) + (V_{i,\text{low}}(\mathbf{Q}) - V_{i,\text{low}}(\mathbf{a}; x, y, z, R)) \tag{3.2}$$

where i refers to the adiabatic electronic state. The high level electronic structure calculations are hence performed in the 4D subspace of the central proton displacements and the oxygen-oxygen distance coordinates. As will be discussed later, these degrees of freedom are the key ones to describe the fragmentation process and the involved conical intersections. In the high-level calculations the spectator degrees of freedom α, γ_a and γ_b are set at reference positions, where $\mathbf{a} = \{\alpha_0, \gamma_{a,0}, \gamma_{b,0}\}$ corresponding to the equilibrium geometry of $H^+(H_2O)_2$ within the D_{2d} point group. In order to accurately describe the excited state PES of $H_5O_2{}^{2+}$in the high level subspace, we use the complete active space self-consistent field (CASSCF) method [35, 36] employing the cc-pVTZ basis set [37]. We use an active space with 11 electrons distributed in 8 molecular orbitals. For selected cuts we investigated the effect of including dynamical correlation at the CASPT2 level, but the change in shape of the PES was found to be small. The low-level calculations were performed at the Hartree-Fock-Koopmans (HF-K) level

$$V_{i,\text{HF-K}} = V_{\text{HF}} - \epsilon_i \,, \tag{3.3}$$

where V_{HF} is the ground state Hartree-Fock energy of $H^+(H_2O)_2$ and ϵ_i is the energy of the ith orbital counting from the highest occupied molecular orbital downwards. The two-level scheme is similar in spirit to a n-mode representation of the PES [31, 38, 39], in which the largest possible cluster (7D) is present but computed at a lower level of theory than smaller clusters.

The potential energy surfaces of the three lowest–energy states of the Zundel dication are shown in Fig. 3.3(a). The two nuclear coordinates of the 2D cut in Fig. 3.3(a) correspond to the oxygen–oxygen distance (R) and to the projection of the central proton position on the oxygen–oxygen axis (z), whereas the rest of the coordinates are held fixed.

The three low lying potential energy surfaces of the Zundel dication is illustrated in Fig. 3.3(b) as a function of the central proton position. The shape of the surfaces is mostly the result of the electrostatic repulsion between the positive charge density associated with the central proton and that of the electron hole. This is made clear by noting that the gradient of potential at the central point of conical intersection is about 6.5 eV·Å^{-1}. This is equivalent of two point charges of equal sign at a distance of 1.4 Å. The distance of the central proton to one of the oxygen atoms is about 1.2 Å at the equilibrium geometry of the molecular ion. When the central proton is displaced towards, e.g. the water molecule on the left, the electronic state with the hole on the water molecule on the right side stabilizes, while the state with the hole on the left side destabilizes, resulting in the conical intersection between the electronic states as a function of the proton position. The third electronic state of the dication can be described by an electron hole delocalized mostly around the central proton. Therefore the potential is quite flat along the proton transfer coordinate in the vicinity of the Frank–Condon point. When the proton is displaced towards either water molecule, however, the electron hole eventually becomes more stable on a localized water site, and at that geometry the third dicationic state crosses with the second one, resulting also in a seam of conical intersection.

It is convenient to label the electronic states of interest using the C_{2v} point group as reference. The lowest two states are energetically degenerate when the molecule is close to the absolute minimum in the electronic ground state of the Zundel cation, where they belong to the E irreducible representation within D_{2d} group, the degeneracy is lifted in first order along the proton-transfer coordinate of B_2 symmetry, resulting in a $E \otimes b$ conical intersection. Intuitively, when the central proton is displaced towards e.g. the water molecule on the left, the electronic state with the hole on the water molecule of the right side gets stabilized, while the state with the hole on the left side is destabilized, leading to the lifting of the degeneracy. The third electronic state of the dication can be described by an electron hole extending mostly around the central hydrogen bond. Therefore, the PES is relatively flat along the proton-transfer coordinate in the vicinity of the Franck-Condon point. When the proton is displaced towards either water molecule, the electron hole eventually becomes more stable on the water molecule opposite to the proton side, and at that geometry the third dicationic state crosses with the second one, resulting in new seams of conical intersections. This topology can be seen in Fig. 3.4. The Coulomb repulsion between the proton and the electron hole, which are both positively

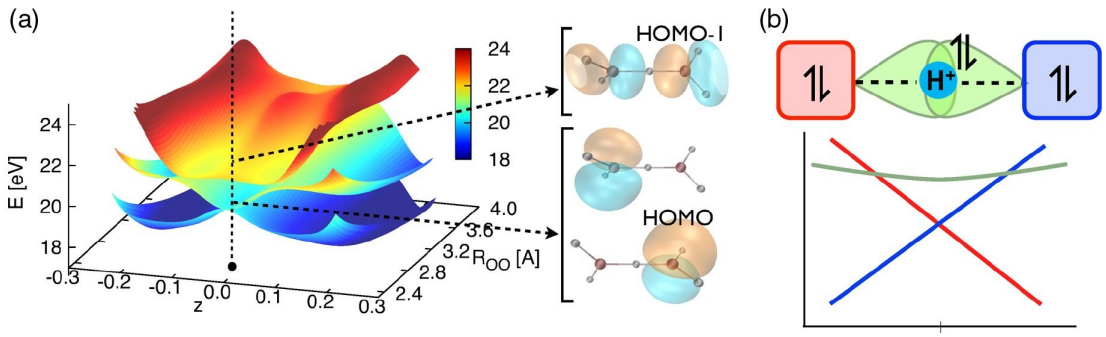

Figure 3.3: (a) Potential energy surfaces of the three lowest electronic states of $H(H_2O)_2^{++}$ for the z (central proton position projected onto the oxygen–oxygen axis) and R (oxygen–oxygen distance) coordinates and keeping the rest of the vibrational modes frozen. The dot marks the Frank–Condon nuclear geoemtry. The orbitals shown represent the highest occupied molecular orbitals at the Hartree–Fock mean field level, and the correspond to the electron hole in the leading configuration for each of the three lowest–energy electronic states of the dication in a multiconfigurational description. (b) Scheme of the hydrogen–bonded system, indicating the location of the electron pairs that can be ionized and they corresponding potential energy surfaces as the function of central proton position. Ionization leading to the electronic states under consideration can take place from lone electron pairs on each monomer (in red and blue, negative and positive slope curves, respectively) or from the electrons involved in the hydrogen bonding (in green, horizontal curve). This figure is taken from Ref. [30]. Copyright © 2013 American Physical Society (APS).

charged, further drives the molecular fragments carrying one of them to separate from each other. In this way, the electronic motion reacts on the nuclei, while the nuclear motion drives non-adiabatic electronic transitions. It is worth mentioning that the PES topology described above will be general to ionized clusters of $M\cdots H^+\cdots M$ type featuring strong and symmetrical hydrogen bonds, where M stands for molecules that are able to support hydrogen bonds.

3.1.2 Diabatization of the Hamiltonian

To describe the fragmentation dynamics of $H_5O_2{}^{2+}$on the three lowest outer-valence electronic states by quantum dynamics, we construct the Hamiltonian in a diabatic representation from the adiabatic PES discussed above.

Recall the discussion in chapter 2, we have the complete Schrödinger equation from Eq. 2.6 in the adiabatic representation. namely the representation subject to basis in the

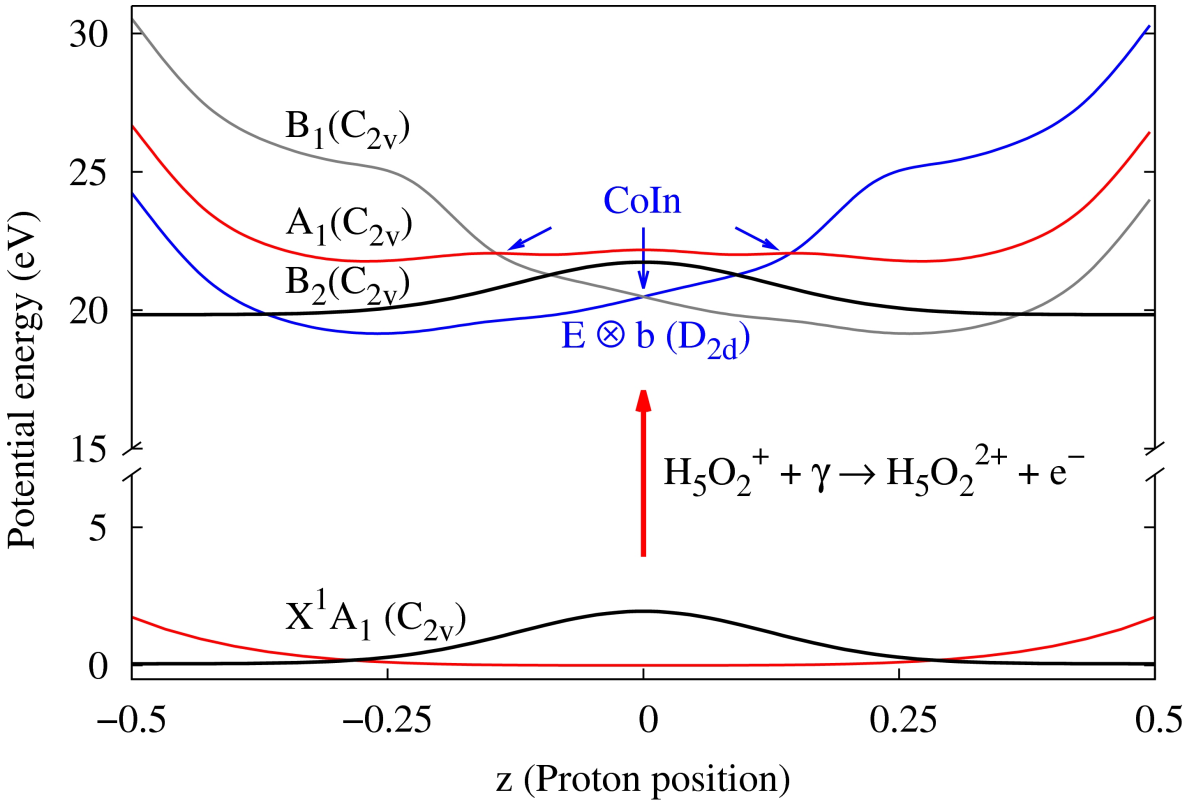

Figure 3.4: A schematic view of the initial photoionization process of the $H^+(H_2O)_2$ cation. The potential energy curves, labeled by B_1, B_2 and A_1 respectively, for the excited electronic states of the ionized $H_5O_2{}^{2+}$dication and the ground electronic state of the $H^+(H_2O)_2$ cation (X^1A_1) are depicted as a function of proton position z. The origin of the potential energy was set to the energy of $H^+(H_2O)_2$ cation at its equilibrium geometry on the ground state PES. This figure is taken from Ref. [34]. Copyright © 2013 American Institute of Physics (AIP).

Born–Oppenheimer factorization (Eq. 2.3 and 2.4),

$$[T_{\mathrm{N}}(\mathbf{Q}) + V_m(\mathbf{Q})]\,\chi_m(\mathbf{Q}) + \sum_n \Lambda_{mn}(\mathbf{Q})\chi_n(\mathbf{Q}) = E\chi_m(\mathbf{Q})\,,$$

in which the non–Born–Oppenheimer effect is introduced by the derivative coupling Λ_{mn}, which is expressed as

$$\begin{aligned}\Lambda_{mn}(\mathbf{Q}) &= -\left\langle \varphi_m \left| \vec{\nabla}_Q \right| \varphi_n \right\rangle \cdot \vec{\nabla}_Q + \frac{1}{2}\left\langle \varphi_m \left| \nabla_Q^2 \right| \varphi_n \right\rangle \\ &= -\vec{\Lambda}^{(1)}_{mn} \cdot \vec{\nabla}_Q + \frac{1}{2}\Lambda^{(2)}_{mn}\,, \end{aligned} \tag{3.4}$$

it is clear that Λ_{mn} couples different states $|\varphi_m\rangle$ and $|\varphi_n\rangle$, via the gradient of nuclear coordinates.

However, an apparent disadvantage to use adiabatic representation in a quantum treatment of non–Born–Oppenheimer dynamics is that the kinetic energy coupling can be singular when the electronic states are degenerate for certain molecular geometries, e.g. at the conical intersection, because the derivative coupling vector

$$\vec{\Lambda}^{(1)}_{mn} = \left\langle \varphi_m \left| \vec{\nabla}_Q \right| \varphi_n \right\rangle = \frac{\left\langle \varphi_m \left| \vec{\nabla}_Q H_\mathrm{e} \right| \varphi_n \right\rangle}{V_n - V_m}, \text{ for } m \neq n \tag{3.5}$$

diverges if $V_n = V_m$, i.e. the n-th and m-th electronic states are degenerate.

Thus it is usually favorable to choose the diabatic representation to treat the non–Born–Oppenheimer dynamics. In the diabatic representation we eliminate the diverging part of the derivative couplings of the kinetic energy term that would appear in the adiabatic Hamiltonian operator [2], using a linear rotation in the basis function space [40]. The kinetic energy matrix elements are made singularity–free at the conical intersections.

In the diabatic representation, the total Hamiltonian can be written as (Eq. 2.18)

$$\mathbf{H} = T_\mathrm{N}\mathbf{1} + \mathbf{W}, \tag{3.6}$$

where T_N is the nuclear kinetic energy operator (KEO) and $\mathbf{W}(\mathbf{Q}) = U^\dagger(\mathbf{Q})V(\mathbf{Q})U(\mathbf{Q})$ is the potential energy matrix in diabatic representation. Practically in this thesis, the diabatic potential energy matrix $\mathbf{W}$ is constructed relying on a regularized diabatization scheme [2, 41, 42, 43, 44] , which is discussed in the following.

We first adopt symmetry-adapted coordinates classified with respect to the D_{2d} point group, in order to take advantage of the fact that the coordinates responsible for the linear non-adiabatic coupling should satisfy the condition

$$\Gamma_s \otimes \Gamma_{s'} \otimes \Gamma_\alpha \supset A_g \tag{3.7}$$

where Γ_s, $\Gamma_{s'}$, Γ_α are the irreducible representations of the electronic states and nuclear coordinates, respectively [41]. The working equation for the diabatization procedure for two states reads [41]

$$\mathbf{W}^{\alpha\beta} = \Sigma^{\alpha\beta}\mathbf{1} + \frac{\Delta^{\alpha\beta}(\mathbf{Q}_g, \mathbf{Q}_u)}{\sqrt{\frac{(\Delta_0^{\alpha\beta})^2}{4} + (\lambda^{\alpha\beta}\cdot\mathbf{Q}_u)^2}} \begin{pmatrix} -\frac{\Delta_0^{\alpha\beta}}{2} & \lambda^{\alpha\beta}\cdot\mathbf{Q}_u \\ \lambda^{\alpha\beta}\cdot\mathbf{Q}_u & -\frac{\Delta_0^{\alpha\beta}}{2} \end{pmatrix} \tag{3.8}$$

where α, β are electronic state indices, $\Delta_0^{\alpha\beta} = \Delta V_0^{\alpha\beta}$ is the energy difference between adiabatic PES V^α and V^β in the reference coordinate subspace, and the coupling constants $\lambda_i^{\alpha\beta}$ were determined according to [6]

$$\lambda_i^{\alpha\beta} = \left\{ \frac{1}{8}\frac{\partial^2}{\partial Q_u^2}(V^\beta(Q_g, Q_u) - V^\alpha(Q_g, Q_u))^2 \right\}^{\frac{1}{2}} \Bigg|_{Q_g; Q_u = 0} \tag{3.9}$$

To construct the linear coupling matrix in Eq. 3.8, the coordinates were grouped by their associated representations. $G_1 \equiv (\frac{1}{\sqrt{2}}(x \pm y), R, \frac{1}{\sqrt{2}}(\gamma_A \pm \gamma_B))$ and $G_3 \equiv (R, z, \alpha)$ are the sets of modes that directly enters the diagonal potential matrix elements, $G_2 \equiv (z, \alpha)$ and $G_4 \equiv (\frac{1}{\sqrt{2}}(x \pm y), R, \frac{1}{\sqrt{2}}(\gamma_A \pm \gamma_B))$ are the modes responsible for the off-diagonal linear couplings between different electronic states. The coordinates in groups G_1 and G_2 are for pair of states (1,2), the coordinates in groups G_3 and G_4 are for pairs of states (1,3) and (2,3).

We then apply the regularized-states procedure of Eq. 3.8 to the three adiabatic states in pairs first. The submatrix that couples diabatic states 1 and 2 is kept. From the submatrices for states $(1,3)$ and $(2,3)$, we keep only the corresponding W_{13}, W_{23}, and the two W_{33} elements are averaged. Now, the elements W_{13} and W_{23} from the latest diagonalization correspond to states 1 and 2 that have not been mixed among each other. We resolve this by applying the transformation

$$\begin{pmatrix} \tilde{W}_{13} \\ \tilde{W}_{23} \end{pmatrix} = U \begin{pmatrix} W_{13} \\ W_{23} \end{pmatrix} \tag{3.10}$$

such that the new coupling elements now connect the diabatic state 3 to the diabatic states 1 and 2 obtained from the first diabatization procedure. In Eq. 3.10, the 2×2 matrix $\mathbf{U}$ is the transformation matrix that diagonalizes the sub-potential-matrix $\mathbf{W}^{(12)}$ for the lowest two diabatic states, i.e. $\mathbf{U}^\dagger \mathbf{W}^{(12)} \mathbf{U} = V^{(12)}$.

The potential energy matrix $\mathbf{W}$ in diabatic representation is finally regularized through

$$\mathbf{W}^{\text{reg}} = \mathbf{S}\mathbf{V}^{(ab\ intio)}\mathbf{S}^\dagger \tag{3.11}$$

where $\mathbf{S}$ is the transformation matrix that diagonalizes $\mathbf{W}$, i.e. $\mathbf{S}^\dagger \mathbf{W} \mathbf{S} = \mathbf{V}$. The main purpose of this last regularization procedure is to ensure that the *ab initio* potential energy data $\mathbf{V}^{(ab\ intio)}$ in the adiabatic representation is fully reproduced via the inverse transformation from the diabatic representation used in the calculations [41]. This transformation does not change the diabatic matrix in 1^{st} order near the conical intersections.

After construction of the regularized diabatic potential energy matrix $\mathbf{W}_{\text{reg}}$, the final Hamiltonian in the diabatic representation is obtained by adding the nuclear kinetic energy operator (KEO) into Eq. 2.18. For the sake of simplicity, we do not distinguish $\mathbf{W}$ from $\mathbf{W}^{\text{reg}}$ in the following.

3.1.3 Quantum wave packet dynamics

The MCTDH method [23, 45, 46] introduced in chapter 2 is then employed to simulate the nuclear dynamics of the molecules ions based on the electronic potentials in diabatic

representation.

In our case, the dynamics involves several electronic states, the multi-electronic state wave functions can be written as

$$\Psi(Q_1, \ldots, Q_p, t) = \sum_{\alpha=1}^{n_s} \Psi_\alpha(Q_1, \ldots, Q_p, t) \, |\alpha\rangle \,, \tag{3.12}$$

where n_s is the number of electronic states. We have applied the multi-state formulation of MCTDH, in which a separate set of SPFs is propagated for every electronic state [47].

The ground state vibrational wavefunction of the $H^+(H_2O)_2$ cation was obtained on the ground state PES employing the *improved relaxation* method [48]. This method converges faster than a simple imaginary time propagation and is essentially a multi-configuration self-consistent field approach that takes advantage of the MCTDH machinery [31, 49].

The acquired ground state wave function was then directly transferred to the excited states of the ionized $H_5O_2{}^{2+}$dication as the initial wavepacket, assuming sudden ionization of the $H^+(H_2O)_2$ cation by the FEL pulse and validity of the Franck-Condon principle [50], as schematically depicted in Fig. 3.4. The wavepacket dynamics on the excited state potentials were propagated up to 100 fs. Within a time period of $\sim$ 65 fs the major photofragmentation process of the Zundel cation was observed in the present calculation, yet we carried out 100 fs quantum dynamical propagation to enable full absorption of the wave packet by the complex absorbing potentials (CAPs) for the purpose of flux analysis.

In order to enhance the efficiency of the MCTDH calculation, we made use of mode-combination using the following four combined modes $Q_1 = [x, y]$, $Q_2 = [z, \alpha]$, $Q_3 = [R]$ and $Q_4 = [\gamma_A, \gamma_B]$. The definition of the underlying one-dimensional (1D) grids and the discrete variable representation (DVR) is provided in Table 3.1. Table 3.2 contains the numbers of SPFs used for each degree of freedom in the MCTDH relaxation and dynamics calculations, which gives converged dynamical results.

In the present calculation, the complex absorbing potentials (CAPs) were applied to x, y, R, γ_A and γ_B coordinates in order to absorb the outgoing wavepacket. The CAP V_c for coordinate q_i takes the form[51]

$$V_c(q_i) = -i\eta \, |q_i - q_{i,c}|^n \, \theta(|q_i - q_{i,c}|) \tag{3.13}$$

where the strength parameter η, the order n and the threshold $q_{i,c}$ were chosen so as to minimize the reflection from the CAP along the coordinate q_i. The suitably chosen CAP parameters are listed in Table 3.2.

From the time-dependent wavepacket propagations, various properties were extracted. Since the wavepacket propagations were perfomed in a diabatic representation, the diabatic

Table 3.1: Definition of the one-dimensional grids. N denotes the number of grid points and x_i, x_f the location of the first and the last point. The DVRs are defined in Appendix B of Ref. [23] (Radial degrees of freedom are given in atomic units, while angular degrees of freedom are given in radians.)

Coordinates	N	x_i	x_f	DVR
x	21	-3.0	3.0	sin
y	21	-3.0	3.0	sin
R	360	3.9	15.5	sin
z	63	-0.5	0.5	sin
α	26	0	2π	exp
γ_A	21	-1.8	1.8	sin
γ_B	21	π-1.8	π+1.8	sin

Table 3.2: Details of the MCTDH calculation. For each combined mode Q_i, the number of single particle functions (SPFs) and the parameters for the complex absorbing potentials (CAPs) of the form $V_c(q_i) = -i\eta\,|q_i - q_{i,c}|^n\,\theta(|q_i - q_{i,c}|)$ are given. The CAP parameters were listed as $(q_{i,c}, \eta, n)_{q_i}$. Atomic units are used for radial degrees of freedom, while radians are used for angular degrees of freedom.

Combined modes	Numbers of SPFs	CAP parameters
$Q_1 = [x, y]$	10	$(\pm 2.50, 0.05, 3)_{x,y}$
$Q_2 = [z, \alpha]$	10	z, α are CAP free
$Q_3 = [R]$	5	$(12.30, 0.005, 3)_R$
$Q_4 = [\gamma_A, \gamma_B]$	5	$(\pm 1.65, 0.05, 3)_{\gamma_A}$, $(\pi \pm 1.65, 0.05, 3)_{\gamma_B}$

electronic state populations $P_\alpha(t)$ and the reduced densities $\rho_\alpha(q_i, q_j, t)$ of the wavepacket for the electronic state $|\alpha\rangle$ can be readily obtained as

$$P_\alpha(t) = \langle \Psi_\alpha(t) \mid \Psi_\alpha(t) \rangle \tag{3.14}$$

and

$$\rho_\alpha(q_i, q_j, t) = \int \Psi_\alpha^*(t)\Psi_\alpha(t) \prod_{l \neq i,j} dq_l, \tag{3.15}$$

respectively. In order to facilitate the comparison with surface-hopping calculations, where the electronic populations are expressed in terms of adiabatic electronic states, we also calculate the *adiabatic populations* [52]. Fot this, the wavepacket in adiabatic representation $\Psi_{\text{adiabatic}}$ is obtained by unitary transformation from the diabatic representation by

$$\Psi_{\text{adiabatic}} = \mathbf{S}^\dagger \Psi_{\text{diabatic}}, \tag{3.16}$$

where **S** is the position dependent transformation matrix of adiabatic-diabatic representations defined in Eq. 3.11.

3.1.4 Ultrafast Coulomb explosion and correlated proton-hole dynamics

Figure 3.5 shows the electronic adiabatic states population during the first 60 fs after photoionization. We assume that the ionization cross-section is constant over the range of energies of the three considered electronic states and therefore the results are averaged over propagations starting from each of the three electronic states. In Fig. 3.5a the populations obtained from MCTDH wavepacket propagation are shown. One sees how after 10 to 20 fs the system has mostly decayed to the ground electronic state of the dication.

The agreement between the wavepacket and both types of surface-hopping calculations shown in Figs. 3.5b and 3.5c is rather good. The non-vanishing populations of states B_2 and A_1 reflect the fact that the outgoing H_2O^+ fragment can be in its ground electronic state in which the electron-hole corresponds to a π-type orbital, but also to some extent in the first and second excited electronic states, in which the hole is found on the plane of the water cation.

Fig. 3.6 depicts the reduced densities in the z and R coordinates obtained from the MCTDH calculation after tracing over the rest of vibrational modes and electronic states.

In order to quantify the correlated proton–hole dynamics we calculate the correlation function between the position of both particles. For the quantum mechanical case, the correlation function is defined as

$$C_{\mathrm{ph}} = S_{\mathrm{ph}} / \sqrt{S_{\mathrm{pp}} S_{\mathrm{hh}}}\,, \tag{3.17}$$

with $S_{xy} = \langle \hat{x}\hat{y} \rangle - \langle \hat{x} \rangle \langle \hat{y} \rangle$. The proton-hole correlation function is calculated in the surface-hopping case analogously by substituting operators by variables and wavefunction averages by ensemble averages over propagated trajectories. C_{ph} is bound to take values between -1, complete anti-correlation, and +1, complete correlation. For the excess proton position we take the projection of the central proton position onto the oxygen-oxygen axis. The electron hole position operator is defined as

$$\hat{h} = \frac{1}{2} \hat{R} \otimes \left(|r\rangle\langle r| - |l\rangle\langle l| \right) \tag{3.18}$$

for the wavepacket calculations, where $|l\rangle$ and $|r\rangle$ refer to the two diabatic electronic states with the hole localized on the left- and on the right-hand side water monomers,

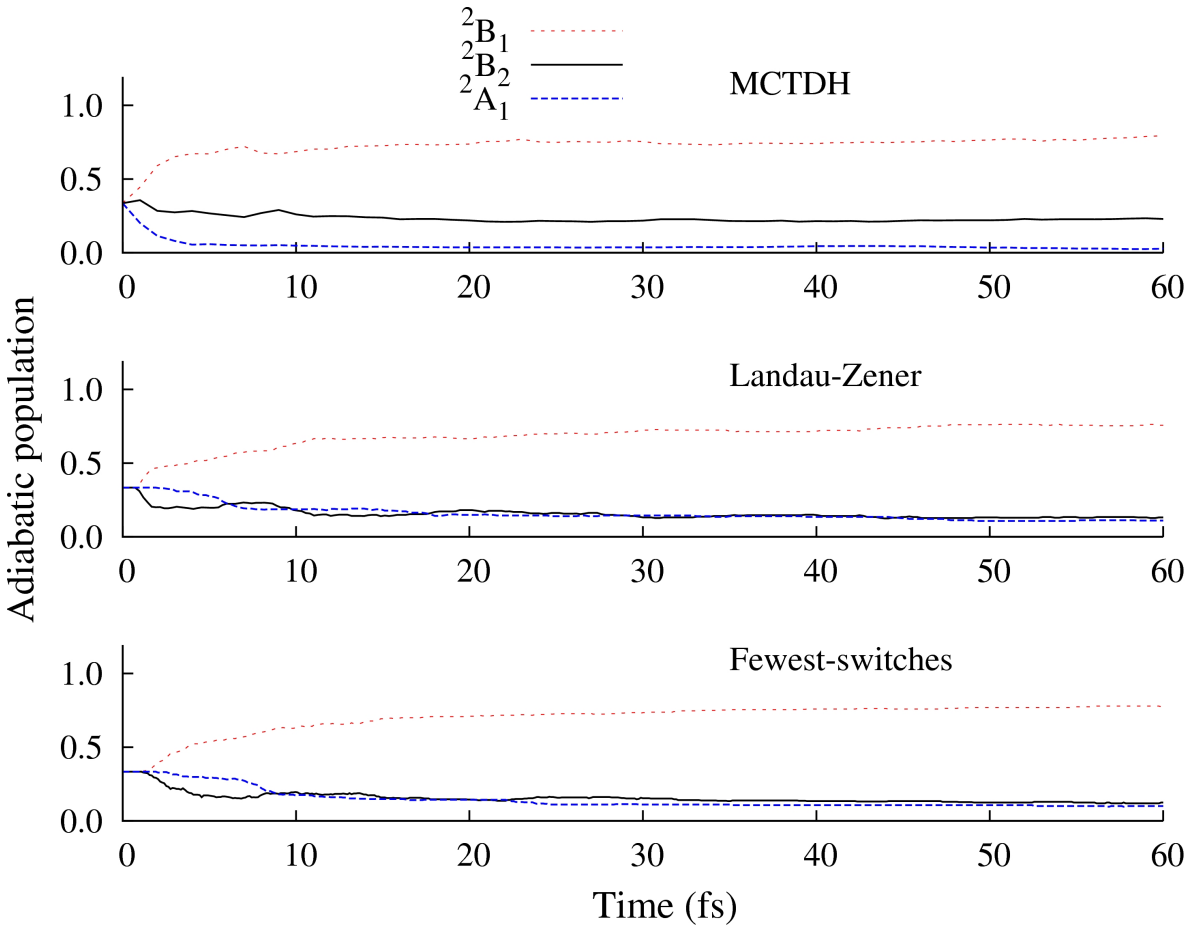

Figure 3.5: The temporal population of the three lowest-energy electronic states in adiabatic representation, calculated from Landau-Zener/fewest-switches surface hopping and MCTDH method, respectively. This figure is taken from Ref. [34]. Copyright © 2013 American Institute of Physics (AIP).

respectively, and $\hat{R}$ is the position operator corresponding to the oxygen-oxygen distance. In the quantum-classical surface-hopping scenario, we represent the hole straightforwardly as the center of the singly occupied molecular orbital associated with the electronic state on which a particular trajectory is being propagated.

In the Coulomb explosion, as the two like-charged particles, namely the proton and the electron-hole, should be forced to separate due to Coulomb repulsion, a general anti-correlation should be expected that $C_{\mathrm{ph}} \leq 0$. As shown in Fig. 3.7, the proton and hole develop the anti-correlation rapidly within 5 fs, which is a natural consequence of the strong Coulomb force. However, the emergence of correlation revival at $\sim$ 10fs appears clearly in both quantum-classical and quantum mechanical scenario, with striking quantitative

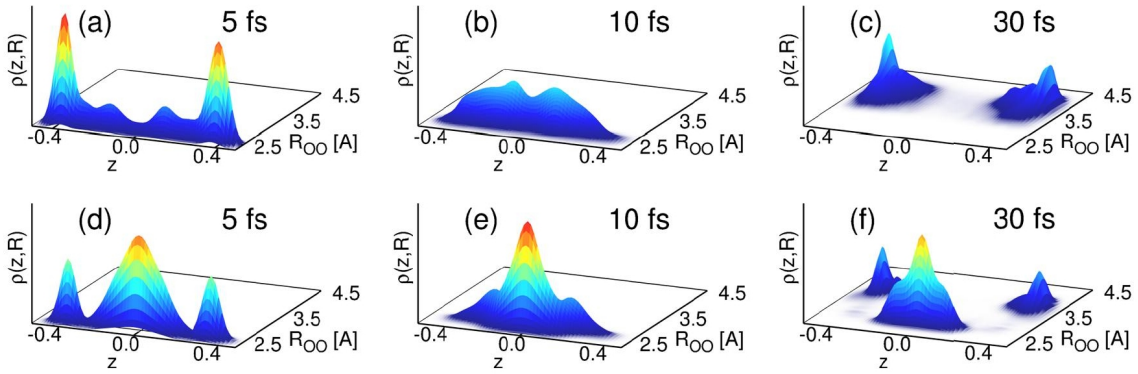

Figure 3.6: Reduced densities in the z (central proton position projected onto the oxygen-oxygen axis) and R (oxygen-oxygen distance) coordinates obtained from the MCTDH calculation after tracing over the rest vibrational modes and all electronic states. The lower panel corresponds to the case in which non-adiabatic coupling is switched off in the Hamiltonian, while the upper panel corresponds to the fully coupled case. This figure is taken from Ref. [30]. Copyright © 2013 American Physical Society (APS).

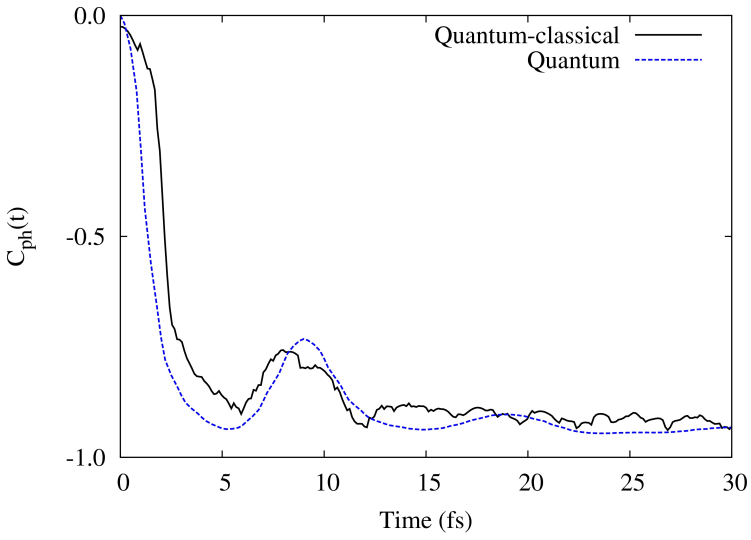

Figure 3.7: Correlation function between proton and electron-hole positions obtained from MCTDH and surface-hopping calculations. This figure is taken from Ref. [34]. Copyright © 2013 American Institute of Physics (AIP).

match of the two approaches. The revival is due to the bounce-back dynamics of both proton and hole in the first 10 fs before the water molecules had time to separate.

Thereafter the dication breaks apart with proton and hole localized on either of the separating fragments. This process is made explicit by direct visualization of the proton-hole motion of one of the surface-hopping trajectories in Fig. 3.8. The time scale of 5 fs appears as a lower limit for the ultrafast response of nuclei to an electron hole in a molecular system.

3.1.5 Photoionization spectrum

The photoionization (PI) spectrum was computed by Fourier transform of the autocorrelation function of the propagated wavepacket [53]

$$I(E) \sim E \int_{-\infty}^{\infty} dt \ \langle \Psi(0) \,|\, \Psi(t) \rangle \, e^{iEt}, \tag{3.19}$$

where E is the ionization energy. Since we are considering an irreversible process, the spectral features will have an intrinsic width that directly depends on the time-scale of the Coulomb explosion.

Figure 3.9a shows the PI spectrum obtained by propagation with the adiabatic Hamiltonian and neglecting the non-adiabatic coupling between the different electronic states. The individual spectra were obtained by populating each of the electronic states at $t = 0$ and incoherently summing to provide the total spectrum. The dotted line relates to the two lowest electronic states of the dication. As discussed above, ionization and further evolution in the lowest electronic state leads to an ultrafast fragmentation. This corresponds to the broad feature between 20 and 21 eV, which fully develops in the first 10 fs. In particular, the FWHM of the peak ($\sim$ 0.6 eV) corresponds to a process with time scale of $\sim$ 12 fs, implying rapid fragmentation after the photoionization. Above 21 eV the spectrum abruptly transitions into a region with bound vibrational states supported above the lower energy conical intersection. The separation between the peaks is about 650 cm^{-1} (81 meV), corresponding to bound water-water vibration. The shoulder above 22 eV corresponds to a small fraction of the wavepacket that finds its way into the fragmentation channel from

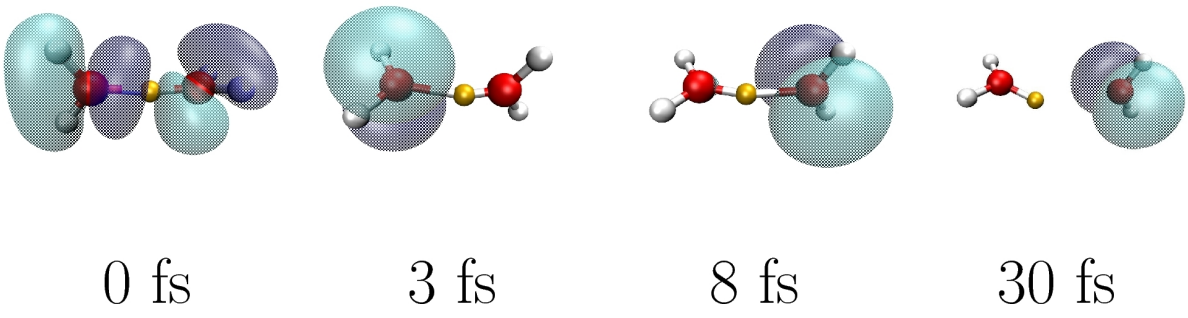

Figure 3.8: Direct visualization of motion for the proton (orange) and the electron-hole (blue and green for positive and negative wavefunction values respectively), when initialized from S_{A_1} state. The geometries were taken at 0, 3, 8 and 30 fs (from left). This figure is taken from Ref. [34]. Copyright © 2013 American Institute of Physics (AIP).

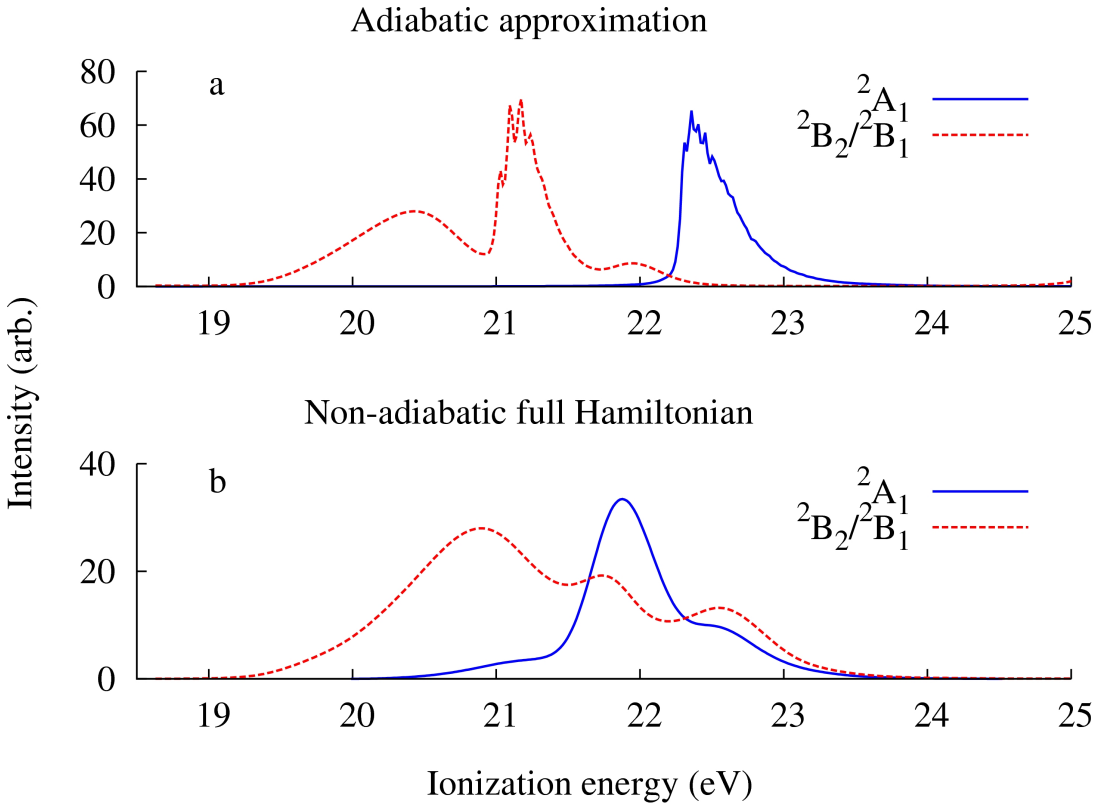

Figure 3.9: The photoionization spectra calculated from adiabatic dynamics (upper panel), and from non-adiabatic dynamics (lower panel).This figure is taken from Ref. [34]. Copyright © 2013 American Institute of Physics (AIP).

the first excited state of the dication. The solid line in Fig. 3.9a corresponds to ionization into the second excited electronic state of the dication. Bound vibrational states exist on its PES, as seen by the peaks in the spectrum at about 23 eV. Hence, even though the $H_5O_2^{2+}$is doubly charged, the missing non-adiabatic coupling between nuclei and electrons can significantly prevent the Zundel dication from fragmenting and relaxing via Coulomb repulsion. The calculation of the PI spectrum with the full vibronic Hamiltonian results in a broad, continuous band with three differentiated peaks in the range 20-24 eV as shown in Fig. 3.9b. This feature arises from the strong mixing of the three lowest electronic states of the dication, and the fact that in the coupled case the dication has no bound vibrational states. The two peaks at higher energy are slightly narrower than the lowest energy peak, which indicates a slightly larger fragmentation time from the continuum of states above the region of conical intersection. By comparison to the spectrum in Fig. 3.9a, these two broad peaks can be assigned to the continuum of vibronic states associated with the first and second excited electronic states of the dication.

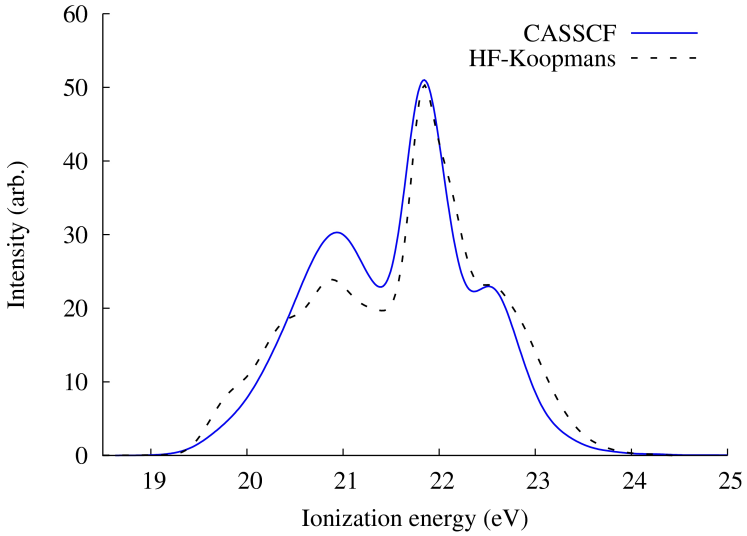

Figure 3.10: The comparison of the photoelectron spectra calculated from the Hartree-Fock-Koopmans potentials and from the CASSCF-corrected potentials. An ionization energy correction of -0.87 eV was consistently applied to the spectra from Hartree-Fock-Koopmans potential.This figure is taken from Ref. [34]. Copyright © 2013 American Institute of Physics (AIP).

To conclude this discussion, Fig. 3.10 presents the comparison of the PI spectrum calculated on the set of PESs at the CASSCF level discussed above, and at the Hartree-Fock-Koopmans level of theory. The latest was shifted by -0.87 eV for comparison to the CASSCF one. It is interesting to note that the two spectra are very similar in their features and intensities. This indicates that Hartree-Fock-Koopmans potentials reproduce remarkably well the conical intersections and overall shape of the PES at least in the vicinity of the Franck-Condon region. Indeed, we had already pointed out to the fact that the outer-valence ionized electronic states under consideration are mostly of one-hole character. This observation would open the door to the investigation of outer-valence ionization of larger water clusters based on the use of Hartree-Fock-Koopmans PESs.

3.1.6 Kinetic energy release of the fragments

The kinetic energy release (KER) spectrum reflects the asymptotic energy redistribution between the fragmentation mode, in this case the water-water distance coordinate, and the internal coordinates of the fragments. In Fig. 3.11 we present the KER of the H_3^+O and H_2O^+ fragments obtained from the 7D quantum dynamical calculation, as well as from reduced 7D and full dimensional models using the surface-hopping method. In the wavepacket calculation, the KER spectrum is obtained from the quantum flux analysis of the outgoing wavepacket through a complex absorbing potential placed in the outgoing channel [23].

In general, the KER spectrum can be measured in coincidence with the photoelectron (PE), or as integrated quantity over the PE energies. The KER spectrum contains complementary information, namely how the energy initially deposited in the system redistributes

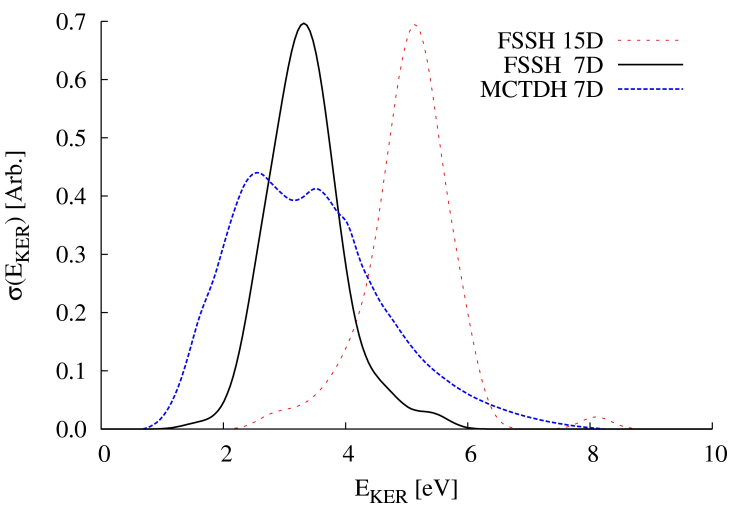

Figure 3.11: The kinetic energy release (KER) spectra of the outgoing fragments H_3^+O and H_2O^+ after tracing over the three lowest energy states, obtained from full dimensional quantum-classical treatment, and reduced dimensional quantum-classical/quantum-mechanical treatment, respectively. This figure is taken from Ref. [34]. Copyright © 2013 American Institute of Physics (AIP).

among translational energy of the fragments and the rest of degrees of freedom during the molecular fragmentation. It is clear that there is qualitative shift of the KER profile to higher energies in the 15D case, which indicates energy flow from internal modes of the monomer to the relative motion between the monomers. The broader envelope of the quantum KER spectrum is probably a consequence of the initial conditions sampling in the surface-hopping calculations, which are not able to capture zero point energy effects. One could also expect that the quantum mechanical KER spectrum will broaden if a full-dimensional model would be used. This result indicates the dimensionality matters when treating the long-time behavior of a fragmenting polyatomic system.

3.1.7 Ionization into the higher outer–valence ionic states

To a good approximation, each water molecule in the Zundel cation contributes three outer-valence orbitals with six electrons to the cluster. Therefore, there exist three further excited electronic states of $H_5O_2^{2+}$of outer-valence character above the three lowest states considered up to now. However, it becomes increasingly cumbersome to obtain a diabatic representation of the Hamiltonian with even more coupled states for a quantum-dynamical treatment, and moreover the upper states lead to further fragmentation channels beyond the two body fragmentation discussed above, which would require a full dimensional treatment and very extended grids. Such type of calculations are not within reach at the moment. Therefore, we study the dynamics in the complete outer-valence set of lowest energy electronic states of $H_5O_2^{2+}$using surface-hopping. The six lowest energy electronic states of $H_5O_2^{2+}$span the range of ionization potential at the Franck-Condon point from 20.6 eV to 27.4 eV calculated at the CASSCF level. The six states are predominantly one-hole

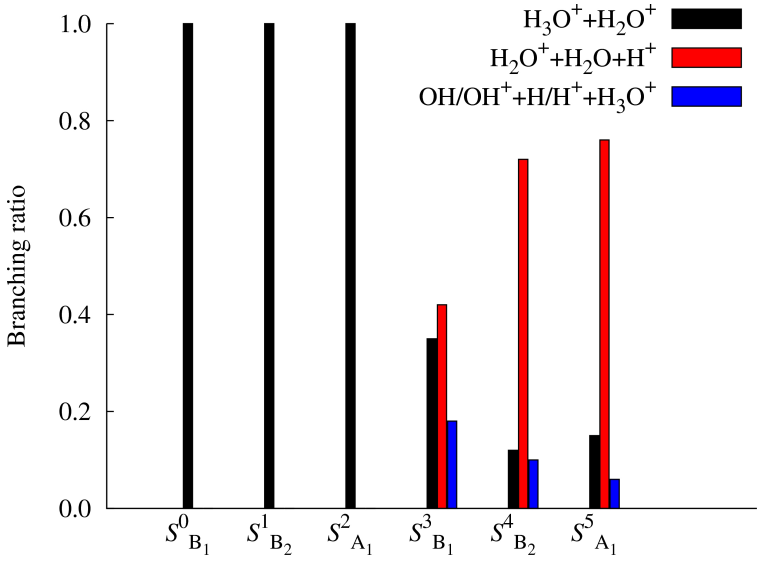

Figure 3.12: Branching ratio of two- and three-fragment channels, initialized from outer-valence ionic states. This figure is taken from Ref. [34]. Copyright © 2013 American Institute of Physics (AIP).

states, and only states above the set of outer-valence states involve one-particle-two-hole configurations in which one electron is further excited to an unoccupied orbital. For such higher-energy inner-valence states the Koopmans theorem no longer applies, due to growing importance of 2-particle-1-hole (2p1h) and higher order electronic configurations as illustrated in Eq. 2.60.

Fig. 3.12 presents the branching ratios of several two- and three-body channels calculated by surface hopping. With higher initial electronic excitation, it is natural to expect that more channels are energetically accessible. In contrast to the dynamics initialized from the three low-energy ionic states, which merely gives two-body fragmentation

$$H^+(H_2O)_2 + \gamma \rightarrow H_2O^+ + H_3O^+ + e^-,$$

the branching ratio of three-body fragmentation channels

$$H^+(H_2O)_2 + \gamma \rightarrow H^+ + H_2O + H_2O^+ + e^-$$

$$H^+(H_2O)_2 + \gamma \rightarrow H^+ + OH + H_3O^+ + e^-$$

$$H^+(H_2O)_2 + \gamma \rightarrow H + OH^+ + H_3O^+ + e^-$$

becomes important and can even exceed that of the two-body channel. We conclude that photons under about 24 eV will lead in all cases to a fast two-body fragmentation of the cluster. An increase in energy to about 27 eV, in which still the outer-valence is being ionized, will lead to further fragmentation channels in which the external hydrogen atoms of the cluster can be ejected during the Coulomb explosion.

So far we have thoroughly investigated the strongly non-adiabatic Coulomb explosion of the Zundel cation after outer-valence ionization by XUV light. We have analyzed in detail

the mechanism of fragmentation in the three lowest energy electronic states of $H_5O_2^{2+}$. For this set of electronic states, we constructed a diabatic Hamiltonian in 7D from CASSCF quality PESs, which was used in quantum-dynamical calculations of the fragmentation process with the MCTDH method. We found that the three lowest electronic states are coupled by strong non-adiabatic effects in which the motion of the central proton along the hydrogen bond between the two water molecules plays a fundamental role. When the dynamics after ionization were analyzed, we found a fast and anti-correlated motion of the central proton and the electron-hole that localizes them at opposite sides of the cluster and leads to a Coulomb explosion within femtoseconds. Exactly the same mechanism and time-scales were reproduced by surface-hopping calculations on PESs of the same quality. The vibrationally resolved photoionization spectrum of the cluster was also provided for the first time in the range between 19 to 24 eV by quantum-dynamical calculations. This energy range covers the lowest energy part of the outer-valence spectrum, which extends up to about 27 eV. The complete outer-valence ionized states of $H_5O_2^{2+}$comprises six electronic states. The dynamics in this set of coupled electronic states was calculated by surface-hopping. We found that above the lowest three electronic states, fragmentation into other than the two-body channel is possible and even dominant. The dynamics starting from the upper states are also strongly non-adiabatic and a large fraction of the initially available electronic energy is redistributed into vibrational modes, which explains the possibility of further fragmentation channels.

The calculations provide an in-deep analysis of the coupled electronic and nuclear non-Born-Oppenheimer dynamics in a small ionized water cluster, in which the high mobility of proton and electron-hole plays a fundamental role. The good agreement between quantum and surface-hopping treatments paves the way for future explorations of larger clusters and the liquid phase.

3.2 Hole dynamics tracked by transient absorption spectroscopy

As we can see from Section 3.1, the non-adiabatic effect can result in qualitatively different dynamics of molecules, as compared to the case of merely taking Born–Oppenheimer approximation. In the non-Born-Oppenheimer chemical reactions, molecular nuclei can switch and move within multiple vibronically coupled electronic states. The ultrafast non-adiabatic energy transfer between nuclei and electrons on the sub-100-femtosecond scale can essentially modify the mechanisms of chemical reaction.

When a molecule is ionized, the created electron hole will undergo complex mechanism

to relax and migrate [30, 34, 54], in order to reach energetically favorable configurations. The electron hole dynamics, essentially non-adiabatic, has profound impact upon complex molecular system, such as the well known DNA self-protection mechanism against the ultraviolet component in sunlight [11].

How do the electrons and nuclei correlate, when both are in motion? A typical question would address the transient electron hole states on which nuclear conformation variation is taking place during electronic decay. A direct on-the-fly probing of the coupled electronic and nuclear wave-packets should be the key to resolve the full scenario of the non-Born-Oppenheimer dynamics in polyatomic molecules. As an example, high harmonic generation (HHG) [12, 55], Coulomb explosion imaging [56, 57], and time-resolved photoelectron spectroscopy (TRPES) [58, 59, 60, 61] have been developed and elegantly applied as powerful tools to map out the dynamics of the excited electrons and the associated nuclear motion. Moreover, the core level transient absorption spectroscopy may be suitable to map out the dynamics of electron holes, using the electronic transitions from core orbital to the valence holes. Meanwhile, to probe dynamics in condensed phase bulk samples, it is advantageous to apply the photon-absorption/scattering based methods, such as nonlinear coherent spectroscopy [62, 63, 64, 65], x-ray absorption and Raman spectroscopy [66, 67].

In the present section, we are going to address the question, "*How to directly observe the non-Born-Oppenheimer valence hole dynamics and relaxation in an ionized complex molecular system ?*" Here we theoretically study the application of a photon based technique, the core-level transient absorption spectroscopy [68, 69, 70, 71, 72, 73, 74], to disentangle the coupled electronic and nuclear dynamics, and map out the non-adiabatic electronic decay to time resolvable spectroscopic signatures. In core-level transient absorption spectroscopy, a time-delayed x-ray probe pulse projects the evolving nuclear and electronic wave-packet of the photoionized molecule onto core-hole states, and the transient absorbance is analyzed as a function of pump-probe delay. The core-hole states are used as reference for projecting out the electronic and nuclear components of the wave-packet. As an example, one could simply expect a shift of absorption energy with time as electronic dynamics in the valence shell progresses. The advantage of core-level spectroscopy relies on the fact that the deeply embedded atomic core orbitals are less perturbed by the molecular environment than the valence orbitals, thus the core-valence-hole transitions are element specific and offer clean spectroscopic signatures for the on-going dynamics. Most importantly, the photon based transient absorption spectroscopy (itself) is a general technique that can be conveniently applied to a wide scope of atomic and molecular systems in either gas or condensed phase. Either free-electron laser or high-order harmonics source could be applied as the probe pulse [70].

By correlating the transient absorption spectra with the nuclear dynamics obtained

from quantum wave-packet and quantum-classical approaches, we are able to depict a complete mechanism for the non-adiabatic chemical reactions. The protonated water multimers $H^+(H_2O)_n$ offer an ideal test ground for the impact of the non-Born-Oppenheimer effect on nuclear and electronic dynamics. Despite the importance of the $H^+(H_2O)_n$ as possible building blocks of aqueous acids [75, 76], the dicationic molecules created from photoionization of $H^+(H_2O)_n$ will undergo an ultrafast charge separation of the proton and molecular fragments carrying the hole, which are both positively charged, accompanied by non-adiabatic electronic decay from excited ionic states [34, 77]. As a consequence of Coulomb repulsion, the proton wave-packet is actually driven by the motion of the valence-hole, which together produce highly coupled electronic and nuclear dynamics on the 100 fs scale.

Nuclear dynamics of photoionized $H^+(H_2O)_n$ is calculated using quantum-classical surface hopping scheme [27, 78], where nuclei are treated classically. The electronic structure is computed using the quantum chemistry package `MOLCAS` [79]. For the Zundel dication, we had in the previous study employed multiconfigurational time-dependent Hartree (MCTDH) method to access the quantum nuclear wave-packet dynamics [23, 46, 77]. Based on our comparative study with quantum mechanical method [34], the quantum-classical method is able to reliably resolve the physical scenario of electron hole relaxation in the Zundel dication. We assume sudden ionization of the molecule, and again invoke the expansion of the wavefunction at time τ after photoionization as Eq. 2.3.The time-domain expression for the transient absorption spectrum (TAS) of a non-stationary wavepacket $\chi_1(\mathbf{R},\tau)$ evolving on the PES $E_1(\mathbf{R})$ and probed by an electronic transition to electronic state 2 is given by [80]

$$\sigma(\omega,\tau) = \frac{4\pi\omega}{c}\int \mathrm{d}\mathbf{R}|\mu_{12}(\mathbf{R})|^2|\chi_1(\mathbf{R},\tau)|^2\frac{\Gamma/2}{\Gamma^2/4+[E_1(\mathbf{R})-E_2(\mathbf{R})-\omega]^2},$$

where

$$\mu_{12}(\mathbf{R}) = \langle\Psi_1(\mathbf{r};\mathbf{R})|\hat{\mu}_{12}|\Psi_2(\mathbf{r};\mathbf{R})\rangle \tag{3.20}$$

is the transition dipole matrix element between the electronic states involved. Equation 3.20 corresponds to the so-called Lorentzian limit in which dephasing of the nuclear wavepackets evolving on PES $E_1(\mathbf{R})$ and $E_2(\mathbf{R})$ is assumed to be fast in comparison to the time-scale of atomic motions. A short probe pulse is also assumed in obtaining this expression [80]. Basically, the cross-section corresponds to the transition dipole matrix element squared between two electronic states, averaged by the probability density in nuclear coordinate space and broadened by the lifetime of the final electronic state. This limit is meaningful in the present situation of core-level TAS due to large topological differences between PES of valence- and core-hole states, leading to fast dephasing, as well as the

presence of purely electronic decay mechanisms, like Auger decay, for the core-hole final states.

Equation 3.20 can be readily used within a surface-hopping framework. At every time τ the integral over configurational space is substituted by a sum over the swarm of classical trajectories. Each trajectory is found at one of the valence electronic states of the system whose dynamics are being probed, and we denote the index of the electronic state of trajectory J at time τ as $j(J,\tau)$. In addition, instead of a single final electronic state for the probe step, one needs to consider all possible transitions from the valence-hole state to core-hole states accessible in the energy range of interest. With these considerations our final working equation for the absorption cross-section reads

$$\sigma(\omega,\tau) = \frac{4\pi\omega}{c}\frac{1}{M}\sum_{J}^{M}\sum_{\alpha}\left\{|\mu_{j(J,\tau),\alpha}(\mathbf{R}_J)|^2\frac{\Gamma/2}{\Gamma^2/4+[E_\alpha(\mathbf{R}_J)-E_{j(J,\tau)}(\mathbf{R}_J)-\omega]^2}\right\}. \quad (3.21)$$

where α denotes the final core-hole electronic state, $\mathbf{R}_J \equiv \mathbf{R}_J(\tau)$ and M is the total number of trajectories. For core-level TAS Γ can be chosen to be of the order of the linewidth of the relevant core-hole state, e.g. O1s^{-1} in the present case. The linewidth of O1s^{-1} is measured to be 160$\pm$5 meV corresponding to a lifetime of about 4.1 fs [81]. The probability of nuclear wavefunctions $|\chi_J(\mathbf{Q},\tau)|^2$ is taken as the incoherent sum of nuclear trajectories.

We find that the non-adiabatic electronic decay from highly excited states is cleanly reflected by the shift of absorption to higher energies on the scale of $\sim$ 10 eV, which corresponds to the energy span of outer valence states. Moreover, the spectra intensity evolution can be considered as sensitive signature of electron hole localization following photoionization from hydrogen bonding bridge to the water monomer, while similar electron localization phenomena have been reported in previous studies [82, 83]. We have also observed intriguing imprints of intramolecular vibrational modes and collective motions on the spectra. All the spectroscopic features could be considered as experimentally accessible, provided $\lesssim$ 10 eV spectra resolution is available [70].

3.2.1 Spectra of photoionized Zundel cation

Zundel cation $H^+(H_2O)_2$ is a prototypical water multimer. It is known the breakdown of Born-Oppenheimer approximation plays a crucial role in its relaxation mechanism [29, 34, 77]. By absorbing extreme ultraviolet (XUV) photon, one is able to generate dicationic $H_5O_2{}^{2+}$with a valence electron hole. The nuclear motion correlates after photoionization with ultrafast electronic decay, leading to shift of transient absorption lines and evolution of spectral intensity (Fig. 3.13).

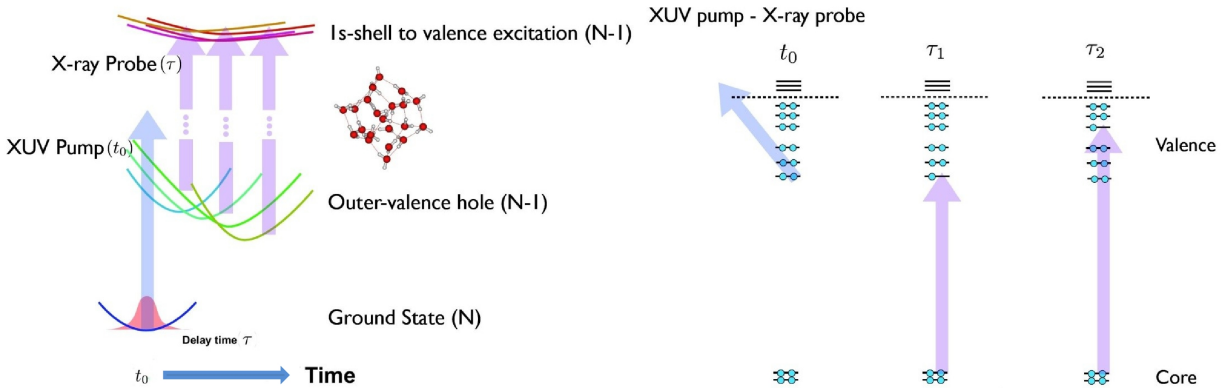

Figure 3.13: The schematic representation of the core level transient absorption spectroscopy. The spectral shift due to electronic relaxation is illustrated.

The most prominent feature of the spectra (Fig. 3.14) is the vanishing of absorption lines initially appearing at low energies, due to the enlarged energy spacing between the oxygen K-shell core-hole state and the valence-hole state, as the valence-hole state decays downwards to the dicationic ground state. The total energy shift is $\sim$ 6 eV, correlating very well with the energy span of the first six low-lying valence-hole states.

The variation of spectral intensity and line position can unravel more subtle scenario of the electronic and nuclear motion. The proton and hole separate within few femtoseconds as a consequence of strong electrostatic repulsion between them, implying rapid decay from higher valence-hole states with overlapping proton and hole wavefunctions to lower valence-hole states with localized proton and hole. The delocalization of the valence-hole wavefunction is clearly reflected in the transient absorption spectra within first 15 fs. Since the strength of transition dipole integral $\langle \phi_J(\mathbf{q};\mathbf{Q}) \left|\hat{\mu}\right| \phi_\alpha(\mathbf{q};\mathbf{Q})\rangle$ can certainly be enhanced as the wavefunction of core-hole state $|\phi_\alpha(\mathbf{q};\mathbf{Q})\rangle$ and valence-hole state $|\phi_J(\mathbf{q};\mathbf{Q})\rangle$ come spatially close, the delocalization of valence-hole from the hydrogen bonding bridge to the water monomers leads to rapid rise of absorption intensity. It can be made clearer by inspecting the temporal wavefunction evolution [77], even the transient period of electon hole localization ($\sim$ 5 fs), delocalization ($\sim$ 10 fs) and re-localization process is imprinted in the tiny revival structure in the spectrogram within first 15 fs. The localization of electron hole is reflected in the enhancement of absorption strength, since the core electron and the valence hole come spatially close as the hole and proton reside locally on the water monomers. The transient period features the quasi-bound state for the dication in the Frank-Condon region, and is also reflected by the single-period oscillation of the proton on the hydrogen bonding bridge at exactly the same time, driving the motion of the electron hole. The dynamics is essentially originated from the fact, that the motion of positively charged proton and electron hole are anti-correlated due to Coulomb repulsion, as

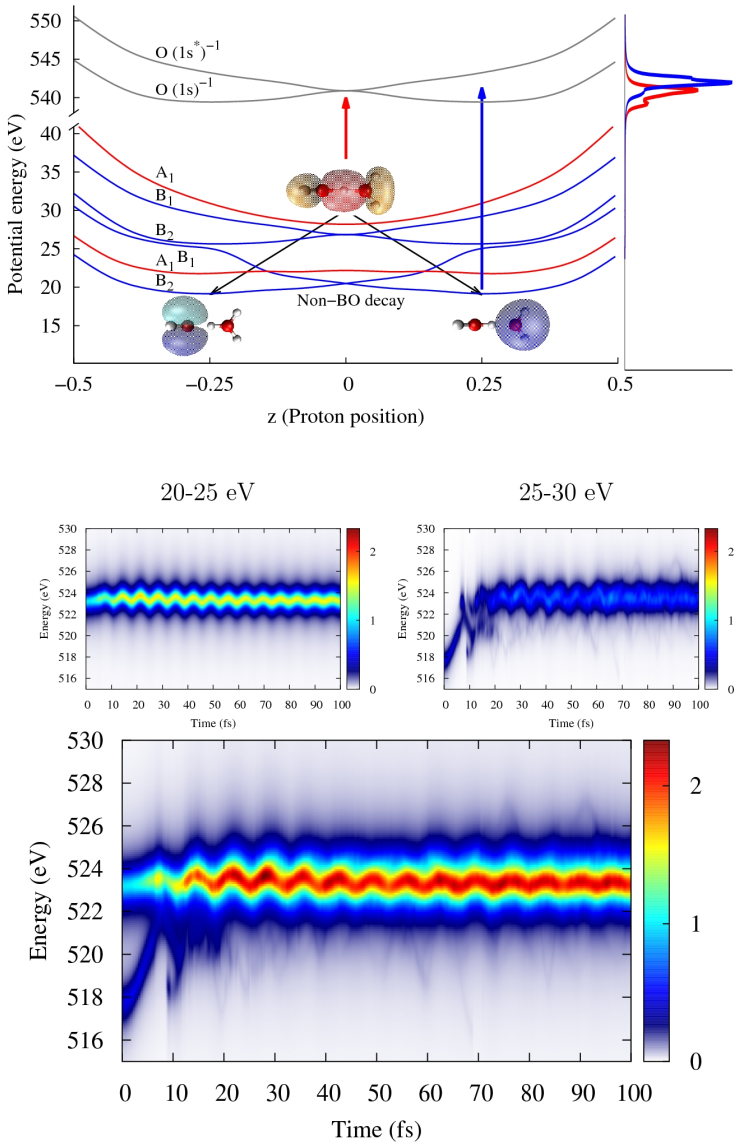

Figure 3.14: The transient absorption spectra of the Zundel dication undergoing Coulomb explosion (lower panel). Reduced densities in the z (central proton position projected onto the oxygen-oxygen axis) and R (oxygen-oxygen distance) coordinates obtained from the quantum wave-packet calculation after tracing over the rest vibrational modes and all electronic states (upper panel).

demonstrated in the proton-hole correlation function $C_{\mathrm{ph}}(t)$ defined in Eq. 3.17, which also shows quantitative agreement of quantal and quantum-classical nuclear dynamics [34, 77].

The obvious oscillation of the spectra center until $\sim$ 100 fs should be another intriguing feature of the transient absorption spectra for the photoionized Zundel cation. The spectra oscillation with Fourier frequency of $\sim$ 3300 cm^{-1} (0.41 eV) can be assigned to the modulation by coherent vibration of hydroxyl group (OH) in water molecules. It is evident that the spectra have recorded $\sim$ 100 fs long vibrational quantum coherence created by suddenly depleting the molecule to the dicationic state. Because photoionization actually appears in much shorter (attosecond) time scale than the vibrational motion, it plays the role in synchronization of vibrational phase of the nuclear wave-packet.

With analog to the formation of energy bands in solids, for the multimers $H^+(H_2O)_n$ with $n > 2$ [84], an enlarged set of molecular valence orbitals are squeezed into a slightly increased energy span to build electronic states supporting the valence-hole. One could expect the growth of stability as more water molecules are added into the multimer, since there is more space for the proton and the electron hole to separate from each other, and more nuclear degrees of freedom to absorb the energy released from the electronic decay. The build-up of extended hydrogen-bonding network may also stablize the multimer. For water multimers, the outer–valence shell can be thought of as being composed of $3n$ molecular orbitals, where n is the number of water molecules in the multimer, because the outer–valence shell is formed by the 3 of sp^3 hybridized molecular orbitals of water, that carry mainly O2p character. With the number of water molecules reaching 21, the protonated 21-mer $H^+(H_2O)_{21}$, firstly discovered by electrospray mass spectrometry [85], acquires intriguing magic number stability [86, 87, 88] The $H^+(H_2O)_{21}$ molecule can be depicted as a nearly spherical cage with an enclosed water monomer, it is an abundant species in water vapor and may contribute to the intense terahertz emission of water vapor under optical excitation [89].

3.2.2 Spectra of photoionized $H^+(H_2O)_{21}$

With in-depth understanding of transient absorption spectra for the fundamental Zundel dication in hand, the spectra for the more complicated protonated 21-mer dication $H(H_2O)_{21}^{2+}$ can be faithfully interpreted. Counter-intuitively, for the protonated 21-mer, the symmetric structure of an enclosed hydronium H_3^+O cation inside the cage was not found in *ab initio* search, instead the molecule favors a surface-protonated cage with a neutral water in the center [84, 90, 91], which is confirmed experimentally [92].

The surface-protonation has a crucial impact on the nuclear dynamics and stabilization of the protonated 21-mer after photoionization. Because the upper energy subshell corresponds to the 21 valence hole states with reduced density on the lone electron pair of water molecule, the electron hole of these valence states are associated to the hydronium cation. As a natural consequence, the electron hole in highly excited dicationic states attaches to the hydronium, the initial Coulomb force is directly imposed on the surface, and makes the surface more likely to break.

The associated transient absorption spectra offers possibility to trace the whole nuclear and electronic dynamics to its subtlety (Fig. 3.15). The most prominent character of the spectra is the temporal shift of $\sim$ 10 eV to higher energies, obviously due to the non-adiabatic electronic decay. Moreover, one could easily spot a relatively large upward leap of spectra profile of $\sim$ 2 eV at $\sim$ 10 – 30 fs. By inspecting the electronic potential

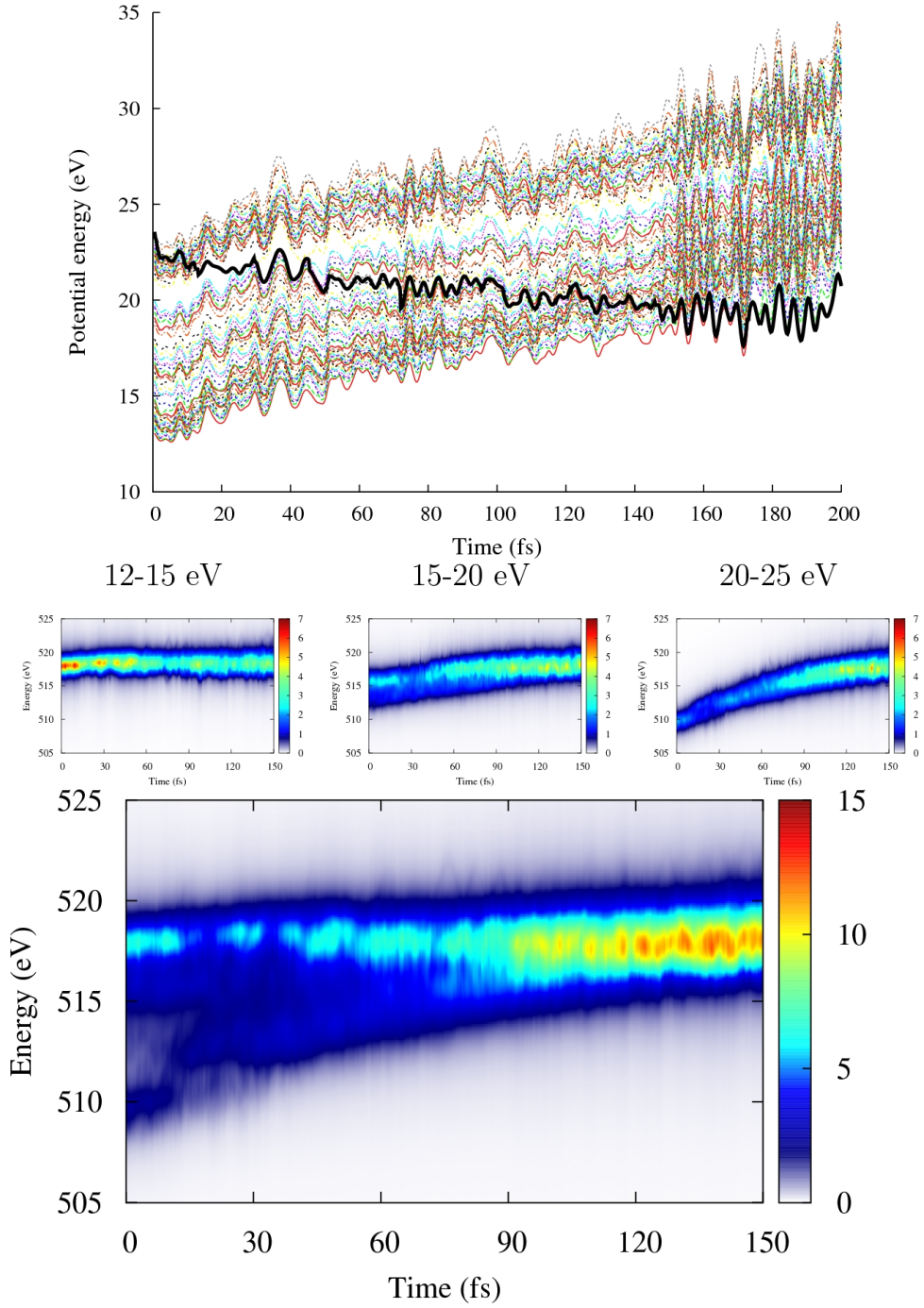

Figure 3.15: The potential energy of all 63 valence states of $H(H_2O)_{21}^{2+}$ dication (upper panel), and the transient absorption spectra of the $H(H_2O)_{21}^{2+}$ dication after photoionization (middle and lower panel). The potential energy evolution is plotted for a single trajectory initialized from the 62^{th} initial electronic state. The black solid curve shows the non-adiabatic descending path in the valence shell the dicationic system follows. The spectra are shown separately according to energy span of the initial ionization pulse (middle panel), and as integral spectra by incoherent summation (lower panel).

energies of the $H(H_2O)_{21}^{2+}$ dication (Fig. 3.15), one can immediately observe an energy gap of $\sim$ 2 eV inherited from the energy difference between the lone electron pair orbital and the covalent bonding orbitals of the sp^3 molecular orbitals in water, the latter supporting hydrogen bonding. The valence states that associates with the orbital purely carrying oxygen $2s$ character inherit large energy gap of $\sim$ 14 eV from the outer valence shell, thus are excluded in the present study. The spectral profile leap can then be unambiguously assigned to the transitions from valence hole states with reduced population in water sp^3 lone pair orbitals to those in H-O covalent bonding orbitals. Analogous to the transient absorption spectra of Zundel cation, the enhancement of spectral intensity at $\sim$ 100 eV may arise from the fact that the electron hole is more localized in the molecular fragments.

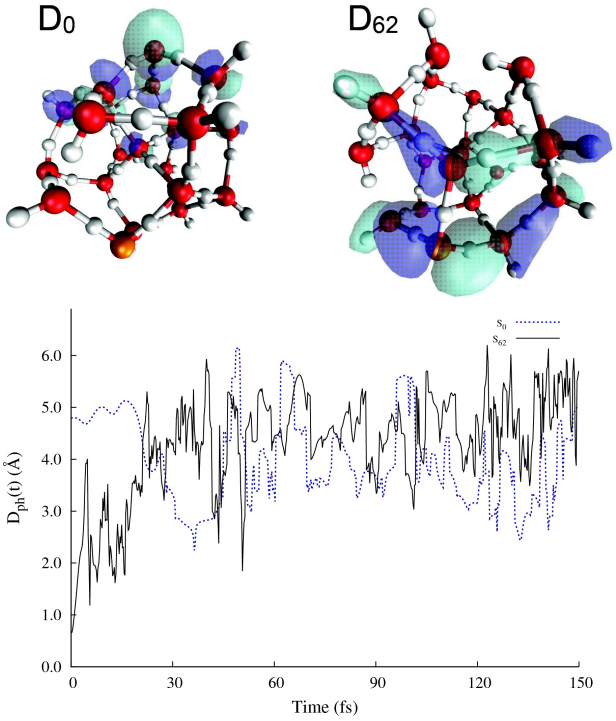

Figure 3.16: The evolution of proton-hole distance in the $H(H_2O)_{21}^{2+}$ dication after photoionization (lower panel), the initial positions of the proton (orange sphere) and the electron hole (blue and green for positive and negative wavefunction values respectively) are shown for the initial states at the top (S_{62}) and the bottom (S_0) of outer valence shell (upper panel).

Again we emphasize the underlying core mechanism dominating the whole dynamics in $H(H_2O)_{21}^{2+}$ dication, the Coulomb repulsion between the valence electron hole and the proton. It is easy to distinguish the hole state at the top and the bottom of the outer valence shell by inspecting whether the electron hole is located at the same side or opposite side of the excess proton. Shown in Fig. 3.16, when initializing from the top of the outer valence shell, the two charged particles experience larger acceleration as they are close on the sphere, since their spatial separation takes place immediately. However, the configuration at the bottom of the outer valence shell is almost well relaxed at the beginning, which exhibits oscillatory proton-hole distance in the following dynamics. Unlike the Zundel dication, the proton in the $H(H_2O)_{21}^{2+}$ dication has delocalized nature, since

the hydrogen atoms can move in a concerted way within the complex hydrogen bonding network, this makes the charge separation process in the $H(H_2O)_{21}^{2+}$ dication to happen in a more chaotic manner than that in the Zundel dication, despite the eventual relaxation with well separated proton and electron hole.

The core-level transient absorption spectroscopy technique can open up new possibilities to cleanly follow complex behavior of coupled electronic and nuclear dynamics in general non-Born-Oppenheimer processes. By correlating the electronic transient absorption spectra with the nuclear wave-packet, we have successfully demonstrated the clear resolution of electronic decay on sub-100-femtosecond time scale, and the subtle localization-delocalization dynamics of electronic dynamics. Since the nuclei are essentially moving in the electronic potential, the anti-correlated proton motion associated with the valence-hole wave-packet has been resolved in detail.

Making use of higher order photon scattering processes may also help to probe the non-adiabatic electronic and nuclear dynamics, for example, the resonant inelastic x-ray scattering spectroscopy (RIXS) should be a promising candidate for this purpose [93, 94, 95].

3.3 Bibliography

[1] A. L. Sobolewski, W. Domcke, and C. Hättig, Proc. Natl. Acad. Sci. **102**, 17903 (2005).

[2] G. A. Worth and C. L. S., Annu. Rev. Phys. Chem. **55**, 127 (2004).

[3] G. A. Worth, P. Hunt, and M. A. Robb, J. Phys. Chem. A **107**, 621 (2003).

[4] G. Worth and M. A. Robb, Adv. Chem. Phys. **124**, 355 (2002).

[5] H. C. Longuet-Higgins, U. Opik, M. H. L. Pryce, and R. A. Sack, Proc. R. Soc. Lond. A **244**, 1 (1958).

[6] H. Köppel, W. Domcke, and L. S. Cederbaum, Adv. Chem. Phys. **57**, 59 (1984).

[7] D. R. Yarkony, Rev. Mod. Phys. **68**, 985 (1996).

[8] D. R. Yarkony, Chem. Rev. **112**, 481 (2012).

[9] S. Pisana, M. Lazzeri, C. Casiraghi, K. Novoselov, A. Geim, A. Ferrari, and F. Mauri, Nature materials **6**, 198 (2007).

[10] H. Satzger, D. Townsend, M. Z. Zgierski, S. Patchkovskii, S. Ullrich, and A. Stolow, Proc. Natl. Acad. Sci. **103**, 10196 (2006).

[11] M. Barbatti, A. J. A. Aquino, J. J. Szymczak, D. Nachtigallová, P. Hobza, and H. Lischka, Proc. Natl. Acad. Sci. **107**, 21453 (2010).

[12] H. J. Wörner, J. B. Bertrand, D. V. Kartashov, P. B. Corkum, and D. M. Villeneuve, Nature **466**, 604 (2010).

[13] D. Polli, P. Altoe, O. Weingart, *et al.*, Nature **467**, 440 (2010).

[14] T. J. Martinez, Nature **467**, 412 (2010).

[15] V. I. Prokhorenko, A. M. Nagy, S. A. Waschuk, L. S. Brown, R. R. Birge, and R. J. D. Miller, Science **313**, 1257 (2006).

[16] T. Schultz, E. Samoylova, W. Radloff, I. Hertel, A. Sobolewski, and W. Domcke, Science **306**, 1765 (2004).

[17] J. D. Savee, V. A. Mozhayskiy, J. E. Mann, A. I. Krylov, and R. E. Continetti, Science **321**, 826 (2008).

[18] U. Manthe, H.-D. Meyer, and L. S. Cederbaum, J. Chem. Phys. **97**, 3199 (1992).

[19] Z. Vager, R. Naaman, and E. P. Kanter, Science **224**, 426 (1989).

[20] H. Shinohara, N. Nishi, and N. Washida, J. Chem. Phys. **84**, 5561 (1986).

[21] Y. V. Novakovskaya, Int. J. Quantum Chem. **107**, 2763 (2007).

[22] F. Dong, S. Heinbuch, J. J. Rocca, and E. R. Bernstein, J. Chem. Phys. **124**, 224319 (2006).

[23] M. H. Beck, A. Jäckle, G. A. Worth, and H.-D. Meyer, Phys. Rep. **324**, 1 (2000).

[24] W. H. Miller, J. Phys. Chem. A **105**, 2942 (2001).

[25] J. Jornet-Somoza, B. Lasorne, M. Robb, H. Meyer, D. Lauvergnat, and F. Gatti, J. Chem. Phys. **137**, 084304 (2012).

[26] I. Burghardt, K. Giri, and G. A. Worth, J. Chem. Phys. **129**, 174104 (2008).

[27] J. C. Tully, J. Chem. Phys. **93**, 1061 (1990).

[28] B. R. Landry and J. E. Subotnik, J. Chem. Phys. **135**, 191101 (2011).

[29] L. Lammich, C. Domesle, B. Jordon-Thaden, *et al.*, Phys. Rev. Lett. **105**, 253003 (2010).

[30] Z. Li, M. E. Madjet, O. Vendrell, and R. Santra, Phys. Rev. Lett. **110**, 038302 (2013).

[31] O. Vendrell, F. Gatti, D. Lauvergnat, and M. H.-D., J. Chem. Phys. **127**, 184302 (2007).

[32] L. Doriol, B. Lasorne, F. Gatti, M. Schröder, O. Vendrell, and H. Meyer, Comput. Theor. Chem. **990**, 75 (2012).

[33] O. Vendrell, M. Brill, F. Gatti, D. Lauvergnat, and H.-D. Meyer, J. Chem. Phys. **130**, 234305 (2009).

[34] Z. Li, M. E. Madjet, and O. Vendrell, J. Chem. Phys. **138**, 094311 (2013).

[35] B. O. Roos, P. R. Taylor, and P. E. M. Siegbahn, Chem. Phys. **48**, 157 (1980).

[36] P. E. M. Siegbahn, J. Almlöf, A. Heiberg, and B. O. Roos, J. Chem. Phys. **74**, 2384 (1981).

[37] T. H. Dunning, J. Chem. Phys. **90**, 1007 (1989).

[38] S. Carter, S. J. Culik, and J. M. Bowman, J. Chem. Phys. **107**, 10458 (1997).

[39] J. M. Bowman, S. Carter, and X. Huang, Int. Rev. Phys. Chem. **22**, 533 (2003).

[40] Z. H. Top and M. Baer, J. Chem. Phys. **66**, 1363 (1977).

[41] H. Köppel, J. Gronki, and S. Mahapatra, J. Chem. Phys. **115**, 2377 (2001).

[42] H. Köppel and B. Schubert, Mol. Phys. **104**, 1069 (2006).

[43] H. Köppel, Faraday Discuss. **127**, 35 (2004).

[44] E. V. Gromov, C. Lévêque, F. Gatti, I. Burghardt, and H. Köppel, J. Chem. Phys. **135**, 164305 (2011).

[45] H.-D. Meyer, F. Gatti, and G. Worth, eds., *Multidimensional Quantum Dynamics: MCTDH theory and its applications* (Wiley-VCH, 2009).

[46] G. A. Worth, M. H. Beck, A. Jäckle, and H.-D. Meyer, The MCTDH Package, Version 8.2, (2000). H.-D. Meyer, Version 8.3 (2002), Version 8.4 (2007). See http://mctdh.uni-hd.de.

[47] H.-D. Meyer and G. A. Worth, Theor. Chem. Acc. **109**, 251 (2003).

[48] H.-D. Meyer, F. Le Quéré, C. Léonard, and F. Gatti, Chem. Phys. **329**, 179 (2006).

[49] R. Kosloff and H. Tal-Ezer, Chem. Phys. Lett. **127**, 223 (1986).

[50] M. G. H. Boogaarts, P. C. Hinnen, and G. Meijer, Chem. Phys. Lett. **223**, 537 (1994).

[51] U. V. Riss and H.-D. Meyer, J. Chem. Phys. **105**, 1409 (1996).

[52] U. Manthe and H. Köppel, J. Chem. Phys. **93**, 345 (1990).

[53] D. Tannor, *Introduction to Quantum Mechanics: A Time-Dependent Perspective* (Macmillan, 2007).

[54] A. I. Kuleff and L. S. Cederbaum, Phys. Rev. Lett. **106**, 053001 (2011).

[55] W. Li, X. Zhou, R. Lock, S. Patchkovskii, A. Stolow, H. C. Kapteyn, and M. M. Murnane, Science **322**, 1207 (2008).

[56] Z. Vager, N. R., and E. P. Kanter, Science **244**, 426 (1989).

[57] M. Kotur, T. C. Weinacht, C. Zhou, and S. Matsika, IEEE J. Sel. Top. Quantum Electron. **18**, 187 (2012).

[58] A. Stolow and J. G. Underwood, Adv. Chem. Phys. **139**, 497 (2008).

[59] A. Stolow, A. E. Bragg, and D. M. Neumark, Chem. Rev. **104**, 1719 (2004).

[60] O. Geß ner, A. M. D. Lee, J. P. Shaffer, *et al.*, Science **311**, 219 (2006).

[61] V. Blanchet, Z. Zgierski, T. Seideman, and A. Stolow, Nature **401**, 52 (1999).

[62] S. Mukamel, *Principles of nonlinear optical spectroscopy (Oxford series on optical & imaging science 6)* (Oxford University Press, 1999).

[63] M. Kullmann, S. Ruetzel, J. Buback, P. Nuernberger, and T. Brixner, J. Am. Chem. Soc. **133**, 13074 (2011).

[64] N. Huse, B. D. Bruner, M. L. Cowan, J. Dreyer, E. T. J. Nibbering, R. J. D. Miller, and T. Elsaesser, Phys. Rev. Lett. **95**, 147402 (2005).

[65] M. L. Cowan, B. D. Bruner, N. Huse, *et al.*, Nature **434**, 199 (2005).

[66] P. Wernet, D. Nordlund, U. Bergmann, *et al.*, Science **304**, 995 (2004).

[67] C. Huang, K. T. Wikfeldt, T. Tokushima, *et al.*, Proc. Natl. Acad. Sci. , 15214 (2009).

[68] M. Dantus, M. J. Rosker, and A. H. Zewail, J. Chem. Phys. **87**, 2395 (1987).

[69] R. Santra, V. S. Yakovlev, T. Pfeifer, and Z.-H. Loh, Phys. Rev. A **83**, 033405 (2011).

[70] Z.-H. Loh and S. R. Leone, J. Chem. Phys. **128**, 204302 (2008).

[71] A. Wirth, M. Hassan, I. Grguraš, *et al.*, Science **334**, 195 (2011).

[72] S. Pabst, A. Sytcheva, A. Moulet, A. Wirth, E. Goulielmakis, and R. Santra, Phys. Rev. A **86**, 063411 (2012).

[73] L. Fang, T. Osipov, B. Murphy, *et al.*, Phys. Rev. Lett. **109**, 263001 (2012).

[74] E. Goulielmakis, Z.-H. Loh, A. Wirth, *et al.*, Nature **466**, 739 (2010).

[75] D. Marx, M. E. Tuckerman, J. Hutter, and M. Parrinello, Nature **397**, 601 (1999).

[76] W. Kulig and N. Agmon, Nature Chem. **5**, 29 (2013).

[77] Z. Li, M. E. Madjet, O. Vendrell, and R. Santra, Phys. Rev. Lett. **110**, 038302 (2013).

[78] S. Hammes-Schiffer and J. C. Tully, J. Chem. Phys. **101**, 4657 (1994).

[79] V. Veryazov, P.-O. Widmark, L. Serrano-Andres, R. Lindh, and B. Roos, Int. J. Quantum Chem. **100**, 626 (2004).

[80] S.-Y. Lee, W. T. Pollard, and R. A. Mathies, Chem. Phys. Lett. **163**, 11 (1989).

[81] R. Sankari, M. Ehara, H. Nakatsuji, *et al.*, Chem. Phys. Lett. **380**, 647 (2003).

[82] M. F. Kling, C. Siedschlag, A. J. Verhoef, *et al.*, Science **312**, 246 (2006).

[83] G. Sansone, F. Kelkensberg, J. F. Perez-Torres, *et al.*, Nature **465**, 763 (2010).

[84] M. P. Hodges and D. J. Wales, Chem. Phys. Lett. **324**, 279 (2000).

[85] G. Hulthe, G. Stenhagen, Wennerström, and C.-H. Ottosson, J. Chromatogr. **A777**, 155 (1997).

[86] M. Miyazaki, F. A., T. Ebata, and N. Mikami, Science **304**, 1134 (2004).

[87] J.-W. Shin, N. I. Hammer, E. G. Diken, *et al.*, Science **304**, 1137 (2004).

[88] T. Zwier, Science **304**, 1119 (2004).

[89] K. Johnson, M. Price-Gallagher, O. Mamer, *et al.*, Phys. Lett. A **372**, 6037 (2008).

[90] A. Khan, Chem. Phys. Lett. **319**, 440 (2000).

[91] S. S. Iyengar, M. K. Petersen, T. J. F. Day, C. J. Burnham, V. E. Teige, and G. A. Voth, J. Chem. Phys. **123**, 084309 (2005).

[92] C. Lin, H. Chang, J. Jiang, J. Kuo, and M. Klein, J. Chem. Phys **122**, 074315 (2005).

[93] L. J. P. Ament, M. van Veenendaal, T. P. Devereaux, J. P. Hill, and J. van den Brink, Rev. Mod. Phys. **83**, 705 (2011).

[94] F. Hennies, A. Pietzsch, M. Berglund, *et al.*, Phys. Rev. Lett. **104**, 193002 (2010).

[95] A. Pietzsch, Y.-P. Sun, F. Hennies, *et al.*, Phys. Rev. Lett. **106**, 153004 (2011).

Chapter 4

Pump-Probe Study of Quantum Beating of Coherent Electron Hole

So far I have discussed the valence electron hole dynamics in the molecules photoionized by the XUV laser pulses, without assuming quantum coherence between electronic states in the process. The reason lies in the fact that in general case the coherence of the initial wave packet can be rapidly lost, because the wave packet components subject to different electronic potential energy surfaces usually experience contrasting local geometries (and therefore very different forces), the relative motion between wave packet components should result in dephasing from their superposition state. With ultrashort laser pulses, which usually possess spectral width of $\sim$ 1–10 eV, one could indeed initiate the dynamics from a coherent superposition of electronic states, since the energy spacing between electronic states lies in the range from several hundred meV to several eV in the molecules. However, it can be expected that their superposition would be quickly destroyed, resulting in fast dephasing after photoionization. Nontheless, in certain cases, the coherence in the ion core left by photoionization can indeed last long enough, that one can monitor the time evolution of electronic coherence in the ion core with time resolved spectroscopic techniques [1]. For example, in the case if the local geometry of several electron potential energy surfaces resembles each other, and provided there are few states perturbing the coherent superposition state in the way of bath-system coupling, the coherence could be maintained for relatively long time.

Here I present a collaborative effort with experimental group at the University of Arizona to study dynamics of a long lasting coherent electron hole produced by XUV photoionization. We show that the coherence of the created electron hole can be maintained for $\sim$ 1 picosecond and be recorded by XUV pump-IR probe technique.

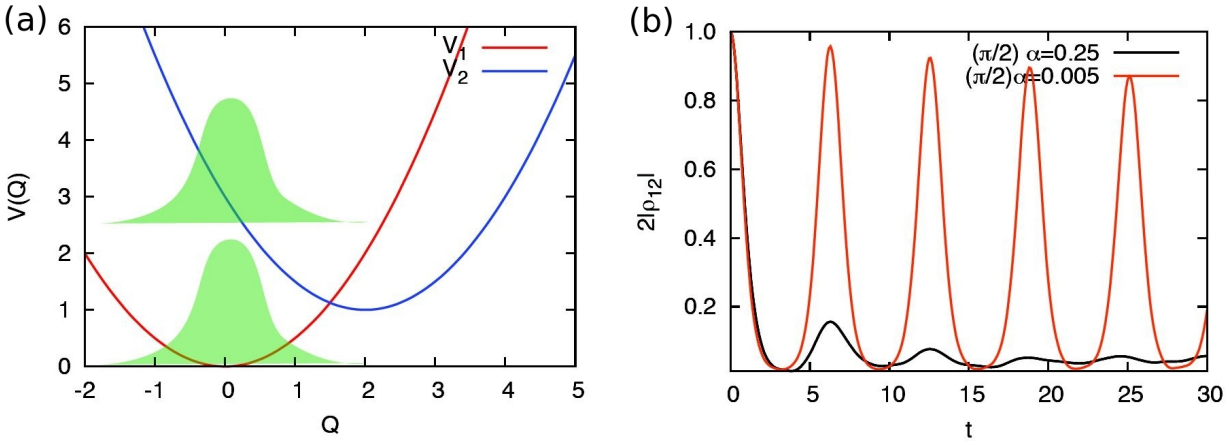

Figure 4.1: Electron decoherence induced by nuclear motion. (a). V_1 and V_2 correspond to two electronic potential energy curves of electronic state $|1\rangle$ and $|2\rangle$, a wave packet centered at $Q = 0$, which contains equally weighted components on both electronic states, is initiated at time $t = 0$. (b). The time evolution of coherence degree measured by off diagonal elements of electronic density matrix, subject to two system bath coupling strength.

4.1 Electronic coherence

Because the ultrashort ionization pulses normally have spectral width of several eV, larger than typical electronic state spacing in the molecule, the created molecular ion should in principle land initially on a coherent superposition state associated with several electronic eigenstates. However, the electronic coherence can decay rapidly, unless the local geometry of electronic potential energy surfaces are similar to each other in the Franck-Condon region, i.e. the region of nuclear geometry subject to vertical ionization, which lies in the vicinity of ground electronic state nuclear geometry.

In general, one should expect the spatial separation of nuclear wave packet components subject to different electronic states can induce rapid dephasing from a superposition of electronic states. Here one can illustrate the concept of electronic coherence loss caused by nuclear wave packet dephasing with a simple system-bath model. In a general context, the $(Q, q_1, \cdots, q_N)$ coordinates could represent vibrational and rotational degrees of freedom of molecules, as well as electronic degrees of freedom beyond the subspace of electronic states in which the investigated coherent superposition actually lives [2].

We will discuss later in this chapter the loss of electronic coherence caused by rotational motion of a photoionized molecule.

Consider a two-state model Hamiltonian with system-bath interaction,

$$\begin{aligned} H(Q, q_1, \cdots, q_N) &= \frac{\omega_s}{2}(P^2 + Q^2) \otimes \mathbf{1} + (\gamma Q + \delta) \otimes |2\rangle \langle 2| \\ &+ \frac{1}{2}\left[\sum_i^N \omega_i p_i + \omega_i \left(q_i - \frac{\lambda_i}{\omega_i} Q\right)^2\right] \otimes \mathbf{1}\,, \end{aligned} \tag{4.1}$$

where $|1\rangle$ and $|2\rangle$ represent the electronic states of the system, P and Q are the momentum and position operators subject to nuclear motion, $\{p_i, q_i\}$ are the canonical coordinates for the bath degrees of freedom. The nuclear degrees of freedom of the system are coupled to an ohmic bath with a spectral density

$$J(\omega) = \frac{\pi}{2}\alpha\omega\theta(\omega - \omega_c)\,, \tag{4.2}$$

and can be discretized as

$$J(\omega) = \frac{\pi}{2}\sum_i^N \frac{\lambda_i^2}{\sqrt{\omega_i}}\delta(\omega - \omega_i)\,. \tag{4.3}$$

Since the wave function of the two-state model can be expressed as

$$\Psi(t=0) = \sum_{i=1}^{2} \chi_i(Q, q_1, \cdots, q_N)\,|i\rangle\,, \tag{4.4}$$

the degree of electronic coherence can be characterized by the off-diagonal element ρ_{ij} of the reduced electronic density matrix, which is defined as

$$\begin{aligned} \rho_{ij} &= \int dQ dq_1 \cdots dq_N\; |i\rangle \langle i|\, \Psi^* \Psi\, |j\rangle \langle j| \\ &= |i\rangle \langle \chi_i | \chi_j \rangle \langle j|\,. \end{aligned} \tag{4.5}$$

As shown in Fig. 4.1(a), a nuclear wave packet centered at $Q = 0$, which contains equally weighted components on both electronic states i.e. $|\chi_1\rangle = |\chi_2\rangle = \frac{1}{\sqrt{2}}|\chi\rangle$, is initiated at time $t = 0$, such as

$$\Psi(t=0) = \frac{1}{\sqrt{2}}\chi(Q, q_1, \cdots, q_N)(|1\rangle + |2\rangle)\,. \tag{4.6}$$

The wave packet component on the lower energy electronic state $|1\rangle$, denoted as $\chi_1(t)$, would mostly sit on the potential minimum of V_1 at $Q = 0$, while the wave packet component at higher energy electronic state $|2\rangle$, denoted as $\chi_2(t)$, would oscillate around the potential minimum of V_2 at $Q = 2$. In the case if the system bath coupling is strong, i.e. α coefficient of the spectral density $J(\omega)$ in Eq. 4.2 is large, the wave packet component

$\Psi_2(t)$ should dissipate fast kinetic energy to the bath, and tends to be localized at the potential well around $Q = 2$, where it could hardly oscillate.

The localization of χ_2 implies its spatial separation with χ_1, which can indeed induce electronic decoherence from the initial superposition state $\frac{1}{2}(|1\rangle+|2\rangle)$. From Fig. 4.1(b), one could readily observe the nuclear motion induced electronic decoherence. As the system-bath coupling strength $(\pi/2)\alpha$ rises, the coherence degree is substantially suppressed. As χ_2 is spatially localized, it manifests itself as fast decay of coherence degree.

4.2 XUV pump IR probe study

Ultrafast extreme ultraviolet (XUV) pump infrared (IR) probe spectroscopy was employed to directly time-resolve the evolution of a valence electron hole wavepacket near a conical intersection in a polyatomic molecule. The coherent motion of this electron hole is observed to persist for $\sim$ 1 picosecond.

As illustrated in previous sections of chapter 3, a conical intersection arises when distinct electronic states become degenerate at a certain set of interatomic coordinates, leading to the breakdown of the conventional Born-Oppenheimer approximation that serves as the basis for the interpretation of many molecular phenomena. Near this point of degeneracy, the electronic and vibrational degrees of freedom become strongly coupled, producing non-adiabatic, vibronic effects [3] which serve to mediate charge transfer processes.

Owing to its small size and known structure, the CO_2 molecule forms an excellent choice for studying these non-adiabatic dynamics. The valence ionized states $A^2\Pi_u(1\pi_u)^{-1}$ (17.3 eV) and $B^2\Sigma_u^+(3\sigma_u)^{-1}$ (18.1 eV)[4] form a conical intersection for nuclear coordinates close to the neutral ground-state equilibrium geometry. These states couple through the joint effect of the bending and the asymmetric stretching motions of the C-O bonds, which is the well-known case of bilinear vibronic coupling [5]. To study the non-adiabatic electron hole dynamics associated with these coupled states, we use the pump-probe scheme illustrated in Fig. 4.2. A femtosecod XUV pulse prepares a σ_u hole wavepacket near this conical intersection whose evolution is then monitored with a time-delayed, near-infrared (NIR) pulse. The role of the NIR pulse is to project the $B^2\Sigma_u^+$ state population onto a dissociation pathway, creating CO^+ ions that form the basis of our measurement.

In the experiment, a 2.4 mJ near-infrared (NIR) pulse with a temporal width of 45 fs is used. As shown in Fig. 4.3, a portion of the pulse is focused into a hollow-core waveguide filled with Xenon gas to generate extreme-ultraviolet (XUV) femtosecond pulses consisting of the 11^{th} to 17^{th} harmonic. The high harmonic spectrum is tuned such that

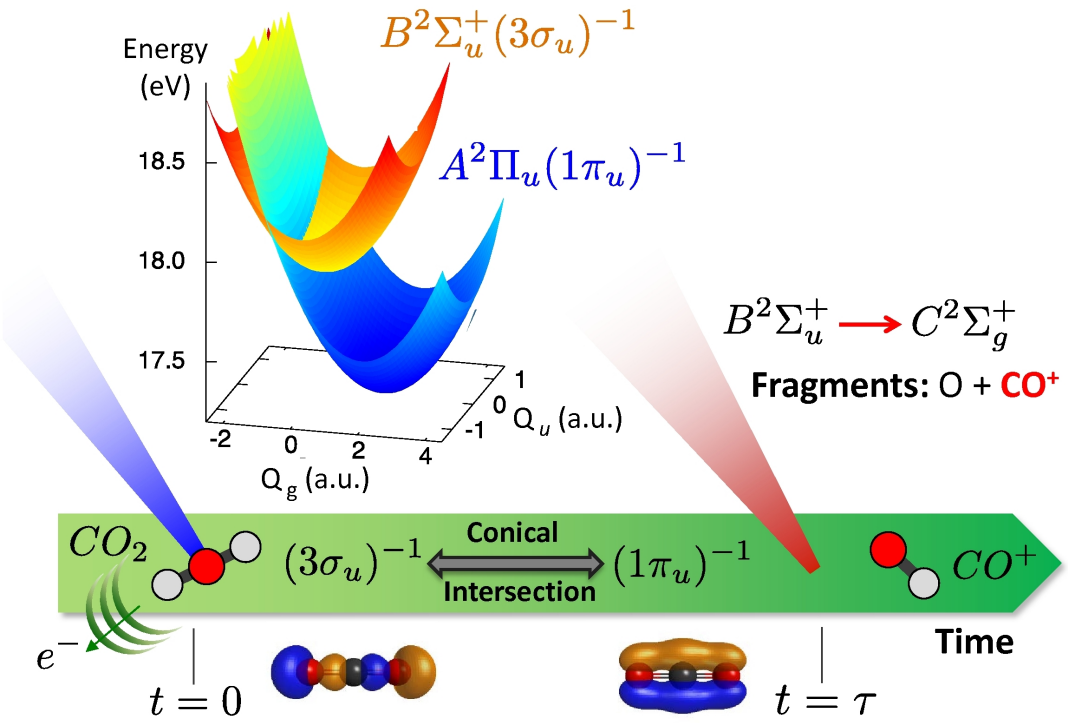

Figure 4.2: The femtosecond XUV pulse photoionizes CO_2 to the $B^2\Sigma_u^+(3\sigma_u)^{-1}$ ionic state. The σ_u hole wavepacket associated with this state exhibits electron hole density distributed along the CO_2 bonding axis and represents a non-stationary state of the cation. Vibronic interactions near the conical intersection result in the periodic transfer of its population to the $A^2\Pi_u(1\pi_u)^{-1}$ ionic state where electron hole density is distributed around the bonding axis (π_u hole). The potential energy surfaces of the $B^2\Sigma_u^+(3\sigma_u)^{-1}$ and $A^2\Pi_u(1\pi_u)^{-1}$ states are shown as a function of the symmetric C-O stretch, Q_g, and asymmetric C-O stretch, Q_u, coordinates. Q_g defines the location of the conical intersection, whereas displacement along Q_u and the bending coordinate Q_ρ mix the two electronic state characters. We resolve the hole dynamics with a time-delayed NIR pulse that excites the $B^2\Sigma_u^+$ population to the predissociative $C^2\Sigma_g^+$ state (19.4 eV) resulting in the formation of observable CO^+ ions.

the 11^{th} harmonic is slightly above the $B^2\Sigma_u^+$ ionic state threshold (18.076 eV [6]). The XUV pulse is focused using a toroidal mirror into an effusive gas jet of CO_2 molecules, where it coherently excites electronic states and launches a non-stationary wavepacket. All harmonics in the XUV spectrum contribute to the excitation of $B^2\Sigma_u^+$ state in a proportion determined by the cross section shown in Fig. 4.3 (b).

The remaining NIR pulse is sent along a time-delayed probing pathway with both polarization and intensity control. We use a probe intensity of ~ 3 TW/cm^2. The NIR

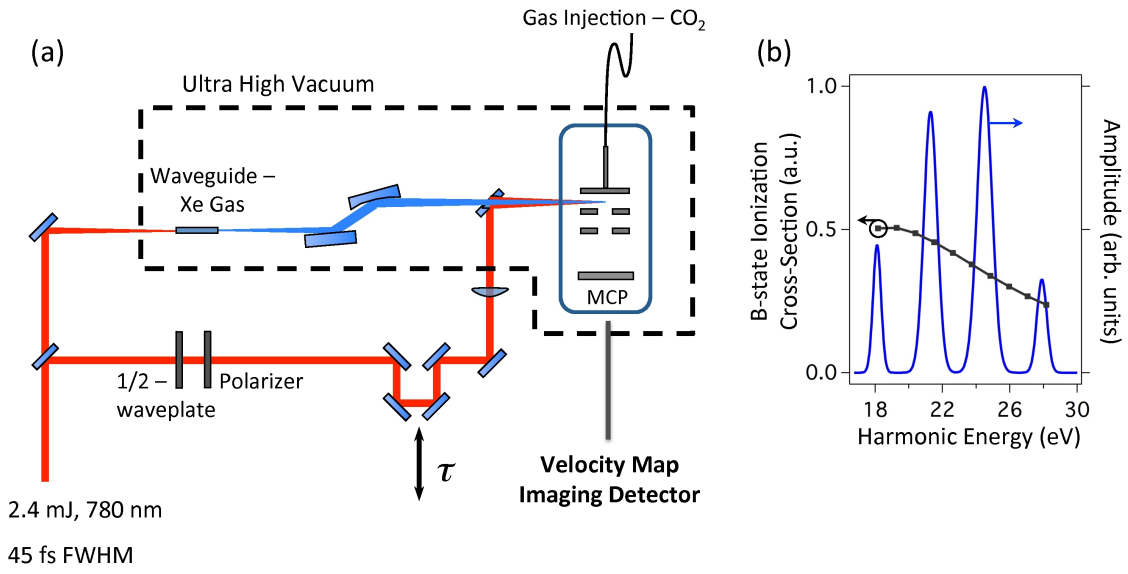

Figure 4.3: The experimental schematic for XUV-pump, NIR-probe set up. The high harmonic spectrum superposed with the $B^2\Sigma_u^+$ state excitation cross-section.

probe pulse maps the $B^2\Sigma_u^+$ state population to the the predissociative $C^2\Sigma_g^+$ state, thus generating an observable CO^+ signal. The dissociation limit for CO^+ ions is 19.4687 eV [7]. Therefore, only states above 17.89 eV can be probed in a one photon transition ($\hbar\omega_{NIR} = 1.58$ eV) to $C^2\Sigma_g^+$ state. A few higher vibrational levels of $A^2\Pi_u$ state also lie in this energy range, however their excitation probability is very low compared to the $B^2\Sigma_u^+$ state [4, 6]. As we discuss later, the dipole excitation also favors the $B^2\Sigma_u^+$ state transition by a few orders of magnitude. Finally, the counts from the direct XUV excitation and dissociation of $C^2\Sigma_g^+$ state form a constant dc baseline, which is subtracted from our time-dependent data.

We finally use a velocity map imaging (VMI) detector to measure the near zero kinetic energy CO^+ ions as a function of pump-probe time delay. The time-zero of the pump-probe scan is calibrated to an accuracy of ± 2 fs using a XUV+IR cross-correlation measurement of Helium photoionization.

Fig. 4.4 (a) shows the experimental measurements of the CO^+ ion yield obtained as a function of time delay between the XUV-pump and NIR-probe pulses. We recorded the ion yield for NIR polarizations both parallel and perpendicular to the XUV polarization.

4.3 Vibronic quantum beating

The most interesting and striking feature in the CO^+ delay-dependent data is the coherent oscillation which exhibits a period of 115 fs. To unveil the nature of the 115 fs oscillation, we consider the bilinear vibronic coupling Hamiltonian proposed in Ref. [5], which is

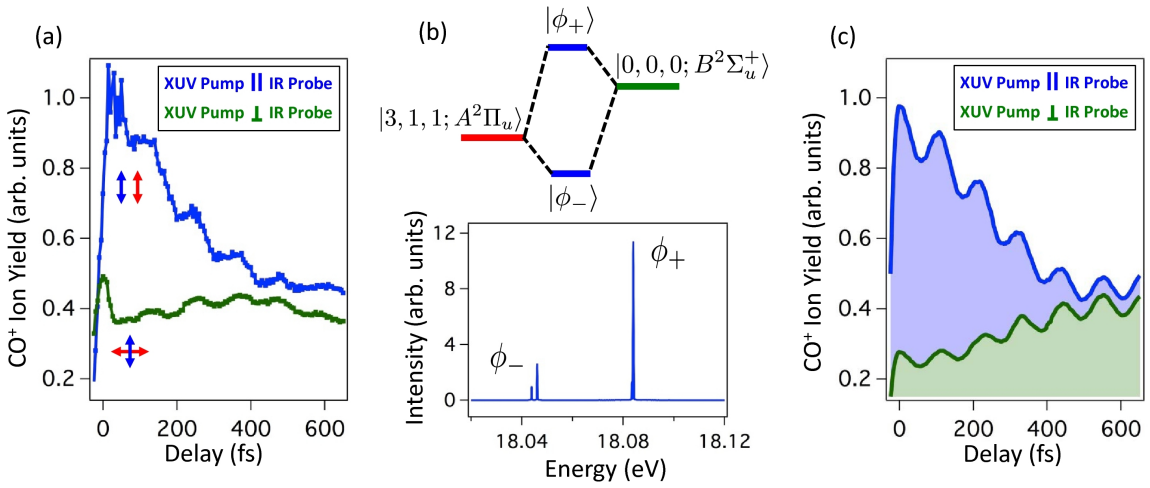

Figure 4.4: (a) Experimental traces of the CO^+ ion yield as a function of XUV-pump, NIR-probe time delay for both parallel (blue) and perpendicular (green) NIR polarizations relative to the XUV field. Oscillations in CO^+ ion yield are due to the coherent excitation of different cationic eigenstates with mixed $\sigma - \pi$ character. (b) Eigenstates of the ion accessible by the XUV pulse. The line height is proportional to $|\langle 0,0,0;X^1|X^1\rangle\langle B^2\Sigma_u^+|\phi_j\rangle|^2$, where $|X^1\rangle$ denotes the neutral ground electronic state, $|\phi_j\rangle$ are eigenstates of the vibronic Hamiltonian of the cation and the sudden approximation for ionization is used. The ϕ_+ and ϕ_- eigenstates are mostly a superposition of vibronic states $|0,0,0;B^2\Sigma_u^+\rangle$ and $|3,1,1;A^2\Pi_u\rangle$, respectively. The small peak close to ϕ_- is assigned to $|2,3,1;A^2\Pi_u\rangle$ and does not contribute to the observed signal. In our notation for vibronic state, e.g. $|n_g,n_\rho,n_u;A^2\Pi_u\rangle$, the quantum numbers n_g, n_ρ, and n_u correspond to the vibrational excitations in C-O symmetric stretch, O-C-O bending and C-O asymmetric stretch modes. (c) Theoretical CO^+ ion traces for both parallel and perpendicular probing fields corresponding to Eq. 4.16. Calculations are based on a quantum treatment of the vibronic dynamics and a classical description of the rotational degrees of freedom. The difference between the parallel and perpendicular ion traces reflects the role of XUV ionization-induced alignment. The CO^+ ion yield for parallel polarization is a direct reflection of the σ_u hole dynamics near the conical intersection and the rapid decay in ion yield is due to the loss of alignment in the thermal ensemble.

expanded in the basis set $|n_g, n_\rho, n_u; B^2\Sigma_u^+\rangle$ and $|n_g, n_\rho, n_u; A^2\Pi_u\rangle$. In this formalism, (n_g, n_ρ, n_u) correspond to the quantum numbers for the excitation of the symmetric stretch, bending, and asymmetric stretch vibrational modes. These modes are characterized by the coordinates Q_g, Q_ρ, and Q_u respectively. The off-diagonal matrix element which results in the mixing of the two electronic states in this Hamiltonian is $V_{AB} \propto \langle\chi_A|Q_\rho Q_u|\chi_B\rangle$. In the vibronic coupling model, the coupling induced by the conical intersection manifests as off-diagonal matrix elements of the Hamiltonian, resulting in the mixing of vibronic states. Using symmetry considerations and a multi-configurational time-dependent Hartree (MCTDH) numerical approach [8], we solve the vibronic coupling model, the calculation results are shown in Fig. 4.5 (a). By taking a Fourier transform of the temporally varying $B^2\Sigma_u^+$ state population, we can obtain the quantum beating spectrum shown in Fig. 4.5 (b). The peaks here correspond to the energy separation between pairs of vibronically coupled states. We identify two vibronic states $|\chi_B\rangle = |0, 0, 0; B^2\Sigma_u^+\rangle$ and $|\chi_A\rangle = |3, 1, 1; A^2\Pi_u\rangle$ as the vibronic states that exhibit the strongest coupling and dominate the wavepacket dynamics.

The two vibronic states $|\chi_B\rangle = |0, 0, 0; B^2\Sigma_u^+\rangle$ and $|\chi_A\rangle = |3, 1, 1; A^2\Pi_u\rangle$ are non-stationary states of the vibronic Hamiltonian, however, one can define the stationary eigenstates $|\phi_\pm\rangle$ by a representation transformation

$$\begin{pmatrix} |\phi_+\rangle \\ |\phi_-\rangle \end{pmatrix} = \begin{pmatrix} \cos\theta & \sin\theta \\ -\sin\theta & \cos\theta \end{pmatrix} \begin{pmatrix} |\chi_B\rangle \\ |\chi_A\rangle \end{pmatrix}, \tag{4.7}$$

where the θ is the mixing angle which quantifies the strength of coupling between the two vibronic states. The hybridization diagram corresponding to this situation is shown in Fig. 4.4 (b). During the photoionization, the XUV pulse used in the experiment predominately populates the $B^2\Sigma_u^+$ electronic state [6], which corresponds to the formation of a σ_u hole. The ionization is accompanied with production of a significantly weaker overtone at $(0, 2, 0)B^2\Sigma_u^+$ [6]. This initial state represents a coherent superposition of cationic eigenstates, $|\phi_\pm\rangle$, whose relative populations are shown in Fig. 4.4 (b). Using the known amplitudes $a_\pm$ and energies $E_\pm$ for $|\phi_\pm\rangle$,

Since the Hamiltonian is composed of an off-diagonal perturbation, $|\chi_{A,B}\rangle$ is not a convenient basis to model the time dynamics of this system. Considering this two-state system, we can define a mixing angle representing the strength of coupling between the vibronic states as

$$\tan(2\theta) = \frac{2V_{AB}}{E_B - E_A}, \tag{4.8}$$

where $E_{A,B}$ are the energies corresponding to the $|\chi_{A,B}\rangle$ vibronic states. With this definition, we can preform a transformation into the stationary eigenstate basis $|\phi_\pm\rangle$ as Eq. 4.7.

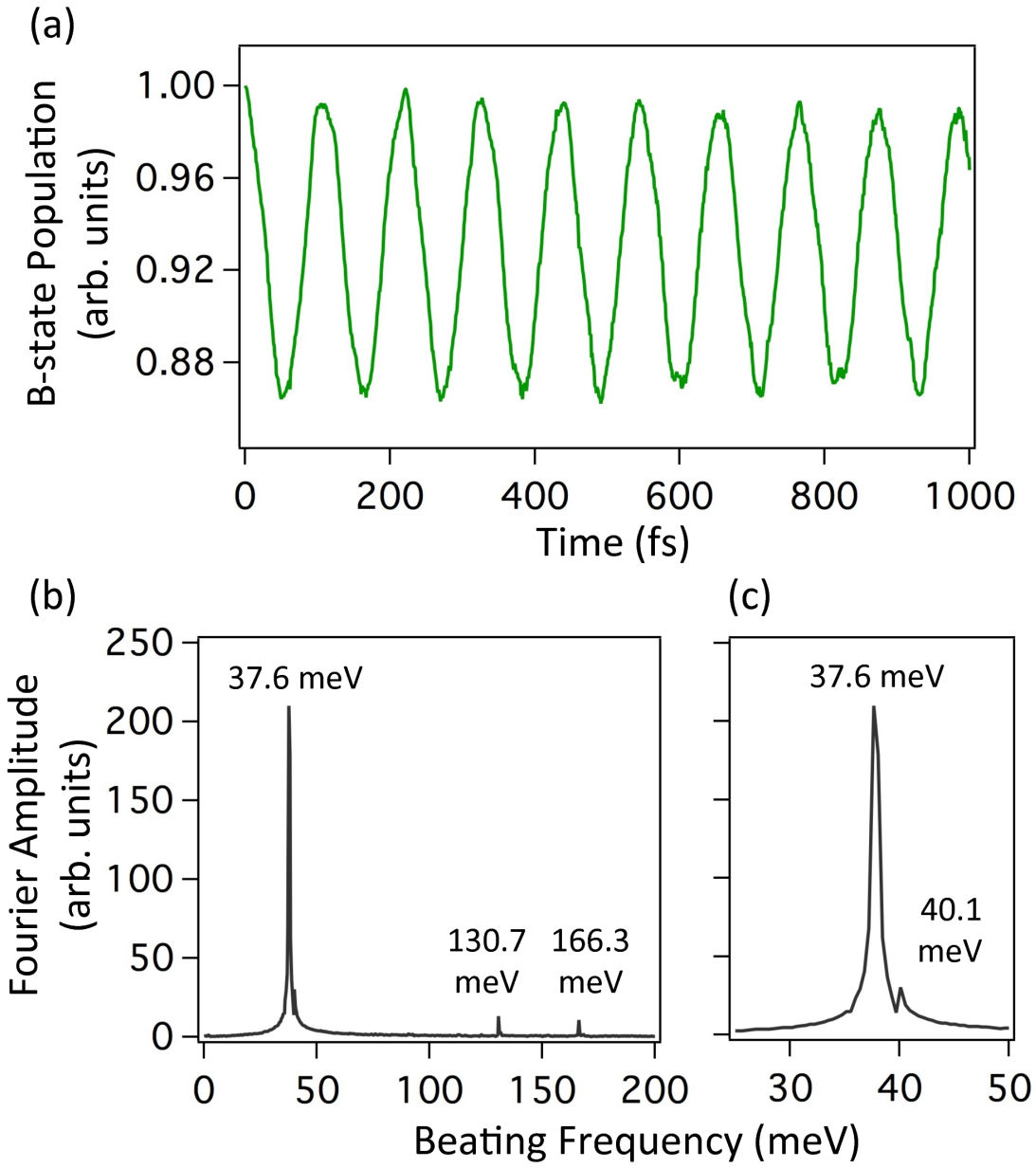

Figure 4.5: (a) Temporal evolution of the $B^2\Sigma_u^+$ state population found by using MCTDH numerical calculations. (b) We obtain the quantum beat spectrum by taking a Fourier transform of (a) to determine the vibronic state pairs at play in the time dynamics. The most prominent peak at 37.6 meV corresponds to the energy difference of the $|\phi_\pm\rangle$ states, which can be represented by the coupled vibronic states $|0,0,0;B^2\Sigma_u^+\rangle$ and $|3,1,1;A^2\Pi_u\rangle$. However, weaker peaks are observed at 40.1 meV, 130.7 meV, and 166.3 meV. (c) A magnified plot of the energy range encompassing the 37.6 meV beating peak.

Thus, in the experiment, our XUV pulse prepares a coherent superposition of the two eigenstates of the vibronic Hamiltonian resulting in the time-dependent wavefunction

$$|\Psi(t)\rangle = a_+ e^{-iE_+ t} |\phi_+\rangle + a_- e^{-iE_- t} |\phi_-\rangle . \tag{4.9}$$

where $a_\pm$ are the initial excitation amplitudes into the two eigenstates with eigenenergies $E_\pm$. We can expand this wavefunction in the $|\chi_{A,B}\rangle$ basis as

$$\begin{aligned} |\Psi(t)\rangle &= (\sin\theta\cos\theta e^{-iE_+ t} - \sin\theta\cos\theta e^{-iE_- t}) |\chi_A\rangle \\ &+ (\sin^2\theta e^{-iE_+ t} + \cos^2\theta e^{-iE_- t}) |\chi_B\rangle , \end{aligned} \tag{4.10}$$

where the amplitude coefficients $a_\pm$ were derived using the initial conditions $c_A(0) \equiv \langle\chi_A | \Psi(0)\rangle = 0$ and $c_B(0) \equiv \langle\chi_B | \Psi(0)\rangle = 1$. By calculating the projection of $|\phi_\pm\rangle$ onto the basis $|\phi_{A,B}\rangle$, we can numerically estimate the mixing angle to be $\theta = 0.195$.

Because the decay of baseline of CO^+ as observed in experiment (Fig. 4.4a) is missing in the MCTDH simulation (Fig. 4.5(a)), in which only vibrational and electronic degrees of freedom were taken into account, one may need to consider the effect of molecular rotation, which is the cause of the baseline decay as well as for the decay of quantum beating oscillation, as explained in the following.

Given that all CO_2^+ cations excited to $C^2\Sigma_g^+$ state will eventually dissociate to give a CO^+ ion signal, we can assume that the population in the predissociative $C^2\Sigma_g^+$ state is proportional to the intensity of the CO^+ ion yield. Therefore, we can write the intensity of the CO^+ ion yield as

$$I(CO^+; t) \propto \left| \left(\mathscr{E}(t)\vec{\epsilon}_{\mathrm{IR}} \cdot \mathbf{R}_{\mathrm{LM}} \left\langle C^2\Sigma_g^+ \left| \hat{\vec{d}}_{\mathrm{M}} \right| \Psi(t) \right\rangle \right) \right|^2 , \tag{4.11}$$

where $|\Psi(t)\rangle$ is the time-dependent wavefunction of the ionized system in the molecular frame (Eq. 4.10), $\hat{\vec{d}}_{\mathrm{M}}$ is the dipole operator in the molecular frame, the NIR probing field is characterized by its polarization vector in the laboratory frame $\vec{\epsilon}_{\mathrm{IR}}$ and a temporal profile $\mathscr{E}(t)$, and $\mathbf{R}_{\mathrm{LM}}$ is the molecular to laboratory frame rotation matrix. The z–axis of the lab system is set parallel to the polarization direction of the linearly polarized XUV pulse. In order to make the notation more compact we define$D_A^{\kappa'} \equiv \left\langle C^2\Sigma_g^+ \left| \hat{d}_{\mathrm{M}}^{\kappa'} \right| A^2\Pi_u \right\rangle$ and $D_B^{\kappa'} \equiv \left\langle C^2\Sigma_g^+ \left| \hat{d}_{\mathrm{M}}^{\kappa'} \right| B^2\Sigma_u^+ \right\rangle$, where κ' is one of the body-fixed axes $\{x', y', z'\}$. We can now write the corresponding lab frame components of the dipole matrix elements

$$\begin{aligned} \begin{pmatrix} D_X^x \\ D_X^y \\ D_X^z \end{pmatrix} &= \mathbf{R}_{\mathrm{LM}} \begin{pmatrix} D_X^{x'} \\ D_X^{y'} \\ D_X^{z'} \end{pmatrix} \\ &= \begin{pmatrix} \cos\alpha\cos\beta & \sin\alpha & \cos\alpha\sin\beta \\ -\sin\alpha\cos\beta & \cos\alpha & -\sin\alpha\sin\beta \\ -\sin\beta & 0 & \cos\beta \end{pmatrix} \begin{pmatrix} D_X^{x'} \\ D_X^{y'} \\ D_X^{z'} \end{pmatrix} \end{aligned} \tag{4.12}$$

where $X = \{A, B\}$, β is the polar angle of the CO_2^+ system with respect to the z–axis in the laboratory frame and α is the azimuthal angle of CO_2^+ in the x, y plane. We calculated the dipole matrix elements $D_A^{x',y'}$ and $D_B^{z'}$ corresponding to processes $A^2\Pi_u \xrightarrow{xy} C^2\Sigma_g^+$ and $B^2\Sigma_u^+ \xrightarrow{z} C^2\Sigma_g^+$ *ab initio* and found that $D_A^{x'}/D_B^{z'} \simeq 0.02$ at the Franck-Condon geometry. All other matrix elements involving these pairs of states are zero by symmetry. Hence, from now on we consider that only $B^2\Sigma_u^+ \xrightarrow{z} C^2\Sigma_g^+$ is relevant for the probing step. For the case that the probe pulse is aligned along the z–axis, $\vec{\epsilon}_{\mathrm{IR}} = (0, 0, 1)$, Eq. 4.11 results in

$$I(CO^+, t) \quad \propto \quad D_B^{z'^2} \cos^2\beta \left[\cos^4\theta + \sin^4\theta + \frac{1}{2}\sin^2 2\theta \cos(E_+ - E_-)t\right] \tag{4.13}$$

where the term in square brackets corresponds to $|c_B(t)|^2$. A similar expression is found for probing in the x direction of the lab frame

$$I(CO^+, t) \quad \propto \quad D_B^{z'^2} \sin^2\beta \cos^2\alpha \left[\cos^4\theta + \sin^4\theta + \frac{1}{2}\sin^2 2\theta \cos(E_+ - E_-)t\right]. \tag{4.14}$$

Eqs. 4.13 and 4.14 explain the origin of the oscillatory ion-yield observed in the experimental data and also indicate that the contribution to the signal intensity from one of the molecules in the probed ensemble depends on its spatial orientation. As the wavefunction evolves, the system develops a mixed $\sigma - \pi$ electronic character. We can see from the above equation that the energy separation $E_+ - E_-$ characterizes the timescale of quantum beating between the $|\phi_+\rangle$ and $|\phi_-\rangle$ eigenstates. The numerical results in Fig. 4.4 (b) show an eigenstate energy difference of 37.6 meV, which corresponds to a timescale of 110 fs. This timescale matches very well with the ion yield oscillation observed in experimental results of Fig. 4.4 (a).

From Eq. 4.13, we expect the ion yield to oscillate about some constant baseline. However, in the experimental CO^+ signal, the ion yield quickly decays within 400 fs. The decay of this signal originates from the decrease in the degree of cation alignment (*decay of anisotropy*) due to a finite rotational temperature of the ensemble [9, 10].

The CO_2^+ ions are initially prepared as an ensemble of rigid rotors aligned through photoionization by the XUV pulse. Assuming a dominant s-wave ($l = 0$) photoionization and using total angular momentum conservation, the ionization probability $W(\beta)$ can be written as

$$\begin{aligned} W(\beta) \quad &= \quad C(\omega)\left(\left|D^{z'}(B^2\Sigma_u^+)\right|^2 \cos^2\beta + \left|D^{\{x',y'\}}(A^2\Pi_u)\right|^2 \sin^2\beta\right) \\ &\propto \quad 1 + aP_2(\cos\beta), \quad a \in [-1, 2], \end{aligned} \tag{4.15}$$

where β is the angle between the z–axis in the lab system and the molecular axis, $C(\omega)$ is the XUV energy-dependent spectrum, and $D^{\kappa'}(\chi) = \left\langle \chi; l = 0 \left| \hat{d}_M^{\kappa'} \right| X^1\Sigma_g^+ \right\rangle$ are, as previously, dipole matrix elements in the molecular frame. While the XUV pulse preferentially

prepares molecules in $B^2\Sigma_u^+$ state aligned parallel to the XUV polarization, it also excites molecules to $A^2\Pi_u$ state aligned perpendicular to the XUV polarization. It is well established from synchrotron measurements [6] that the $B^2\Sigma_u^+$ electronic state has a much higher ionization probability than the $A^2\Pi_u$ state at photon energies in our XUV pump pulse. Hence, we expect the contribution from $A^2\Pi_u$ state excitation to the total CO^+ ion yield to be negligible. Given that $\left|D^{\{x',y'\}}(A^2\Pi_u)\right|^2 \ll \left|D^{z'}(B^2\Sigma_u^+)\right|^2$, the initial $\langle\cos^2\beta\rangle$ after XUV excitation will be close to 0.6. Therefore, the XUV ionization creates an aligned distribution of CO_2^+ ions in the $B^2\Sigma_u^+(3\sigma_u)^{-1}$ electronic configuration, which is then probed by the NIR field.

We can now model the observed features in the CO^+ ion yield by accounting for the NIR probing step and the rotational degrees of freedom in the molecular system. Assuming a dominant s-wave nature for photoionization, dipole selection rules dictate that the ionization will preferentially occur from $3\sigma_u$ orbitals for molecules aligned parallel to the XUV field. Therefore, the XUV pulse prepares an aligned distribution of CO_2^+ ions in a $B^2\Sigma_u^+$ electronic configuration. Further, due to the dipole selection rules and bandwidth constraints, the parallel NIR probing field exclusively maps the $B^2\Sigma_u^+$ state population to the predissociating $C^2\Sigma_g^+$ state[7], resulting in the formation of CO^+ ions. This transition is forbidden for a perpendicular probing field, explaining the large discrepancy in ion yield between the parallel and perpendicular polarizations at $t = 0$ fs seen in Fig. 4.4 (a).

To incorporate the effect of ionization induced alignment and the thermal rotational effects into our simulation, we perform a trajectory calculation for the ensemble of rigid rotors. In this approach, we compute the ensemble-averaged NIR transition dipole $D_B(t)$ from the $B^2\Sigma_u^+$ state to the final $C^2\Sigma_g^+$ state. Using the time-dependent wavefunction in Eq. 4.9, and calculating the transition strength to $C^2\Sigma_g^+$ state, the expression for the CO^+ ion yield is given by taking ensemble average of Eq. 4.13, such that

$$I(CO^+, t) \propto D_B^{z'2} \left\langle \cos^2\beta \right\rangle \left[\cos^4\theta + \sin^4\theta + \frac{1}{2}\sin^2 2\theta \cos(E_+ - E_-)t \right] \tag{4.16}$$

The 110 fs quantum beating is therefore reproduced in the experimental CO^+ ion yield. Additionally, the finite rotational temperature T_{rot} of the molecular ensemble leads to the loss of the cation's alignment, resulting in a time dependent $\langle D_B(t)\rangle$. Figure 4.4 (c) shows the result of Eq. 4.16 for a rotational temperature relevant to our experimental conditions ($T_{rot} = 200$ K). The computed signal intensity for parallel NIR polarization undergoes a decay in nearly 400 fs, which matches the experimental observation in Fig. 4.4 (a). This decay can be explained as follows: as the ensemble rotates out of alignment, a smaller fraction of the molecules can be probed by the parallel NIR field. On the other hand, this opens up a larger number of molecules which can be probed by the perpendicular NIR field, resulting in the increase in ion yield for perpendicular polarization.

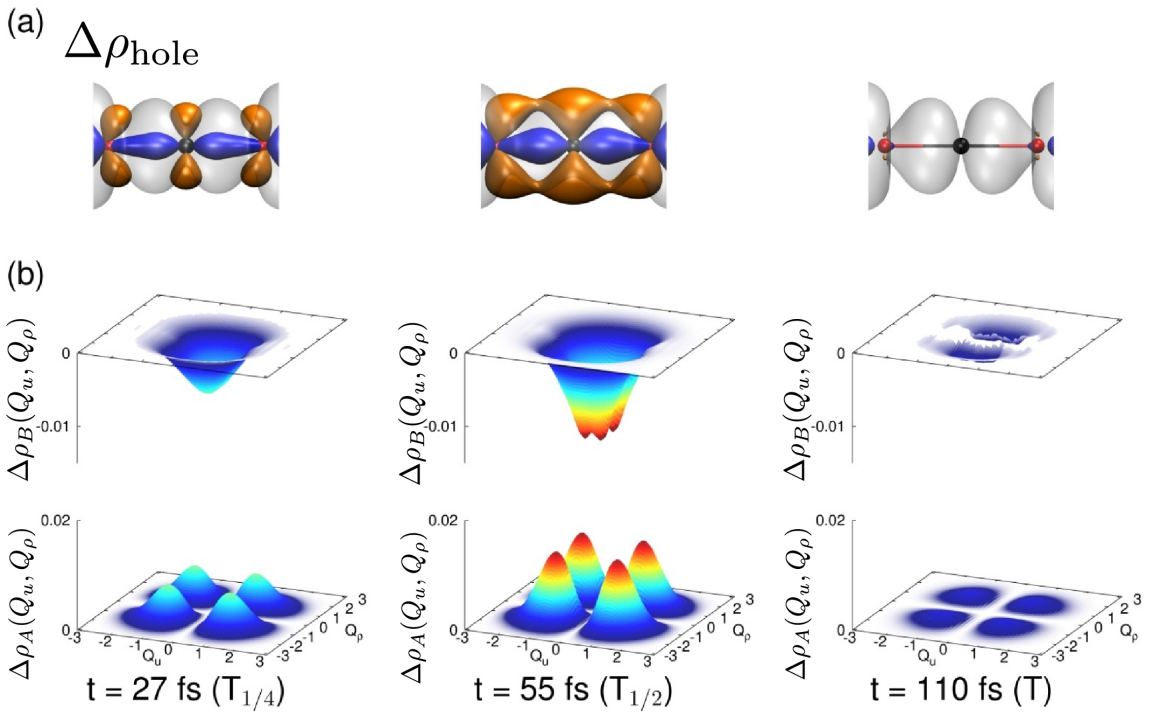

Figure 4.6: (a) Change in electron hole density $\Delta\rho_{\mathrm{hole}}$ with respect to time zero. The dynamics shown correspond to the 110 fs quantum beat. During this period, the electron hole density is driven from σ_u character along the molecular axis (blue, negative) to π_u character (orange, positive) around the molecular axis. (b) Change in the reduced density of the vibronic wavepacket along the coupling coordinates Q_u and Q_ρ (defined in main text) associated with electronic states $B^2\Sigma_u^+$ (upper panel) and $A^2\Pi_u$ (lower panel).

With strong agreement between experiment and theory, we finally arrive at a complete picture of coupled nuclear-hole dynamics near a conical intersection of CO_2^+(Fig. 4.6). The XUV pulse first prepares the molecule in a coherent superposition of cationic eigenstates with an initial σ_u electron hole character. The bending and asymmetric stretch motions of the molecule coherently drive the electron hole density from the region along the molecular axis with σ_u symmetry, to the region around the molecular axis with π_u symmetry. The relative electron hole density corresponding to the evolution of the wavepacket within the first 110 fs period of quantum beating is shown in Fig. 4.6 (a). The reduced density of the nuclear wavepacket on the $A^2\Pi_u$ and $B^2\Sigma_u^+$ states in terms of the asymmetric stretching (Q_u) and bending (Q_ρ) coordinates is shown in Fig. 4.6 (b) and demonstrates periodic modulation in synchronization with the electron hole dynamics.

We can also monitor the evolution of quantum coherence in the cationic superposition

by using the results in Fig. 4.4(a) and defining the time-dependent ion yield contrast as

$$C_{expt}(\tau) = \frac{I_{sig}(\tau) - I_{dc}(\tau)}{I_{dc}(\tau)}, \tag{4.17}$$

where $I_{sig}(\tau)$ is the raw CO^+ ion yield and $I_{dc}(\tau)$ is the non-oscillatory component. In Fig. 4.7 (a), we plot the delay-dependent contrast observed in the experiment. We can compare this to the theoretical ion-yield contrast from Eq. 4.16, or

$$C_{theo}(t) = \frac{\frac{1}{2}\sin^2(2\theta)}{\cos^4\theta + \sin^4\theta}\cos(E_+ - E_-)t. \tag{4.18}$$

Eq. 4.16 does not consider dephasing effects and the *amplitude* of the theoretical contrast depends only on the mixing angle and is stationary with time, whereas the amplitude of the experimental contrast in Fig. 4.7 (a) decays with time delay. This decay in amplitude is indicative of the loss of coherence. In Fig. 4.7 (b), we plot the delay-dependent contrast amplitude for the four prominent oscillation periods observed in the experiment and find that the contrast amplitude decreases linearly with time. By extrapolation, we can extract the initial contrast amplitude at $t = 0$ fs, before the onset of decoherence. Using the initial contrast amplitude value in Eq. 4.18, we can obtain an experimental measurement of the mixing angle, $\theta = 0.183 \pm 0.007$. This can readily be compared with the mixing angle directly obtained from numerical results of MCTDH calculations which yield $\theta = 0.195$. Our work thus represents a sensitive measurement of the coupling induced by the non-adiabatic perturbations near a conical intersection.

From the linear fit in Fig. 4.7(b), we experimentally infer the rate of decoherence to be (0.06 ± 0.01) ps^{-1}. The mechanism behind this can be understood in terms of thermal dephasing. At a finite rotational temperature, XUV excitation from the ground state creates an incoherent distribution of rotational levels in the $|\chi_B\rangle$ vibronic state. Since the rotational constants of coupled $|\chi_B\rangle$ and $|\chi_A\rangle$ states are appreciably different, the energy gap between them varies with the rotational quantum number, J.

The origin of the decay in the oscillation contrast of the CO^+ ion signal can be explained considering the slightly different rotational constant in states $A^2\Pi_u$ and $B^2\Sigma_u^+$ due to different mean equilibrium distances between atoms in each electronic potential energy surface. We evaluate the impact of the rotational dynamics on the decoherence rate based on the model Hamiltonian

$$\hat{\mathcal{H}} = \begin{pmatrix} \omega_A + \hat{\mathcal{H}}_A & \lambda \\ \lambda & \omega_B + \hat{\mathcal{H}}_B \end{pmatrix} \tag{4.19}$$

where $\hat{\mathcal{H}}_X = B_X\hat{\mathcal{J}}^2$, $X = A, B$. In this model each of the vibronic states described previously is incremented by a rotational Hamiltonian characterized by a different rotational

constant. This causes the gap between vibronic states $|\chi_B\rangle = |0,0,0;B^2\Sigma_u^+\rangle$ and $|\chi_A\rangle = |3,1,1;A^2\Pi_u\rangle$ to be dependent on the rotational state of the system. The rotational constants for the two electronic states are $B(A^2\Pi_u) = 0.28$ cm^{-1} and $B(B^2\Sigma_u^+) = 0.38$ cm^{-1}, respectively, which correspond to the equilibrium geometry of the CO_2^+ ion in the $A^2\Pi_u$ and $B^2\Sigma_u^+$ state. T=200 K is assumed for the thermal averaging. In Fig. 4.8 the damping of the quantum beating in the signal leads to a loss of contrast of about 50% in 500 fs, which is consistent with our observation.

As a result, the J- dependent phases of electron hole oscillations diverge with time, manifesting as an loss of coherence in our data. The dashed curve in Fig. 4.7 (a) represents the results of a semi-classical, linear rotor model incorporating the effects of rotational dephasing of a thermal distribution. The numerical contrast decays on a very similar timescale to what is seen in the experiment. This is further exemplified in Fig. 4.7 (b), where the theoretical contrast amplitude (dashed) follows the experimental amplitude (solid). It is interesting to note that while the thermal ensemble is fairly warm ($T_{\text{rot}} \approx 200$ K), the coherence in the weakly coupled cationic states persists for more than 500 fs.

The coupling between $A^2\Pi_u$ and $B^2\Sigma_u^+$ states with the cationic ground state $X^2\Pi_g$ can be excluded from the damping mechanism of quantum beating, by observing the large energy gap of ~ 4 eV between $X^2\Pi_g$ and $A^2\Pi_u$ /$B^2\Sigma_u^+$ states, whereas energy gap between $A^2\Pi_u$ and $B^2\Sigma_u^+$ states is 0.77 eV [11]. Since the non-adiabatic coupling matrix element (NACME) $\vec{D}_{ij}$ is inversely proportional to the energy gap, according to the Hellmann–Feynman theorem in Eq. 2.10 [3],

$$\vec{D}_{ij} = \left\langle \varphi_i \left| \hat{\vec{\nabla}} \right| \varphi_j \right\rangle = \frac{\left\langle \varphi_i \left| \vec{\nabla} \hat{\mathcal{H}}_e \right| \varphi_j \right\rangle}{E_j - E_i}, \tag{4.20}$$

where $|\varphi_i\rangle = |A^2\Pi_u\rangle, |B^2\Sigma_u^+\rangle, |C^2\Sigma_g^+\rangle$. It is obvious that the coupling to the $X^2\Pi_g$ state should be negligible comparing the to $A^2\Pi_u$ –$B^2\Sigma_u^+$ coupling. Fig. 4.9 illustrates the NACMEs between $A^2\Pi_u$, $B^2\Sigma_u^+$ and $X^2\Pi_g$ states from *ab initio* multi-configurational self-consistent field (MCSCF) calculation [12], the $A^2\Pi_u$ –$B^2\Sigma_u^+$ coupling is two orders of magnitude stronger than the $A^2\Pi_u$ /$B^2\Sigma_u^+$ coupling to the $X^2\Pi_g$ state in the vicinity of conical intersection.

The concept of quantum coherence is playing an increasingly important role in our understanding of chemical and biological phenomena[13, 14, 15, 16] and our results suggest that the non-adiabatic coupling to nuclear motion provides an efficient means for mediating coherent charge transfer in polyatomic systems.

In this study, we used an XUV-pump and NIR-probe to resolve the ultrafast and coherent motion of an inner-valence electron hole between σ and π orbitals. The coherent

motion of electron hole was observed to last $\sim$ 1 ps, due to the reason that the potential energy surfaces are of similar geometry at the Franck-Condon region, and the XUV ionization pulses actually produce specific superposition state involving only a small set of vibronic states, which can be approximated as a two-state system.

We quantified the coupling between electronic states due to the perturbation caused by the conical intersection and measured the evolution of quantum coherence during the charge oscillation. The real-time visualization of electron hole dynamics in such non-adiabatic scenario and the understanding of the limitations of the quantum system due to coupling with environmental degrees of freedom is fundamental in probing the inner workings of charge migration processes occurring in nature. The experimental and theoretical results we obtained here for the linear triatomic molecule represent first steps in elucidating these dynamics and paves the way for realization of the full potential of ultrafast XUV spectroscopy in the measurement and control of charge dynamics in complex biochemical systems.

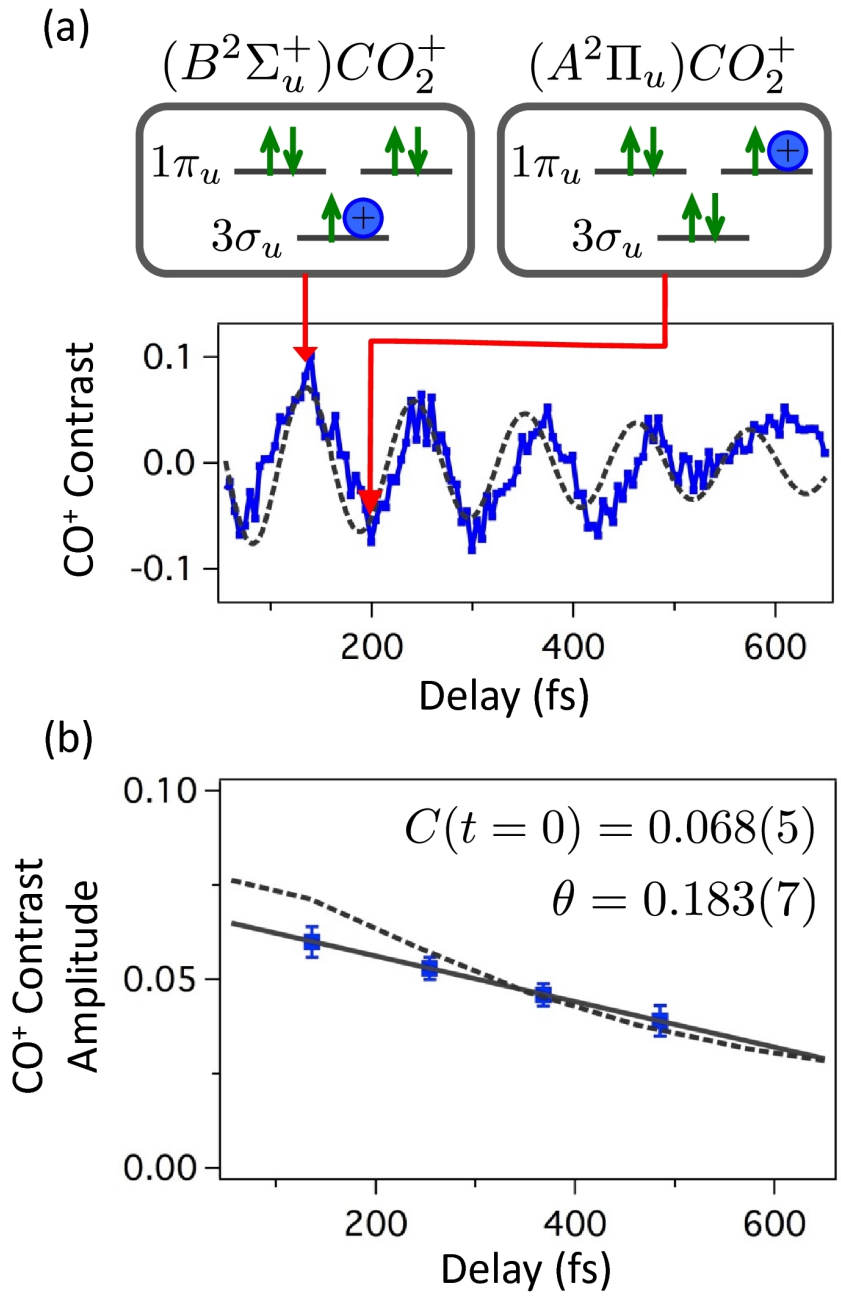

Figure 4.7: (a) The experimental results for the contrast of CO^+ yield oscillation for parallel polarization. The contrast peaks and minima reflect the electronic character of the hole as it evolves in time. The dashed curve is the theoretically calculated contrast incorporating the effects of dephasing due to slightly different rotational constants of the $A^2\Pi_u$ and $B^2\Sigma_u^+$ states and the rotational temperature of the ensemble. (b) The contrast amplitude is plotted for the four prominent oscillation periods shown in (a) and it decays linearly over time due to the loss of coherence. A linear fit to this data allows us to experimentally measure the mixing angle to be $\theta = 0.183(7)$ before the onset of decoherence. The dashed line is the theoretical calculated decay of contrast amplitude.

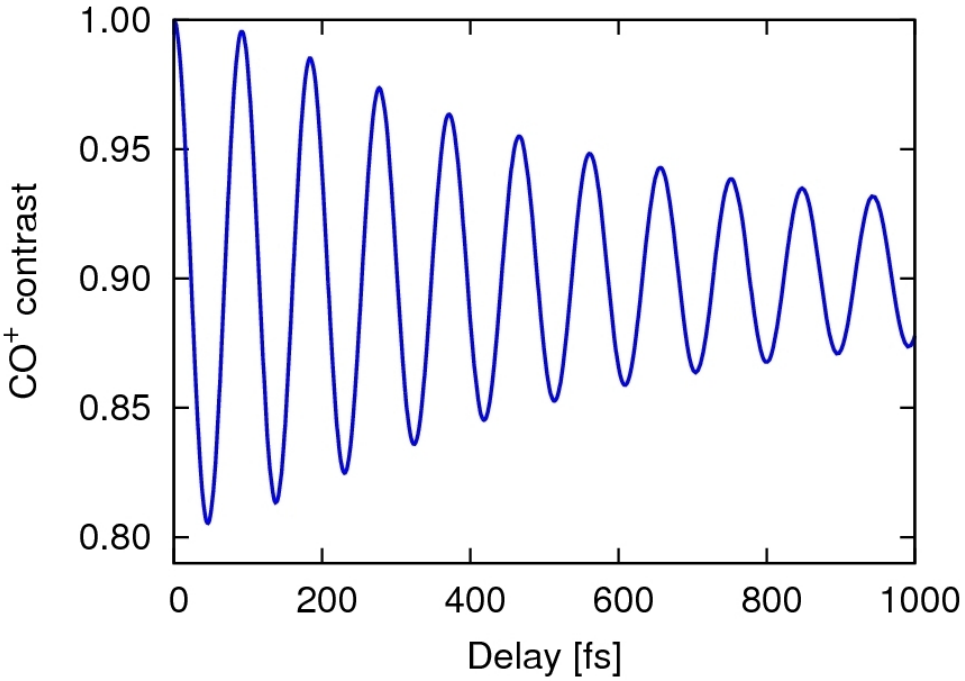

Figure 4.8: The contrast of CO^+ yield oscillation, assuming the difference in the rotational constants of $A^2\Pi_u$ and $B^2\Sigma_u^+$ states to be the only damping mechanism.

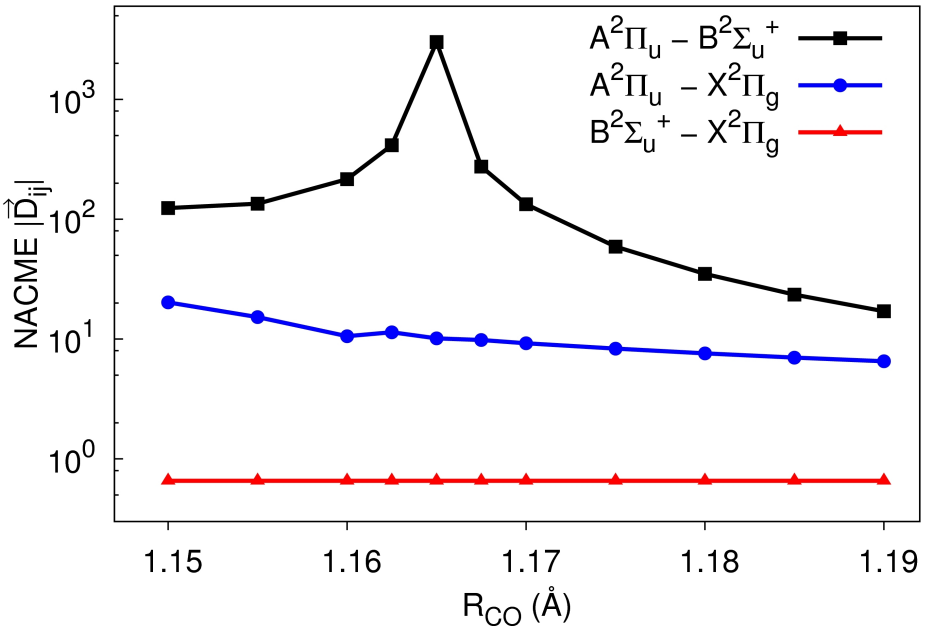

Figure 4.9: The norm of the non-adiabatic coupling matrix element vector $\vec{D}_{ij}$ between $A^2\Pi_u$, $B^2\Sigma_u^+$ and $X^2\Pi_g$ states in the vicinity of conical intersection.

4.4 Bibliography

[1] S. Pabst, L. Greenman, P. J. Ho, D. A. Mazziotti, and R. Santra, Phys. Rev. Lett. **106**, 053002 (2011).

[2] S. Pabst, L. Greenman, P. J. Ho, D. A. Mazziotti, and R. Santra, Phys. Rev. Lett. **106**, 053003 (2011).

[3] G. Worth and L. Cederbaum, Annu. Rev. Phys. Chem. **55**, 127 (2004).

[4] L. Wang, J. Reutt, Y. Lee, and D. Shirley, J. Electron. Spectrosc. Relat. Phenom. **47**, 167 (1988).

[5] T. Zimmermann, H. Köppel, and L. Cederbaum, J. Chem. Phys. **83**, 4697 (1985).

[6] J. Liu, M. Hochlaf, and C. Ng, J. Chem. Phys. **113**, 7988 (2000).

[7] J. Liu, W. Chen, M. Hochlaf, X. Qian, C. Chang, and C. Ng, J. Chem. Phys. **118**, 149 (2003).

[8] M. Beck, A. Jäckle, G. Worth, and H. Meyer, Phys. Rep. **324**, 1 (2000).

[9] Y. Lin, P. Pieniazek, M. Yang, and J. Skinner, J. Chem. Phys. **132**, 174505 (2010).

[10] E. Smith and D. Jones, J. Phys. Chem. A **115**, 4101 (2011).

[11] D. A. Shaw, D. M. P. Holland, M. A. Hayes, M. A. MacDonald, A. Hopkirk, and S. M. McSweeney, Chem. Phys. **198**, 381 (1995).

[12] M. W. Schmidt, K. K. Baldridge, J. A. Boatz, *et al.*, J. Comput. Chem. **14**, 1347 (1993).

[13] N. Lambert, Y.-N. Chen, Y.-C. Cheng, C.-M. Li, G.-Y. Chen, and F. Nori, Nature Phys. **9**, 10 (2013).

[14] G. S. Engel, T. R. Calhoun, E. L. Read, *et al.*, Nature **446**, 782 (2007).

[15] P. Hockett, C. Z. Bisgaard, O. J. Clarkin, and A. Stolow, Nature Phys. **7**, 612 (2011).

[16] C. Z. Bisgaard, O. J. Clarkin, G. Wu, A. M. D. Lee, O. Geßner, C. C. Hayden, and A. Stolow, Science **323**, 1464 (2009).

Chapter 5

Electron Dynamics in Strongly Correlated Materials

Real time DMFT-MCTDH scheme for electron dynamics in strongly correlated materials

I have so far addressed the coupled relaxation dynamics of electrons and nuclei in molecules under irradiation with ultrafast laser pulse that photoionises the molecule. The created valence electron hole feels the Coulomb force from the nuclei and the rest of the electrons, the correlated motion of electrons and nuclei then determines the dynamical behavior and the fate of the molecule after photoionization.

In solids, the correlated motion of electron mediated by strong Coulomb interaction can also lead to dramatic consequence – e.g. highly nontrivial phenomena such as heavy fermion behavior, the Mott metal–insulator transition [1], and the qualitative failure of the energy band theory to explain these experimental observations.

The exotic electron correlation behavior is known to exist in a wide scope of condensed matter dubbed *strongly correlated materials*, which includes the high-T_c superconductors. One of the most peculiar aspects of high-T_c superconductors is that their parent compounds are Mott insulators, which are typical strongly correlated materials, and the superconductivity is achieved by introducing charge carriers into the insulating parent compounds. It is generally believed that a comprehensive understanding of the evolution from Mott insulator to superconductor holds the key to the mystery of high-T_c superconductors. Moreover, in the high-T_c superconductors, strong Coulomb correlation essentially dominates the interaction in the CuO_2 plane and the formation of Zhang–Rice singlets [2] between electron

holes with antiparallel spins ($S = 0$) in Cu $3d$ and O $2p$ orbitals.

The intriguing properties and applications of strongly correlated materials have motivated methodological development beyond the energy band theory. For this purpose, the dynamical mean field theory (DMFT) is one of the state–of–the–art tool developed to solve the electronic structure of strongly correlated solids.

Considering the real time picture in the strongly correlated solids, their electronic nuclear dynamics has been studied using pump probe technique, e.g. the time–resolved optical spectroscopy [3, 4] and the time–resolved photoemission spectroscopy [5]. The experimental spectra and theoretical results acquired using DMFT in these works illustrate striking scenario on how the quasi–particles in solids emerge dynamically on the femtosecond time scale [3, 4], as well as the build–up of electronic correlations after the laser pump [5]. A real time movie of quasi–particle formation near Fermi surface can be recorded by the pump probe spectroscopy [4]. These phenomena in condensed matter revealed by pump–probe spectroscopy can have profound implications to understand the fundamental concepts of many–body physics.

Besides, the solids in nonequilibrium state as they are pumped by laser can exhibit intriguing properties and hidden phases, which are absent in equilibrium. For example, one can induce insulator–metal transition or superconductor phase transition using ultrashort laser pulses [6].

In this chapter, I present our work to develop an efficient impurity solver based on multiconfiguration time–dependent Hartree (MCTDH) method in Fock space formalism, in order to solve the single–impurity Anderson model (SIAM) with time–dependent electron hopping parameters and local Coulomb repulsion, which is a core component for the non–equilibrium dynamical mean field theory (DMFT) for studying femtosecond pump–probe experiments on the strongly correlated materials.

5.1 Principles of dynamical mean field theory

This section aims at giving a brief introduction to the DMFT method, based on published literature in the DMFT community.

A main concept of DMFT is a projection onto a set of spatially localized single–particle orbitals, which generate a subspace of the total Hilbert space, dubbed the correlated subspace $\mathcal{C}$, in which many–body correlation effects can be treated in a non-perturbative manner. The correlation can essentially reshape the electronic structure near the Fermi surface, which is treated as the non–perturbative correction to the one–electron energy

band theory. Fig. 5.1 [7] sketches the hybrid density functional theory (DFT) – DMFT approach, where the DMFT correction on electron density $\rho(r) = \rho_{\mathrm{DFT}} + \Delta\rho(r)$ is feed back to the DFT, and a self–consistent procedure leads to the final solution of electronic structure. In order to understand the underlying physical scenario revealed by the pump–probe experiments, growing theoretical effort has been devoted to establish microscopic description of strongly correlated lattice models out of equilibrium. A promising framework to capture the both ultrafast dynamics and strong electronic correlation is the nonequilibrium formulation of dynamical mean field theory (DMFT) [8, 9, 10].

In the framework of DMFT, a lattice model such as the Hubbard model is mapped onto an effective impurity model, which consists of a single site of the lattice (impurity) coupled to a non–interacting medium, where electrons are exchanged between the impurity site and the medium. One of the key ingredients required for advancing DMFT to nonequilibrium regime is to establish methods to solve the real–time dynamics of the single impurity model

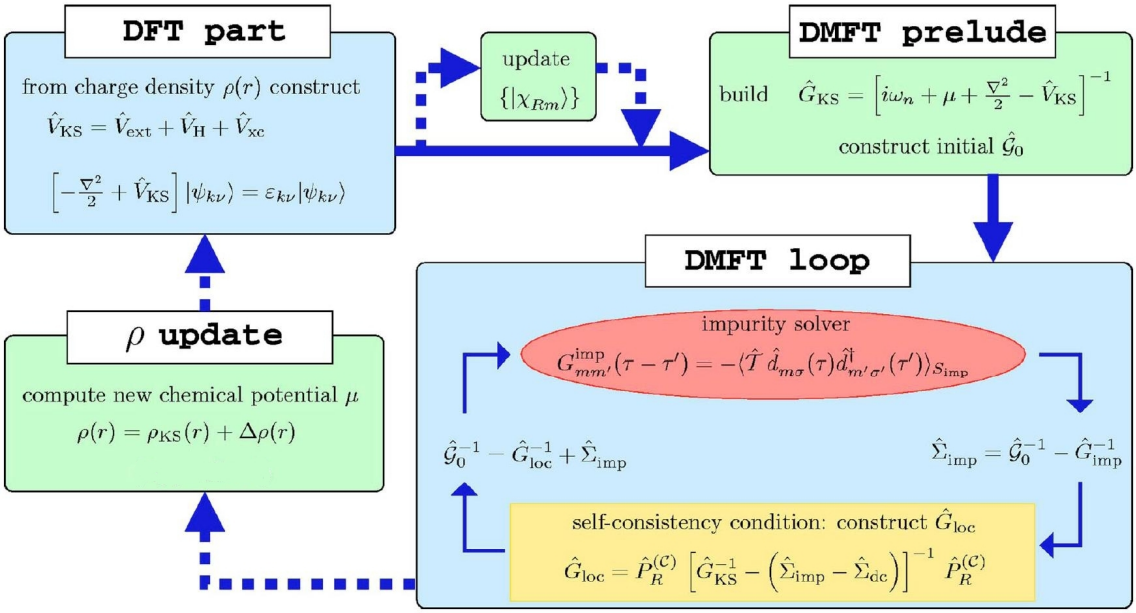

Figure 5.1: The self–consistent loop for LDA+DMFT scheme. The electron density ρ determines the DFT Kohn–Sham (KS) potential V_{KS}, from which one acquire the KS eigenvalues and eigenfunctions. The KS Green function is then constructed and feed to the DMFT cycle. In the converged DMFT loop, a new electron density is generated, taking into account the Coulomb correlation effect, the updated electron density $\rho = \rho_{\mathrm{Ks}} + \Delta\rho$ is then passed on to the DFT. The DFT–DMFT loop is iterated until convergence of the self energy. This figure is taken from Ref. [7].

far from equilibrium. In the previous work of K. Balzer and M. Eckstein *et al.* [11], a robust Hamiltonian–based impurity solver scheme was established for nonequilibrium DMFT based on the discretization effective DMFT medium into a finite number of bath orbitals. The self consistent discretization procedure further maps the DMFT impurity model to a single–impurity Anderson model (SIAM), which is then solved by exact diagonalization method [11, 12]. The mapping of the DMFT impurity model to SIAM is advantageous, because it allows us to access intermediate coupling regime, without presuming that either on-site Coulomb interaction or hopping is small.

In this chapter, I introduce the highly efficient multiconfiguration time–dependent Hartree method, which is originally developed for the time propagation of nuclear wave packets in molecular dynamics [13, 14], to treat the real–time dynamics of the SIAM. Despite the accuracy of exact diagonalization method, which is equivalent to time–dependent full configuration interaction (TDCI), the notorious scaling of its Hilbert subspace dimension, as a function of number of bath sites of SIAM, prohibits us to acquire faithfully the electron dynamics at long time scales. Intuitively, as the dynamics approaches longer times, the electrons can explore wider space in the lattice, therefore one needs more bath sites in the SIAM to guarantee that the SIAM is a faithful mapping of the original lattice Hubbard model, i.e. the growing SIAM reflects the expanding accessible area of the electrons appearing around the impurity site.

The MCTDH method provides a route to represent the dynamical wave function with a minimal set of time–dependent basis functions that co-move with the evolving wave function. This feature can lead to tremendous reduction of configuration space dimension, therefore may allows us to reach long time dynamics in nonequilibrium DMFT. Moreover, MCTDH based impurity solver can be readily incorporated with its more powerful extension, the multi–layer multiconfiguration time–dependent Hartree (ML-MCTDH) [15, 16, 17].

In order to combine nonequilibrium dynamical mean-field theory (DMFT) [10, 18, 19] and the multiconiguration time-dependent Hartree (MCTDH) method, which we propose as impurity solver, I here give a brief introduction to the DMFT framework I employ in this thesis, followed by a detailed description of the application of MCTDH to Fock space dynamics.

From a general perspective, one is interested in the real-time evolution of a lattice quantum many-body system like the single-band Hubbard model

$$H(t) = \sum_{ij\sigma} t_{ij}(t)\, c^{\dagger}_{i\sigma} c_{j\sigma} + U(t) \sum_{i} (n_{i\uparrow} - \tfrac{1}{2})(n_{i\downarrow} - \tfrac{1}{2})\,, \tag{5.1}$$

which is initially in thermal equilibrium at temperature $T = 1/\beta$, and evolves unitarily

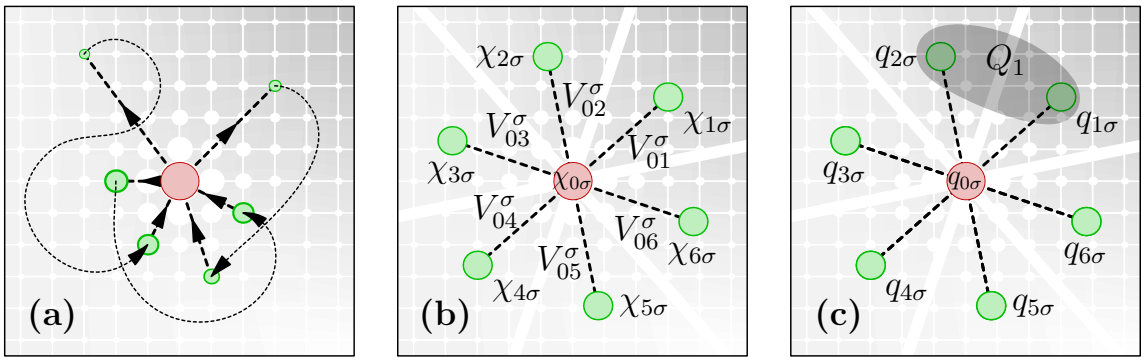

Figure 5.2: (a) DMFT impurity problem according to the action of Eq. (5.3). The arrows illustrate the effect of the two-time hybridization function $\Lambda_\sigma(t,t')$ which describes all kind of processes where a particle of spin σ jumps at a time t from the impurity site (red) to a lattice site i (green), propagates forward or backward in time from site i to site j, and at a time t' jumps back to the impurity. (b) Representation of the DMFT bath by a single-impurity Anderson model (SIAM) with six bath spin orbitals $\chi_{l\sigma}$, $l \geq 1$. (c) SIAM degrees of freedom that enter the MCTDH ansatz of Eq. (2.19).

under the time-dependent Hamiltonian $H(t)$. In Eq. (5.1) the operator $c^\dagger_{i\sigma}$ ($c_{i\sigma}$) creates (annihilates) an electron with spin σ on site i of the crystal lattice, $n_{i\sigma}$ is the spin-density, $t_{ij}(t)$ is the hopping matrix element between sites i and j, and $U(t)$ denotes the local Coulomb repulsion. For the purpose of methodological development, we adopt a parametrized model with given hopping matrix elements and local Coulomb repulsion. In practical material simulation, t_{ij} and U can be determined in an *ab initio* manner, e.g. within the self consistent field density functional theory–dynamical mean field theory (SC-DFT-DMFT) scheme [7].

In our time–dependent single–band Hubbard model, the time unit is defined as the inverse of the electron hopping parameter at the end of dynamics one considers, namely $\hbar/\tilde{t}_{ij}(t \to \infty)$, which corresponds to the time scale of several tens of femtoseconds. For example, $\tilde{t}_{ij} \simeq 40$ meV in one–dimensional organic Mott–insulator, one time unit then corresponds to $\simeq 16.5$ femtoseconds, in transition metal oxides, $\tilde{t}_{ij}$ lies in the range of $7 \sim 300$ meV, the time unit in this case lies accordingly in the range of $2.2 \sim 94.0$ femtoseconds.

5.1.1 Nonequilibrium DMFT and Hamiltonian-based impurity solvers

In previous work by K. Balzer and M. Eckstein *et al.* [11], a comprehensive framework is established for nonequilibrium DMFT, which is briefly presented in the following.

The central task of nonequilibrium DMFT based on the Keldysh formalism [20] is to compute the local contour-ordered Green (or correlation) function

$$G_\sigma(t,t') = -\mathrm{i}\langle T_\mathcal{C} c_\sigma(t) c_\sigma^\dagger(t')\rangle_{S_\mathrm{loc}} \tag{5.2}$$

of an effective single-site impurity model which exactly replaces the original translationally invariant lattice problem (5.1) in the limit of an infinite lattice coordination Z (and is approximate at finite dimensions). The action S_loc of the effective model is given by

$$\begin{aligned} S_\mathrm{loc} &= -i\int_\mathcal{C} \mathrm{d}t \left[U(t)(n_\uparrow(t)-\tfrac{1}{2})(n_\downarrow(t)-\tfrac{1}{2}) - \mu\sum_\sigma n_\sigma(t)\right] \\ &\quad -i\int_\mathcal{C}\int_\mathcal{C} \mathrm{d}t\,\mathrm{d}t' \sum_\sigma \Lambda_\sigma(t,t') c_\sigma^\dagger(t) c_\sigma(t')\,, \end{aligned} \tag{5.3}$$

where the first part contains the Hamiltonian of an isolated site of the original lattice at a chemical potential μ, and the second part connects the site to a noninteracting continuous bath which in nonequilibrium is defined by the hybridization function $\Lambda_\sigma(t,t')$. The integrations are performed over the full L-shaped Keldysh contour.

In single-site DMFT, the bath incorporates retardation effects which come from a local self-energy $\Sigma_i(t,t')$ and therefore must be determined self-consistently. Specifically for a Bethe lattice with nearest-neighbor hopping and semi-elliptical density of states, the bath is characterized by a hybridization function of closed form [21],

$$\Lambda_\sigma(t,t') = v(t) G_\sigma(t,t') v(t')\,. \tag{5.4}$$

where the hopping matrix elements in Eq. (5.1) are rescaled according to $t_{ij}(t) \to v(t)/Z$.

Unfortunately, the DMFT action of the form (5.3) does not allow for a direct solution of the impurity problem with Hamiltonian-based methods. However an optimal representation of S_loc in terms of a time-dependent impurity Hamiltonian with finitely many bath orbitals can be obtained by a suitable decomposition of the two-time hybridization function. Formally such a mapping requires that all impurity correlation functions $\langle \mathcal{O}(t_1)\ldots\rangle$

for S_{loc} are the same in the final impurity Hamiltonian $H'(t)$, i.e.,

$$\begin{aligned} & \frac{\mathrm{Tr}\left(\mathrm{T}_C\left\{\exp\left(S_{\mathrm{loc}}\right)\mathcal{O}(t_1)\ldots\right\}\right)}{\mathrm{Tr}\left(\mathrm{T}_C\left\{\exp\left(S_{\mathrm{loc}}\right)\right\}\right)} \\ \stackrel{!}{=} \; & \frac{\mathrm{Tr}\left(\mathrm{T}_C\left\{\exp\left(-i\int_{\mathcal{C}}\dot{H}'(t)\right)\mathcal{O}(t_1)\ldots\right\}\right)}{\mathrm{Tr}\left(\mathrm{T}_C\left\{\exp\left(-i\int_{\mathcal{C}}\dot{H}'(t)\right)\right\}\right)} \,. \end{aligned} \tag{5.5}$$

A particularly convenient mapping [11] becomes possible for the single-impurity Anderson model (SIAM) where $H' = H_{\mathrm{SIAM}} = H_{\mathrm{imp}} + H_{\mathrm{bath}} + H_{\mathrm{hyb}}$ with

$$\begin{aligned} H_{\mathrm{imp}} &= -\mu\sum_{\sigma} n_{0\sigma} + U(t)\left(n_{0\uparrow}-\tfrac{1}{2}\right)\left(n_{0\downarrow}-\tfrac{1}{2}\right) \,, \\ H_{\mathrm{hyb}} &= \sum_{l=1}^{L}\sum_{\sigma}\left(V_{0l}^{\sigma}(t)c_{0\sigma}^{\dagger}c_{l\sigma} + \mathrm{H.c.}\right) \,, \\ H_{\mathrm{bath}} &= \sum_{l=1}^{L}\sum_{\sigma}(\epsilon_{l\sigma}-\mu)c_{l\sigma}^{\dagger}c_{l\sigma} \,. \end{aligned} \tag{5.6}$$

Here, the impurity site is coupled in a star-pattern by hopping processes of amplitude $V_{0l}^{\sigma}(t)$ to L individual noninteracting bath orbitals of energy $\epsilon_{l\sigma}$, and the operator $c_{l\sigma}$ ($c_{l\sigma}^{\dagger}$) annihilates (creates) an electron in a spin orbital $\chi_{l\sigma}$ at bath site l for $l > 0$, and at the impurity for $l = 0$. The hybridization function of the SIAM is given by

$$\Lambda'_{\sigma}(t,t') = \sum_{l=1}^{L} V_{0l}^{\sigma}(t)g(\epsilon_{l\sigma},t,t')V_{l0}^{\sigma}(t') \,, \tag{5.7}$$

where $g(\epsilon,t,t') = -\mathrm{i}[\theta_{\mathcal{C}}(t,t')-f(\epsilon)]\mathrm{e}^{-\mathrm{i}\epsilon(t-t')}$ is the Green function of an isolated bath orbital, $f(\epsilon) = 1/(\mathrm{e}^{\beta\epsilon}+1)$ denotes the Fermi distribution and $\theta_{\mathcal{C}}$ is the contour step function.

If the bath is initially decoupled from the impurity (this is commonly referred to as the atomic limit), the initial state of the system is completely described by the impurity density matrix ρ, and in Eq. (5.3) the Matsubara and mixed components of the hybridization function vanish, $\Lambda^{\mathrm{M}} = \Lambda^{\lceil} = \Lambda^{\rceil} = 0$. The open parameters in the SIAM can then be obtained by demanding that the greater and lesser components of the original hybridization function $\Lambda_{\sigma}(t,t')$ and $\Lambda'_{\sigma}(t,t')$ of Eq. (5.7) are identical for all times t and t' on the real part of the contour.

In practice, this leads over to a matrix decomposition of $\Lambda_{\sigma}(t,t')$, where the matrix rank N_{t} is defined by the discretization of the times t and t' according to $0, \delta t, 2\delta t, \ldots, (N_{\mathrm{t}}-1)\delta t$. By choosing the bath energies of the SIAM such that the occupations $f(\epsilon_{l\sigma}-\mu)$ are either 0

or 1, the greater and lesser components can be decomposed independently of one another,

$$
\begin{aligned}
-\mathrm{i}\Lambda^{<}_{\sigma}(t,t') &= \sum_{l=1}^{L/2} V^{\sigma}_{0l}(t)[V^{\sigma}_{0l}(t')]^{*}\,, \\
\mathrm{i}\Lambda^{>}_{\sigma}(t,t') &= \sum_{l=L/2+1}^{L} V^{\sigma}_{0l}(t)[V^{\sigma}_{0l}(t')]^{*}\,,
\end{aligned}
\tag{5.8}
$$

where we have occupied the first half of the spin orbitals $\chi_{l\sigma}$ and left the other half empty (note that non-uniform partitions are also possible).

It is obvious that the equality in Eq. (5.8) holds strictly only in the limit $L \to \infty$, given the continuity of the DMFT bath. However, appropriate representations can usually be obtained already for a rather small number of bath orbitals [22]. Furthermore, the use of a causal low-rank Cholesky approximation in Eq. (5.8) guarantees that the representation of the hybridization function is always correct at short times, see Ref. [11] for details. In this context a gradual increase of L allows us to successively approach longer and longer simulation times.

5.2 MCTDH based nonequilibrium DMFT impurity solver

5.2.1 MCTDH in electronic Fock space

I apply the MCTDH method [13, 14, 23], which is introduced in chapter 2.2, to the time–dependent single–impurity Anderson model appearing in the nonequilibrium DMFT. To this specific application, it is convenient to implement the MCTDH solver with the Fock space formulation of electronic wave functions and Hamiltonian.

The impurity model is a system containing N electrons and can be described by a set of M orthonormal spin orbitals $\{\chi_1(\mathbf{x}), \chi_{\mathbf{2}}(\mathbf{x}), \ldots, \chi_{\mathbf{M}}(\mathbf{x})\}$, where $M \geq N$.

The corresponding N-electron wave function lives in the Hilbert (sub)space $\mathcal{H}(M, N)$ and can be constructed from antisymmetrized products (i.e, Slater determinants) of these basis functions. In previous work of K. Balzer and M. Eckstein [11], a Hamiltonian-based impurity solver was developed, using the Hilbert space representation of electronic wave function [11]. The Hilbert space formalism has also led to the development of multiconfiguration time–dependent Hartree for fermions (MCTDHF) [24, 25, 26, 27]. The MCTDHF *ansatz* invokes fermionic symmetry in the wave function, so the f-electron wave function is expressed as linear combination of Slater determinants, namely the configuration state functions (CSFs). Explicitly, in MCTDHF scheme, an f-electron N-orbital wave function is written as

$$\Psi(q_1, \cdots, q_f) = \sum_{j_1}^{N} \cdots \sum_{j_f}^{N} C_{j_1,\cdots,j_f}(t) \prod_{\kappa=1}^{f} \phi_{j_\kappa}^{(\kappa)}(q_\kappa, t)\,, \tag{5.9}$$

where q_i and $\phi_{j_\kappa}^{(\kappa)}(q_\kappa, t)$ are electronic coordinates and orbitals, respectively. Eq. 5.9 is slightly different from the MCTDH *ansatz* (Eq. 2.19), the MCTDHF coefficient $C_{j_1,\cdots,j_f}(t)$ carries fermionic symmetry, namely it is antisymmetric with respect to their indices. The time propagation of electronic wave function with variationally optimal B's and ϕ's are similar to that in MCTDH using the Dirac–Frenkel variational principle [28].

Without explicitly invoking fermionic symmetry in the wave function, an equivalent and convenient way to implement the MCTDH method for the impurity problem is to use the Fock space representation of fermion wave function [15]. The Fock space MCTDH of second quantization representation, dubbed MCTDH-SQR [15], may have particular advantage over the MCTDHF scheme, when one extends the depth of basis function layers, namely invoking ML-MCTDH scheme. As introduced in chapter 3, the extension to ML-MCTDH scheme relies on effective mode combination. However, in the MCTDHF,

combining coordinates of different electrons into one logical mode would face difficulty to conserve the fermionic symmetry of the wave function. For example, suppose one has a 3–layer MCTDHF scheme, a mode combined basis $\phi_{j_\kappa}(Q_\kappa, t)$ with $Q_\kappa = \{q_{1_\kappa}, \cdots, q_{d_\kappa}\}$ in the 1st layer needs to be further expanded as a d_κ–dimensional wave function like object with time–dependent orbitals as in Eq. 2.20, it remains to be an open question to determine the appropriate symmetry of the expansion coefficient in the 2nd layer, such that the fermionic symmetry of the f-electron wave function $\Psi(q_1, \cdots, q_f)$ is conserved. Possible solutions might be to carefully prepare the initial wave function in the N-layer representation, which possesses fermionic symmetry. Since the Hamiltonian operator would not break the fermionic symmetry in the time propagation, one might be able to construct a ML-MCTDHF scheme. Such possibility has not been investigated yet.

On the contrary, in the Fock space MCTDH-SQR of fermions does not explicitly invoke antisymmetry in the wave function, the fermionic symmetry is instead *transferred* to the Hamiltonian operator. The mode combination can be applied in exactly the same way as the non–symmetric MCTDH, it can be straightforwardly extended to Fock space fermionic ML-MCTDH [15]. The tree structure of the corresponding ML-MCTDH scheme is sketched in Fig. 5.3. For M spin orbitals, the basis of the Fock space (denoted as $\mathcal{F}(M)$) is given by

$$|n_1, n_2, \ldots, n_p, \ldots, n_M\rangle = \prod_{P=1}^{M} (c_P^\dagger)^{n_P} |0_1, 0_2, \ldots, 0_M\rangle \,. \tag{5.10}$$

where $n_p = 0, 1$ are the allowed occupations of the spin orbital χ_p, and $c_P^\dagger$ denotes the fermionic creation operator, satisfying the anticommutation relations with the associated annihilation operator c_P,

$$\begin{aligned} \{c_P, c_Q^\dagger\} &\equiv c_P c_Q^\dagger + c_Q^\dagger c_P = \delta_{PQ} \,, \\ \{c_P, c_Q\} &= \{c_P^\dagger, c_Q^\dagger\} = 0. \end{aligned} \tag{5.11}$$

Their action on the Fock state basis is determined by Pauli exclusion principle, i.e.,

$$\begin{aligned} c_P^\dagger |n_1, n_2, \ldots, 0_P, \ldots, n_M\rangle &= \prod_{Q=1}^{P-1} (-1)^{n_Q} |n_1, n_2, \ldots, 1_P, \ldots, n_M\rangle \\ c_P^\dagger |n_1, n_2, \ldots, 1_P, \ldots, n_M\rangle &= 0, \end{aligned} \tag{5.12}$$

where the phase factor $\prod_{Q=1}^{P-1}(-1)^{n_Q}$ accounts for all permutations needed in order to bring Fock state $|1_P, n_1, n_2, \ldots, n_M\rangle$ to $|n_1, n_2, \ldots, 1_P, \ldots, n_M\rangle$.

For implementation of the impurity model in MCTDH, it is practical to represent the primitive Fock space basis and the fermionic operators in matrix form. The occupation

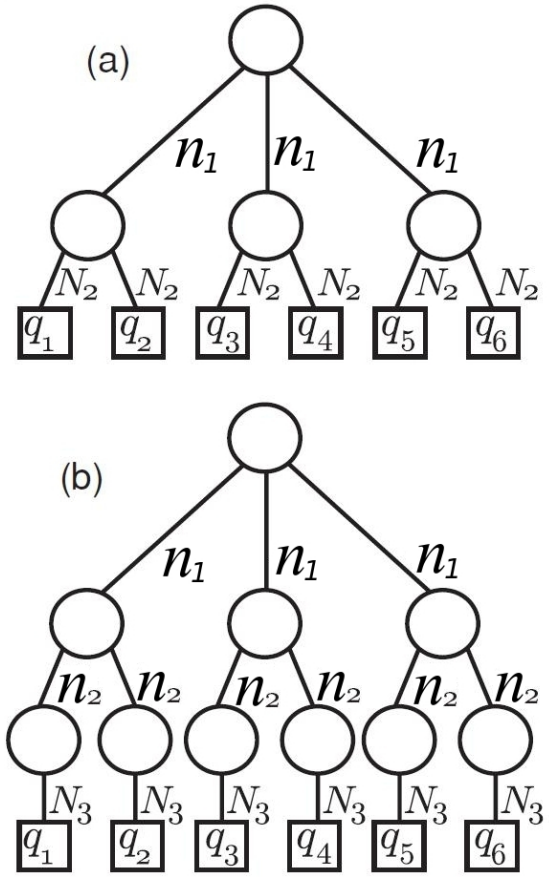

Figure 5.3: Tree structure of (a) MCTDH and (b) ML-MCTDH wave functions of a 6 spin orbital model, combined into groups of two spin orbitals. The bottom layer is supported by the primitive Fock state basis. n_1 and n_2 by the edge of the tree diagram represent the number of SPFs used to represent each combined mode. $N_2 = 2$ for MCTDH and $N_3 = 2$ for ML-MCTDH, which corresponds to 2 occupancy state of the spin orbital. This figure is taken from Ref. [17]. Copyright © American Institute of Physics (AIP).

number states of spin orbital χ_j are described by a rank-2 vector space,

$$\begin{aligned} |n_j = 0\rangle &\Leftrightarrow \begin{pmatrix} 0 \\ 1 \end{pmatrix} \\ |n_j = 1\rangle &\Leftrightarrow \begin{pmatrix} 1 \\ 0 \end{pmatrix} \end{aligned} \tag{5.13}$$

The matrix representation of creation operator can be written as

$$\begin{aligned} c_P^\dagger &\equiv \left(\prod_{Q=1}^{P-1} (-1)^{n_Q} \right) \tilde{c}_P^\dagger = \left(\prod_{Q=1}^{P-1} S_Q \right) \tilde{c}_P^\dagger \\ \tilde{c}_P^\dagger &\equiv \begin{pmatrix} 0 & 1 \\ 0 & 0 \end{pmatrix} \\ S_Q &\equiv \begin{pmatrix} -1 & 0 \\ 0 & 1 \end{pmatrix}. \end{aligned} \tag{5.14}$$

One can readily find the matrix form of annihilation operator as Hermitian conjugate of

the creation operator $\hat{c}_P^\dagger$,

$$\begin{aligned} c_P &\equiv \left(\prod_{Q=1}^{P-1}(-1)^{n_Q}\right)\tilde{c}_P \\ \tilde{c}_P &\equiv \begin{pmatrix} 0 & 0 \\ 1 & 0 \end{pmatrix}. \end{aligned} \tag{5.15}$$

The number of electrons in a Fock state $|n_1, n_2, \ldots, n_M\rangle$ is given by $N = \sum_{P=1}^{M} n_P$, and the electron number operator $\hat{n}_P$ for spin orbital χ_P can be written as

$$\hat{n}_P \equiv \begin{pmatrix} 1 & 0 \\ 0 & 0 \end{pmatrix}. \tag{5.16}$$

As an example, one may consider a spinless two orbital model, an electron hopping operator $t_{12}c_1^\dagger c_2$ in matrix representation acting on a Fock state $|0_1 1_2\rangle$ could be conveniently evaluated as

$$\begin{aligned} t_{12}c_1^\dagger c_2 \,|0_1 1_2\rangle &= t_{12}\tilde{c}_1^\dagger \,(S_1\tilde{c}_2)\,|0_1 1_2\rangle \\ &= t_{12}\begin{pmatrix} 0 & 1 \\ 0 & 0 \end{pmatrix}_1 \otimes \begin{pmatrix} -1 & 0 \\ 0 & 1 \end{pmatrix}_1 \begin{pmatrix} 0 & 0 \\ 1 & 0 \end{pmatrix}_2 \left[\begin{pmatrix} 0 \\ 1 \end{pmatrix}_1 \otimes \begin{pmatrix} 1 \\ 0 \end{pmatrix}_2\right] \\ &= t_{12}\begin{pmatrix} 1 \\ 0 \end{pmatrix}_1 \otimes \begin{pmatrix} 0 \\ 1 \end{pmatrix}_2 \\ &= t_{12}\,|1_1 0_2\rangle\,. \end{aligned} \tag{5.17}$$

We see from Eq. 5.17 that in second quantization representation, all operators are in a product form, which is advantageous for the treatment using MCTDH scheme.

For the benchmark calculations, we apply two-layer MCTDH as an impurity solver and evaluate its performance on the basis of computational complexity. In the first part, we outline the procedure for a simple test bath and compute the time-dependent wave function of the corresponding SIAM with L bath sites for various on-site interactions U. In the second part, we discuss the self-consistency and illustrate the computation of the impurity Green function. Starting from the atomic limit, the impurity site $q_{0\sigma}$ is initially decoupled from the bath and is occupied by a single up- or down-spin electron. Consistent with the decomposition scheme outlined in Sec. 5.1.1, the bath orbitals $q_{1\sigma}$ to $q_{L\sigma}$ have different initial populations; the first half is doubly occupied whereas the second half is empty.

To quantify the dimension scaling in comparison to exact diagonalization (ED) we determine the maximum time to which observables are still physically meaningful in the

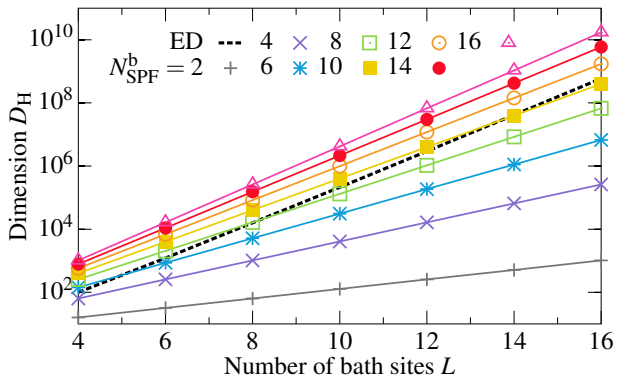

Figure 5.4: Hilbert space dimension of the SIAM as function of the number of bath sites L (black dashed line) and dimension of the corresponding A-vectors in MCTDH (colored lines) for a setup where four bath spin orbitals are treated in a combined mode ($N^{\mathrm{b}}_{\mathrm{CM}}$=4) and $N^{\mathrm{b}}_{\mathrm{SPF}}$ single-particle functions are involved, Eq. (5.19).

SIAM model. While the dimension of the Hilbert space of the SIAM is given by

$$D_{\mathrm{H}} = \binom{L+1}{L/2+1}\binom{L+1}{L/2}, \tag{5.18}$$

the A-vectors $A_{j_1\ldots j_p}$ in MCTDH have dimension

$$D = 2^2 (N^{\mathrm{b}}_{\mathrm{SPF}})^{2L/N^{\mathrm{b}}_{\mathrm{CM}}} \tag{5.19}$$

for an orbital partition scheme with $N^{\mathrm{b}}_{\mathrm{CM}}$ bath spin orbitals in a combined mode and each combined mode being represented by $N^{\mathrm{b}}_{\mathrm{SPF}}$ SPFs. The impurity degrees of freedom are treated in a single separate mode and are accounted for by the factor 2^2. From Fig. 5.4 we observe that (despite the exponential scaling of the configuration space with L) the application of MCTDH can become favorable against ED for specific numbers of SPFs $N^{\mathrm{b}}_{\mathrm{SPF}}$ at fixed L, provided that the relevant observables of the impurity model are satisfactorily resolved in time. The scaling of MCTDH can be further improved by introducing its ML-MCTDH extension.

5.2.2 MCTDH for a typical SIAM

To assess the performance of MCTDH for a time-dependent impurity problem which is representative for a DMFT calculation, we solve the SIAM for a bath which has temperature $T = \beta^{-1} = 1$ and is characterized by a (noninteracting) equilibrium Green function with semi-elliptical density of states,

$$g^{\gtrless}_{\sigma}(t,t') = \mp \mathrm{i} \int d\omega f^{\gtrless}(\omega) A(\omega) \mathrm{e}^{-\mathrm{i}\omega(t-t')}, \tag{5.20}$$

where $f^{<}(\omega) = f(\omega) = 1/(\mathrm{e}^{\beta\omega}+1)$, $f^{>}(\omega) = 1 - f(\omega)$ and $A(\omega) = \frac{1}{2\pi}\sqrt{4-\omega^2}$.

At time $t = 0$, we assume a sudden switch-on of the hopping in the physical (Bethe) lattice according to $v(t) = \theta(t)$, where θ denotes the Heavyside step function. The complex

hopping parameters $V_{0l}^{\sigma}(t)$ in the SIAM then follow from a low-rank Cholesky decomposition of the bath hybridization function $\Lambda_{\sigma}(t,t') = v(t)g_{\sigma}(t,t')v(t')$. Figure 5.5 shows the resulting hopping parameters for a setup with $L = 4$ and $L = 6$ bath sites on a time window up to $t = 10$; the time discretization comprises $n_t = 500$ time steps.

To examine the MCTDH wave function $|\Psi(t)\rangle$ of the SIAM for different numbers of SPFs, we compute the time-dependent impurity double occupancy

$$\langle d \rangle(t) = \langle \Psi | n_{0\uparrow}(t) n_{0\downarrow}(t) | \Psi \rangle \tag{5.21}$$

for various sizes L of the bath and different on-site interactions and compare it to exact reference data which is obtained by ED. In all calculations we group four bath degrees of freedom (i.e., four bath spin orbitals) into one combined mode, $N_{\mathrm{CM}}^{\mathrm{b}} = 4$ in Eq. (5.19). As each spin orbital has two degrees of freedom, the span with $2^4 = 16$ SPFs represents the full Fock space that is equivalent to the exact diagonalization basis space. In this case, the SPF basis are effectively time–independent, because in Eq. 2.22 the projector $P^{(\kappa)} = 1$ and

$$i\dot{\varphi}^{(\kappa)} = 0. \tag{5.22}$$

(A) Comparison to exact diagonalization

In Fig. 5.6a and 5.6b, we show MCTDH data for the SIAM with four bath sites and compare the dynamics for $U = 2$ with those for $U = 6$. In both cases, the MCTDH data for $N_{\mathrm{SPF}}^{\mathrm{b}} = 16$ (orange lines) correspond to the full configuration interaction result and thus perfectly lie on top of the ED curves. Since the dynamics starts from the atomic limit with a singly-occupied impurity at $t = 0$, the double occupation is initially zero and then becomes finite and oscillatory; note that the density on the impurity site is a constant of motion by construction of the hopping parameters $V_{0l}^{\sigma}(t)$. For $N_{\mathrm{SPF}}^{\mathrm{b}} < 16$ the MCTDH

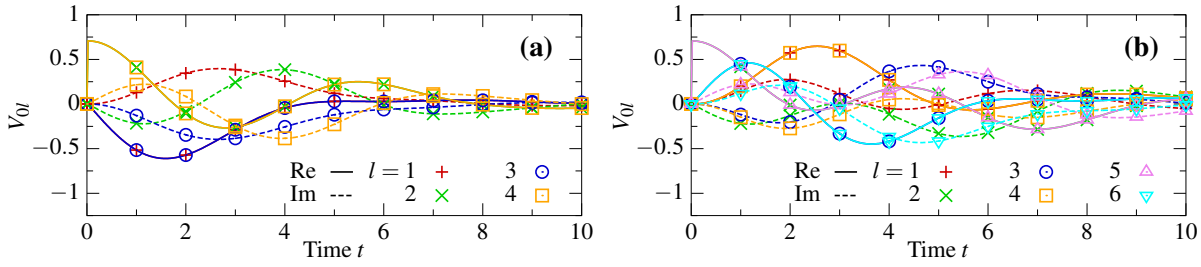

Figure 5.5: Time evolution of the hopping parameters $V_{0l}(t) = V_{0l}^{\uparrow}(t) = V_{0l}^{\downarrow}(t)$ for a SIAM with (a) $L = 4$ and (b) $L = 6$ bath orbitals as obtained for a reference bath which is governed by the equilibrium Green function of Eq. (5.20) with inverse temperature $\beta = 1$.

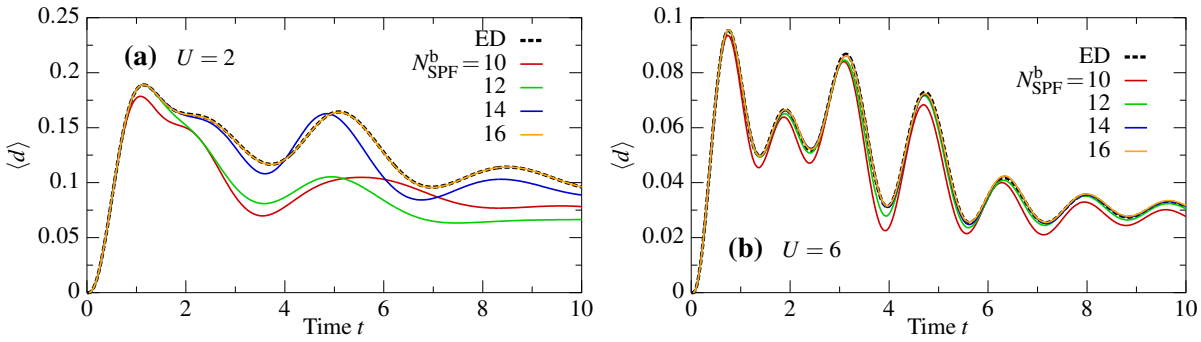

Figure 5.6: Time-dependent double occupancy $\langle d \rangle(t)$ of the impurity site for the SIAM with $L = 4$ bath orbitals at (a) $U = 2$ and (b) $U = 6$, calculated by exact diagonalization (ED) and MCTDH with various numbers of SPFs (N^{b}_{SPF}).

results are approximate, and we generally find that convergence towards ED [by increasing the number of SPFs] is harder to reach as U decreases. This behavior can be attributed to the fact that, during the time evolution at small U, the inter-site hopping of electrons (i.e., the influence of H_{hyb} in Eq. (5.6)) is more pronounced due to smaller energy gain from localization. Consequently, the wave function expands to a larger area in configuration space which requires an increased number of time-adjusted SPFs $\varphi_j(t)$ to optimally cover the support of $|\Psi(t)\rangle$. For strong coupling (large U) on the contrary, the wave function implies relatively weak inter-coordinate correlation such that convergence can be reached faster.

In summary, we expect that MCTDH can accurately capture the time evolution of the nonequilibrium impurity model in the moderate to strong coupling regime, where U is essentially larger than the kinetic energy. Moreover, it is worth mentioning that the partition of spin orbitals into combined physical modes can affect the performance of MCTDH [17], i.e., the dimension of the SPF basis space needed to converge the time-dependent observables. In cases where the spin orbitals within a combined mode are half filled, the initial phase of the dynamics should already involve a larger number of electronic configurations. Thus one may need a higher-dimensional basis to achieve observables of similar quality. A more favorable partition scheme is to group spin orbitals with the criterion that all bath spin orbitals of a combined mode are initially either empty or fully occupied. This guarantees that only a small set of possible electronic configurations can be accessed within the projected Fock space of a certain combined mode.

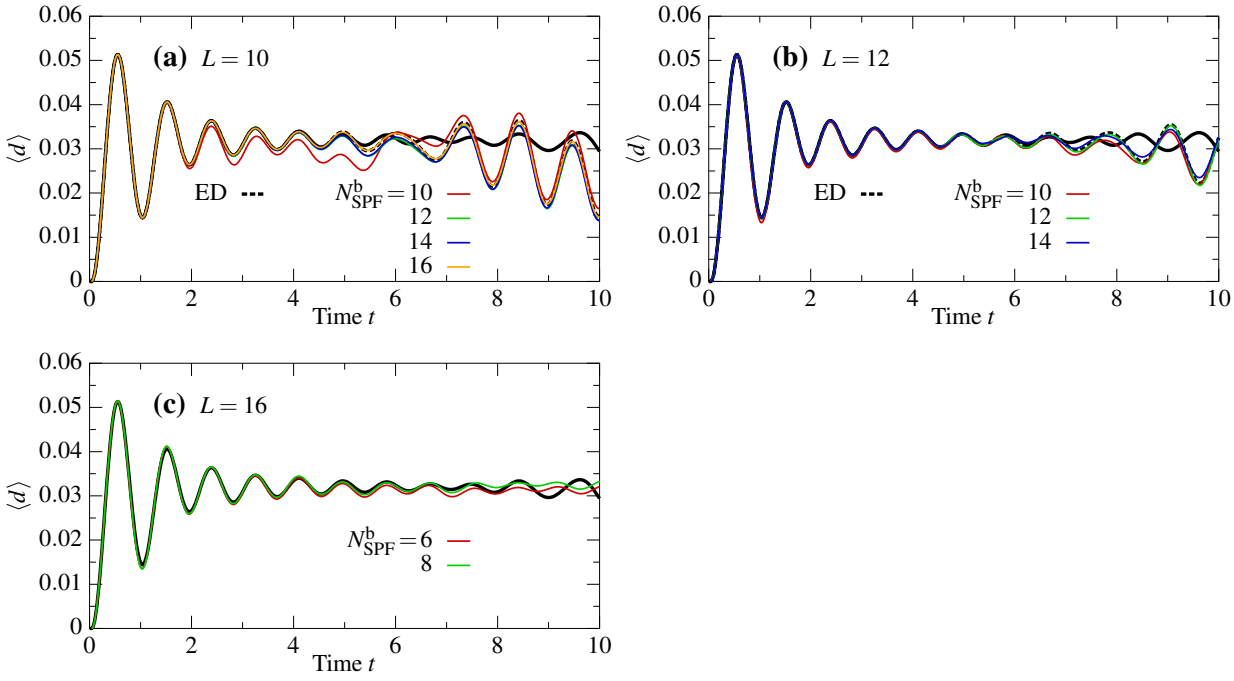

Figure 5.7: Comparison of MCTDH with four combined modes ($N_{\mathrm{CM}} = 4$) and N_{SPF} single-particle functions to exact diagonalization (ED) at an on-site interaction of $U = 10$: Time-dependent impurity double occupancy $\langle d \rangle(t)$ for the SIAM with (a) $L = 10$, (b) $L = 12$ and (c) $L = 16$ bath orbitals. The black solid line, showing the ED result for $L = 14$, acts as reference data to determine the maximum time t_{max} in Fig. 5.8.

(B) Scaling with Hilbert space dimension

Instead of using the full 2^4 static SPFs of the configuration interaction picture (recall the remark regarding the time dependence of the SPFs in Sec. 5.2.1), the dynamics of the double occupancy in Fig. 5.7b is well reproduced already with 12 to 14 time-dependent SPFs. In terms of the dimension of the MCTDH Hilbert space this means a reduction from $D_{\mathrm{H}} = 1024$ to 576 (784) for $N^{\mathrm{b}}_{\mathrm{SPF}} = 12$ (14). However, in this size regime of the SIAM the corresponding ED subspace with dimension $D_{\mathrm{H}} = 100$ is still much smaller, cf. Fig. 5.4.

To define the regime where MCTDH potentially starts to become superior, we perform calculations around the limit of exact diagonalization, i.e., around $L = 14$ bath sites in our implementation ($D_{\mathrm{H}} = 41409225$). Also we confine ourselves to the case of strong coupling where MCTDH converges most rapidly. Figure 5.7a-c shows the time evolution of $\langle d \rangle$ for SIAMs with $L = 10$, 12 and 16 bath orbitals at $U = 10$. To analyze the result we first discuss the additional ED data which are given by the black lines. In all panels, the black solid line indicates the dynamics for the bath [described via Eq. (5.20)] which is

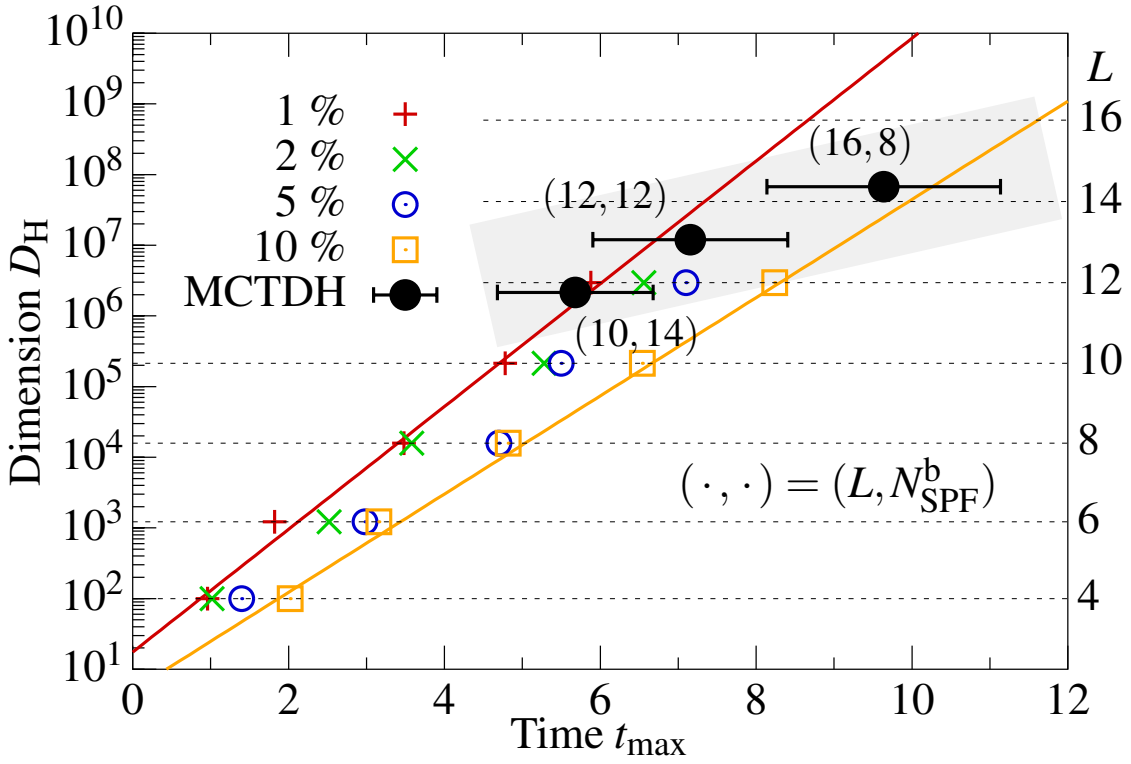

Figure 5.8: Maximum physical time $t_{\max}$ that can be reached in the time evolution of the SIAM with exact diagonalization (colored points) and MCTDH (black dots) at Hilbert space dimension $D_{\mathrm{H}}(L)$ respectively $D_{\mathrm{H}}(L, N_{\mathrm{SPF}})$, allowing for a maximum error between 1 and 10 percent in the double occupation $\langle d \rangle(t_{\max})$; compare with Fig. 5.7a-c. The error bars for the MCTDH results are taken from the (extrapolated) difference of the ED data for 1% and 10% deviation, cf. the red and orange lines.

approximated by 14 SIAM sites and is thus valid to longer times than the black dashed lines in Fig. 5.7a and 5.7b that refer to 10 and 12 bath sites, respectively. Comparing the ED results for $L \leq 12$ with the one for $L = 14$ (which is used as reference) we can extract a maximum physical time $t_{\max}$ which can be reached in the calculation with a certain computational effort measured by the assigned Hilbert space dimension. Allowing for a maximum error of 1-10% in the time-dependent double occupancy (hard cutoff), the colored points in Fig. 5.8 indicate the scaling between $t_{\max}$ and D_{H} for exact diagonalization, systematically including also the simulation results for smaller L.

From the plot it becomes clear that it is exponentially hard to reach long times with a Hamiltonian-based representation of a DMFT bath. However, the interesting question is if a MCTDH partition scheme with fewer and optimally time-evolving SPFs can lead to a more favorable scaling behavior. We obtain indications about this by analyzing the

MCTDH results of Fig. 5.7 for a minimum number of SPFs for which $\langle d \rangle(t)$ is still satisfactorily described within an error of about 5%. While in panels Fig. 5.7a and 5.7b we can directly compare the corresponding ED result with the same number of bath orbitals (see the black dashed lines), in Fig. 5.7c we only have the $L = 14$ data as reference; here we estimate a maximum time of about $t_{\max} = 9$ up to which the oscillation in the double occupancy for $N_{\mathrm{SPF}}^{\mathrm{b}} = 8$ is still decaying as function of time.

The result of the analysis is presented by the black dots labeled by $(L, N_{\mathrm{SPF}}^{\mathrm{b}})$ in Fig. 5.8. Indeed, we find a deviating scaling for MCTDH which roughly follows the delineated gray band as function of $t_{\max}$. With eight SPFs the calculation for $L = 16$ also marks the first point where the effective Hilbert space dimension ($D_{\mathrm{H}} \approx 6.7 \times 10^7$) is clearly reduced in comparison to exact diagonalization ($D_{\mathrm{H}} \approx 5.9 \times 10^8$).

5.2.3 Impurity Green function

For a successful manifestation as out-of-equilibrium impurity solver, MCTDH must be capable to access the two-time Green function $G_{0\sigma}(t, t')$ on the impurity site of the SIAM in a self-consistent manner. From this Green function one can then directly obtain, e.g., the self-energy of the system, the time-dependent momentum distribution or spectroscopic observables of pump-probe experiments [5, 11].

To demonstrate the general procedure and its feasibility we follow Ref. [11] and consider the real-time dynamics of the Hubbard model on the Bethe lattice, starting from the atomic limit and a zero-temperature initial state ($T = 0$). More precisely, we fix the on-site interaction to U=4 and study the dynamics of the paramagnetic phase at half-filling when the nearest-neighbor hopping in the infinite-dimensional lattice is ramped up from zero to $v(t_1) = 1$ with a cosine-shaped profile; in the Hubbard Hamiltonian (5.1) we consider $t_{ij}(t) = \delta_{\langle ij \rangle} v(t)/\sqrt{Z}$ in the limit of infinite coordination number Z.

The DMFT action of the lattice Hubbard model is mapped onto a SIAM with an initial state as in the previous section, i.e., it contains an equal number of empty and doubly-occupied bath sites with energy $\epsilon_l = 0$ and a singly-occupied impurity. Further, the hopping parameters $V_{0l}^{\sigma}(t)$ are spin-independent and are determined self-consistently via the bath hybridization function $\Lambda_\sigma(t, t') = v(t') G_{0\sigma}(t, t') v(t')$, where $G_{0\uparrow} = G_{0\downarrow}$ for all times on the contour. To generate an initial guess for $\Lambda_\sigma(t, t')$ we use the Green function of Eq. (5.20).

From the time-dependent MCTDH wave function $|\Psi(t)\rangle$ of the SIAM, the two independent (lesser and greater) components of the impurity Green function, $G_{0\sigma}^{>}$ and $G_{0\sigma}^{<}$, are

defined as the overlaps

$$G^{>}_{0\sigma}(t,t') = -\mathrm{i}\langle\Psi(t)|\Xi^{>}(t,t')\rangle\,, \qquad (5.23)$$
$$G^{<}_{0\sigma}(t,t') = \mathrm{i}\langle\Psi(t')|\Xi^{<}(t',t)\rangle\,,$$

where the states $\left|\Xi^{\gtrless}(t,t')\right\rangle$ are defined by $|\Xi^{>}(t,t')\rangle = c_{0\sigma}U(t,t')c^{\dagger}_{0\sigma}\,|\Psi(t')\rangle$, $|\Xi^{<}(t,t')\rangle = c^{\dagger}_{0\sigma}U(t,t')c_{0\sigma}\,|\Psi(t')\rangle$ and $U(t,t') = T_{\mathrm{t}}\mathrm{e}^{-i\int_{t'}^{t}\mathrm{d}s\,H'(s)}$ denotes the time-evolution operator for the impurity model (5.6). In practice, we evaluate the two time Green functions as

$$\begin{aligned} G^{>}_{0\sigma}(t,t') &= -\mathrm{i}\langle\Sigma^{>}(t)|\Sigma^{>}(t')\rangle\,, \qquad (5.24)\\ G^{<}_{0\sigma}(t,t') &= \mathrm{i}\langle\Sigma^{<}(t')|\Sigma^{<}(t)\rangle\,, \end{aligned}$$

where $\left|\Sigma^{\gtrless}(t)\right\rangle$ are defined as $|\Sigma^{>}(t)\rangle = U(0,t)c^{\dagger}_{0\sigma}\,|\Psi(t)\rangle$, and $|\Sigma^{<}(t)\rangle = U(0,t)c_{0\sigma}\,|\Psi(t)\rangle$.

Furthermore, since the original Hubbard model we start from has intrinsic particle-hole symmetry but the derived SIAM with a singly-occupied impurity exhibits this symmetry only in the bath subspace, we use an adapted initial state which is a superposition of two degenerate states: One has a spin-up electron occupying the impurity site, and the other has a spin-down electron on the impurity site. An alternative scheme, which we have also implemented to restore electron-hole symmetry, is to first construct Green functions $G^{A}(t,t')$ and $G^{B}(t,t')$ with interchanged particle numbers (i.e., $N_{\uparrow} \leftrightarrow N_{\downarrow}$), and then to average over the two Green functions according to $G(t,t') = \frac{1}{2}[G^{A}(t,t') + G^{B}(t,t')]$.

In Fig. 5.9 I present results for the self-consistent impurity Green functions where the hybridization $\Lambda_{\sigma}(t,t')$ is approximated on a time window $t \in [0,4]$ by a SIAM with $L = 8$ bath sites. One can clearly see that while the density in the system, $\langle n_{\sigma}\rangle(t) = \mathrm{Im}\,G^{<}_{\sigma}(t,t) = 0.5$, is a constant of motion, the time-off-diagonal components of the Green's function containing the spectral information develop as a function of the two times (see the black arrows). Moreover, for times $t,t' \gtrsim 1.5$ where the double occupation in the system approaches a stationary value, also the Green's functions attain quasi static structure as a function of the physical (center of mass) time $(t+t')/2$.

To bring the results to convergence, we have implemented the self-consistency loop in two ways, either iterating on the full (t,t')-mesh or using the time propagation scheme described in Ref. [11]. While the former approach was simpler to implement, the latter is found to be much more efficient because the self-consistency is established for each time slice separately allowing for essentially fewer iterations. Finally, we remark that the tiny changes in the Green's function at later times ($t \gtrsim 3$) are due to discretization of the DMFT bath with only eight bath sites, see, e.g., the red arrow in Fig. 5.9c and compare to the time evolution of the doubly occupancy in Fig. 5.9d which also deviates from the steady state (dashed line) for times $t > 3$. Though still more expensive in terms of configuration space

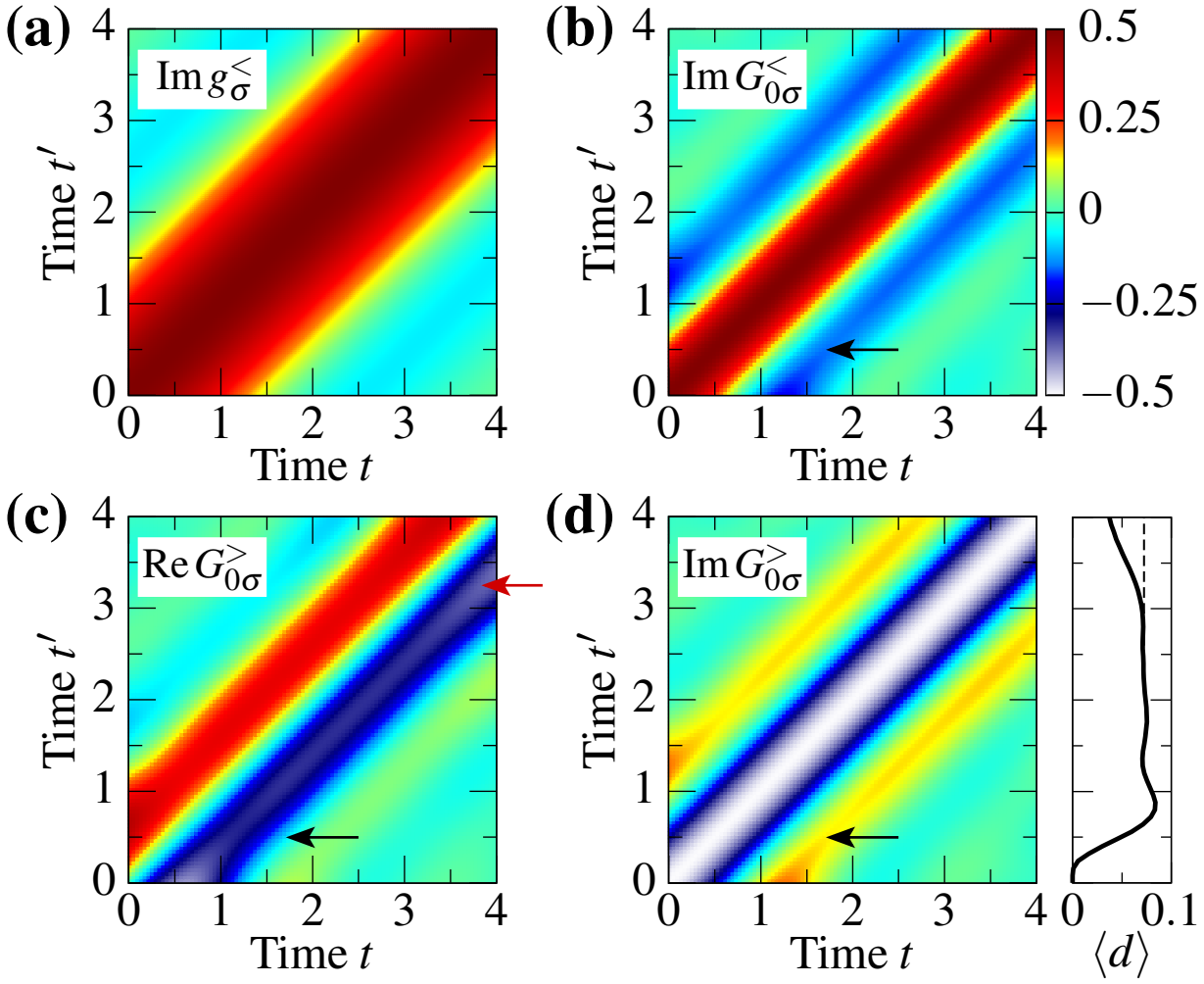

Figure 5.9: (a) Imaginary part of the Green's function $g^{\gtrless}_\sigma(t,t')$ of Eq. 5.20 which is used to compute the initial guess for the hybridization function in the first DMFT iteration. Panels (b)-(d): Self-consistent results for the local impurity Green's function $G^{\gtrless}_{0\sigma}(t,t')$ as obtained from an MCTDH calculation with $L = 8$ bath orbitals in the single-impurity Anderson model; the on-site Coulomb repulsion is $U = 4$. The black arrows indicate the early time domain where the transient dynamics due to the switch-on of the hopping is most pronounced. Furthermore, the red arrow in panel (c) points to the formation of small artifacts in the final *steady* state which are due to the representation of the DMFT bath with finitely many bath orbitals. Furthermore, in panel (d), the black solid line shows the time evolution of the double occupation $\langle d \rangle$ in the system.

dimension for $L = 8$, the calculation of Fig. 5.9 shows that MCTDH can be successfully embedded as an impurity solver in nonequilibrium DMFT.

So far we have devised an efficient methodology to solve impurity model of nonequilib-

rium DMFT based on multiconfiguration time-dependent Hartree method. The MCTDH method provides a variationally optimized representation of time-dependent fermionic wave function, which can tremendously reduce the dimension of basis function space. This is a crucial feature to overcome the notorious exponential scaling barrier that hinders the access to long time dynamics of nonequilibrium DMFT. We have implemented the MCTDH impurity solver based on the Fock space second quantization formalism, with help of matrix representation of fermionic operators and Fock state basis. This formalism can be readily extended to the more flexible ML-MCTDH scheme [15], which can bring the dynamics of nonequilibrium DMFT impurity model to even longer time scale.

We have illustrated the feasibility and efficiency of the MCTDH based impurity solver by applying it to a nonequilibrium Hubbard model on Bethe lattice. The numerical consistency of impurity site double occupancy and real-time Green functions obtained from MCTDH and exact diagonalization proves the successful integration of MCTDH into the nonequilibrium DMFT framework. Furthermore, we have shown the MCTDH based impurity solver can indeed go beyond the capability of exact diagonalization, by providing dynamics of $L = 16$ SIAM, which is not feasible to be solved by exact diagonalization with reasonable computational cost.

Nevertheless, the flexibility offered by the (multi-layer) multiconfiguration time-dependent Hartree formalism in the Fock space second quantization representation can lead to a promising new methodology to faithfully treat equilibrium or nonequilibrium many-body problems with strong correlation, especially for many important model problems in condensed matter physics.

5.3 Bibliography

[1] M. Imada, A. Fujimori, and Y. Tokura, Rev. Mod. Phys. **70**, 1039 (1998).

[2] F. C. Zhang and T. M. Rice, Phys. Rev. B **37**, 3759 (1988).

[3] M. Eckstein and M. Kollar, Phys. Rev. B **78**, 205119 (2008).

[4] R. Huber, F. Tauser, A. Brodschelm, M. Bichler, G. Abstreiter, and A. Leitenstorfer, Nature **414**, 286 (2001).

[5] M. Eckstein and M. Kollar, Phys. Rev. B **78**, 245113 (2008).

[6] M. Rini, N. Dean, J. Itatani, *et al.*, Nature **449**, 72 (2007).

[7] F. Lechermann, A. Georges, A. Poteryaev, S. Biermann, M. Posternak, A. Yamasaki, and O. K. Andersen, Phys. Rev. B **74**, 125120 (2006).

[8] J. K. Freericks, V. M. Turkowski, and V. Zlatić, Phys. Rev. Lett. **97**, 266408 (2006).

[9] A. Georges, G. Kotliar, W. Krauth, and M. J. Rozenberg, Rev. Mod. Phys. **68**, 13 (1996).

[10] H. Aoki, N. Tsuji, M. Eckstein, M. Kollar, T. Oka, and P. Werner, Rev. Mod. Phys. (2014).

[11] C. Gramsch, K. Balzer, M. Eckstein, and M. Kollar, Phys. Rev. B **88**, 235106 (2013).

[12] H. Aoki, N. Tsuji, M. Eckstein, M. Kollar, T. Oka, and P. Werner, arXiv:1310.5329 .

[13] M. H. Beck, A. Jäckle, G. A. Worth, and H.-D. Meyer, Phys. Rev. **324**, 1 (2000).

[14] H.-D. Meyer, F. Gatti, and G. Worth, eds., *Multidimensional Quantum Dynamics: MCTDH theory and its applications* (Wiley-VCH, 2009).

[15] H. Wang and M. Thoss, J. Chem. Phys. **131**, 024114 (2009).

[16] U. Manthe, J. Chem. Phys. **128**, 164116 (2008).

[17] H.-D. M. O. Vendrell, J. Chem. Phys. **134**, 044135 (2011).

[18] P. Schmidt and H. Monien, arXiv:cond-mat/0202046 (2002).

[19] J. K. Freericks, V. M. Turkowski, and V. Zlatić, Phys. Rev. Lett. **97**, 266408 (2006).

[20] L. V. Keldysh, Sov. Phys. JETP **20**, 1018 (1964).

[21] M. Eckstein and M. Kollar, New J. Phys. **12**, 055012 (2010).

[22] K. Balzer and M. Eckstein, Phys. Rev. B **89**, 035148 (2014).

[23] G. A. Worth, M. H. Beck, A. Jäckle, and H.-D. Meyer, The MCTDH Package, Version 8.2, (2000). H.-D. Meyer, Version 8.3 (2002), Version 8.4 (2007), Version 8.5 (2014). See http://mctdh.uni-hd.de.

[24] J. Caillat, J. Zanghellini, M. Kitzler, O. Koch, W. Kreuzer, and A. Scrinzi, Phys. Rev. A **71**, 012712 (2005).

[25] M. Nest, Chem. Phys. Lett. **472**, 171 (2009).

[26] I. S. Ulusoy and M. Nest, J. Chem. Phys. **136**, 054112 (2012).

[27] J. M. Zhang and M. kollar, Phys. Rev. A **89**, 012504 (2014).

[28] J. Caillat, J. Zanghellini, M. Kitzler, O. Koch, W. Kreuzer, and A. Scrinzi, Phys. Rev. A **71**, 012712 (2005).

Chapter 6

Conclusions and Outlook

6.1 Conclusions

The application of ultrafast lasers to initiate, watch and control the motion of electrons and nuclei in real time is a rapid developing field. The recent technological advancement in novel light sources as free electron laser and high harmonic source is pushing the ultrafast physics to cover the femtosecond and attosecond realms, which correspond to the time scale of electronic and nuclear motion.

In this thesis, the ultrafast electronic nuclear dynamics has been studied based on a general theoretical framework of time-dependent formulation of Schrödinger equation, and mixed quantum classical dynamics.

Explicitly, I have studied coupled electronic nuclear non–Born–Oppenheimer dynamics of molecules after valence photoionization and the characterization of the non–Born–Oppenheimer dynamics using transient absorption spectroscopy. In a joint experimental and theoretical study, we have observed and explained the coherent electron hole dynamics, also in the context of coupled electronic nuclear dynamics. Furthermore, I have investigated the electron dynamics in strongly correlated solids, using nonequilibrium DMFT with MCTDH based impurity solver.

It is shown that the direct time–dependent formulation of Schrödinger equation, as a dual formalism to the time–independent treatment for time–independent Hamiltonian, provides intuitive and convenient access to describe the underlying dynamics in atoms, molecules and solids generated by the ultrafast laser pulses.

Electron hole dynamics in gas phase molecules

On the molecular scale, we have shown that the motion of valence electron hole created by the extreme ultraviolet (XUV) photoionization can strongly couple to the motion of nuclei via the non–Born–Oppenheimer effects. Since photoionization is probably the most usual phenomena when molecules are exposed to XUV or x–ray radiation, it is crucial to understand the dynamics of molecular and electronic structure after photoionization, if one uses XUV or x–ray based techniques to study molecules, for example x–ray imaging crystallography, XUV / x–ray pump probe spectroscopy. Besides, the photoionization can also initiate intriguing charge transfer process, as the electrons respond to the electron hole left by the photoionized electron.

Through the non–Born–Oppenheimer coupling enabled electronic relaxation, the energy can flow from the highly excited electrons to the relatively colder nuclei, causing large amplitude vibration or dissociation of the molecule. For the purpose to simulate the coupled electronic nuclear dynamics, the state–of–the–art multiconfiguration time–dependent Hartree (MCTDH) and mixed quantum classical surface hopping methods have been applied.

It is shown from the simulation, that the non–Born–Oppenheimer effect can open new reaction channels, compared to the calculation adopting Born–Oppenheimer approximation. The inter-electronic state transistion induced by nuclear motion can set free wave packet components which are trapped on one of the electronic potential energy surfaces.

For the molecules of medium and large size, the non–Born–Oppenheimer effect can become more pronounced, since the molecular orbitals are more closely packed and start to form quasi continuous band structure, as the scale gradually transit from atomic (wave vector $\mathbf{k} = \mathbf{0}$ in reciprocal space) to molecular (discrete $\mathbf{k}$) and finally into the solid state (continuous $\mathbf{k}$) realm. The intersection between adjacent electronic potential energy surfaces can become the dominant feature for the geometry of a set of potential energy surfaces. Thus the nuclear motion mediated electronic state transition can occur more frequently and may dominate the coupled electronic nuclear dynamics. For this reason, it is necessary to take the non–Born–Oppenheimer effect into account, especially when treating excited state dynamics of medium and large size molecules.

It is further shown that the non–Born–Oppenheimer relaxation process of electron hole created by photoionization can be faithfully probed in real time using core–level transient x–ray absorption spectroscopy technique.

The x–ray photon induces core to valence transition, where a core shell electron is resonantly excited to fill the electron hole initially produced by photoionization. As the

electronic system relaxes by exchanging energy with the nuclei, the electron hole would *float* towards the top of valence shell orbitals, the core to valence transition energy is thus enlarged accordingly, since the energy level of core orbitals is rarely effected by the structure of outer valence shell. In time resolved absorption spectra, this scenario exhibits as a monotonic shift to higher energy, as the relaxation dynamics develops on a time scale of $\sim$ 100 femtoseconds. The spectral intensity, on the other hand, reflects the degree of localization of the electron hole inside the molecule, since the core orbitals are normally localized on individual atoms.

For specific cases, where the electron hole can maintain its coherence for sufficient long time, we have studied the resulted quantum beating of $\sim$ 1 ps in a CO_2^+ cation, which is recorded with XUV pump – IR probe technique in a joint experimental–theoretical study. The quantum beating is explained with the vibronic coupling mechanism, by which an electron hole carrying the superposition of two electronic state characters is sent to motion, driven by the nuclear vibrations. The coherent motion of electron hole in the CO_2^+ cation can be viewed as a charge transfer process, since the electron hole carries electronic character of both π and σ type, the quantum beating implies its shape oscillates between these two types of molecular orbitals. Pictorially, the positive charge of the electron hole would shift from the spatial area along the molecular axis (σ symmetry) to the spatial area surrounding the molecular axis (π symmetry) and vice versa. Together with the explanation of the rotation induced decay of quantum beating and signal baseline, we have given a complete picture to understand the experiment.

Electron dynamics in strongly correlated materials

On the solid state scale, we have further studied the electron dynamics in solids out of equilibrium. The nonequilibrium electron dynamics is initiated and watched using ultrashort laser pulses. Solid state materials that are driven out of equilibrium can reveal intriguing phenomena and hidden phases that are not accessible for solids at equilibrium state. Besides, the time evolution of solid state electronic structure also appears as the scenario for pump probe spectroscopy of solids with ultrashort laser pulses.

On the theoretical side, the nonequilibrium dynamical mean field theory (DMFT) is one of the state-of-the-art framework to treat the time evolution of strongly correlated solid state electronic structure that is driven out of equilibrium.

In this thesis, the multiconfiguration time–dependent Hartree (MCTDH) method has been applied to solve the time evolution of single impurity Anderson model, which is a discretized representation of the complex lattice Hamiltonian describing the strongly

correlated electron system, and is one of core components in the non–equilibrium dynamical mean field theory.

The long time dynamics in the nonequilibrium DMFT formalism implies single impurity Anderson model with increasing number of bath site, which sets the major challenge to develop impurity solver, since one would rapidly hit the computational barrier due to notorious dimension scaling of electronic configuration space.

A promising way braving this challenge is to apply the MCTDH method, which is one of the most efficient methods to handle time–dependent Schrödinger equation. We have shown that MCTDH can be successfully embedded into the nonequilibrium DMFT framework by providing two-time Green functions which are the key quantities for the DMFT self-consistent iteration procedure. The reduction of configuration space dimension brought by MCTDH may enable the access to long time dynamics, which can be crucial in simulation of the pump–probe experiment of strongly correlated materials.

The particular advantage in the Fock space MCTDH formalism employed in this thesis, which guarantees the fermionic symmetry of electronic wave functions in MCTDH mode combination, would enable further extension to more efficient ML-MCTDH scheme, which can definitely push the limit of nonequilibrium DMFT to even longer time scale dynamics.

6.2 Outlook

Electron hole dynamics in gas phase molecules

So far in this thesis, the electron hole considered is in the shallow outer valence shell subjected to photoionization by sub-keV extreme ultraviolet (soft x–ray) radiation. In many x–ray physics applications, for example the x–ray crystallography, the photon energy lies however in the keV or even hard x–ray (> 10 keV) range. When the molecule is exposed to x–ray photons, the core hole creation becomes the dominant process. The electron hole in the deep core shell of molecules can initiate various secondary cascade processes of electrons, for example Auger decay, which build the theatre for abundant dynamics involving coupled motion of electrons and nuclei.

To treat the deep core shell electron hole and the dynamical processes initiated by it, one needs to have a good electronic structure tool, which can appropriately describe the electron correlation, since e.g. the valence electrons would immediately respond to the presence of a deep core hole in order to screen its positive charge. In certain cases, the x–ray photon brings the core shell electron into the quasi-continuum orbitals instead

of directly into the continuum. In this case, one needs a reasonable discretization of quasi continuum states, which may imply tremendous computational effort. Exploring the electronic structure theory involving deep core shell excitation and core hole creation could be a promising direction for the following development in the near future.

With the reliable electronic structure in hand, one is able to construct physical observables, in order to simulate the recorded spectra or signals in the experiment, and to interpret the underlying mechanism that the signals reveal.

Subject to the time–resolved x–ray spectroscopy, which is most closely related to the focus of this thesis, and to the young and rapidly developing field of XFEL science, the non–linear x-ray spectroscopy could be a promising candidate for the following work.

The non–linear x-ray spectroscopy can provide further possibilities to resolve the coupled electronic nuclear dynamics in real time. A good example is the resonant inelastic x-ray scattering (RIXS) technique. The RIXS process corresponds a photon-in photon-out mechanism, thus would not be limited to the study of thin materials, which is a typical drawback for photoelectron based technique due to the relatively short mean free path of electrons in the material.

The high energy resolution down to meV provided by modern RIXS spectrometers allows one to access not only the electronic dynamics on a delicate manner, for example the electron spin flip, but also the nuclear dynamics, for example nuclear vibrations. Because the x-ray free electron laser can enable the non–linear x–ray spectroscopy to be carried out with femtosecond x–ray laser pulses, one can add the time dimension to the RIXS spectra, which gives ideally a molecular movie.

Moreover, the multidimensional resonant spectroscopy for molecules, which was originally developed in the optical regime by S. Mukamel, has been recently brought into the realm of x–ray (Ref: S. Mukamel *et al.* Annu. Rev. Phys. Chem. 64, 101 (2013)), since this type of experiments are enabled by the pulses produced from new free–electron laser facilities and high–harmonic generation X–ray light sources, which are short and intense enough.

With the multidimensional resonant spectroscopy, one can trigger valence–electron motions impulsively by core excitations and monitor with high spatial and temporal resolution. The inherent non–linearity of this technique renders it possible to probe quantum coherence and correlations of valence electrons and electron holes, rather than the charge density alone, which is analogous to the multidimensional spectroscopy in the visible regime which resolves vibrational motions of molecules.

Thus I would envision plan to study the x–ray multidimensional resonant electronic

spectroscopy.

On the methodological side, it should be a promising direction to develop of novel theoretical schemes to treat non–Born–Oppenheimer dynamics based on the exact factorization representation introduced in chapter 2.

Electron dynamics in strongly correlated materials

The strongly correlated solids have intriguing electronic structure, in which the many–body Coulomb correlation between electrons dominate the electronic interactions. Due to the pronounced many–body effects in the strongly correlated solids, their electronic structure cannot be correctly described by energy band theory based on independent particle picture.

The dynamical mean field theory is a state-of-the-art framework that is developed solve the electronic structure of strongly correlated solids beyond the independent particle picture of energy band theory.

In this thesis, we have introduced the MCTDH method to solve the DMFT impurity problem that is mapped from a time–dependent model Hubbard Hamiltonian on the Bethe lattice, which is the first and important step towards simulating the solid state pump–probe experiments. We would further embed the ML-MCTDH scheme into the DMFT framework, which should improve the efficiency on the basis of present DMFT–MCTDH impurity solver.

It is a natural direction for following work to bring the MCTDH-DMFT scheme to the *ab initio* simulation of real time dynamics of strongly correlated materials beyond the independent particle picture provided by energy band theory.

Up to date, most efforts in the *ab initio* DMFT community have been devoted to solve the static electronic structure for strongly correlated solids in equilibrium. Among various techniques to treat electron correlations in solids, the self-consistent density functional theory – dynamical mean field theory (SC–DFT–DMFT) is one of the state-of-the-art methods (Ref: F. Lechermann *et al.*, Phys. Rev. B, 74, 125120 (2006)). In SC–DFT–DMFT, certain single–particle electronic orbitals near Fermi surface are projected into a *correlated subspace*, in which the pronounced many–body correlation effects can be treated in a non–perturbative manner using DMFT, the non–perturbative correction to the electron density is then fed to the DFT. The electronic structure is determined when self–consistency between DFT and DMFT is reached.

So far we are able to solve the nonequilibrium DMFT problem with time–dependent electron hopping term $t_{ij}(t)$ and on–site Coulomb interaction $U(t)$, it would be an attractive

plan to incorporate DFT component to the nonequilibrium DMFT scheme, such that one is able to simulate experiment on specific materials with pronounced electron correlation, for example perovskite, which is driven out of equilibrium and probed by the ultrashort laser pulses.

It has been shown in previous experiments by M. Rini *et al.*, that light can induce phase transitions in strongly correlated solids, for example insulator to metal transition, by the photon coupling to electronic and nuclear degrees of freedom (Ref: M. Rini *et al.*, Nature, 449, 72 (2007)).

In a recent experiment by the group of Prof. Andrea Cavalleri (Ref: S. Kaiser *et al.*, Phys. Rev. B, 89, 184516 (2014)), ultrashort terahertz pulses have been used to induce a transient nonequilibrium phase in high-T_c superconductors via coherent control of lattice phonon states that could very likely be superconducting over a fraction of the solid at room temperature $T_c \sim 300$ K with a lifetime of several picoseconds. With *ab initio* time–dependent DFT–DMFT framework, which can be developed based on our nonequilibrium DMFT–MCTDH program, one could expect to clarify the delicate photon–phonon–electron interaction that induces the possible room temperature superconducting phase transition phenomena, which remains up-to-date a hypothetical explanation to the highly coherent transport phenomena observed from a photoinduced transient state of $YBa_2Cu_3O_{6+\delta}$ cuprates.

Overall perspective

From molecular to solid state scales, the novel ultrafast and ultrabright light sources, such as x–ray free electron lasers, open the possibility to make movies in real time and real space, in which nuclei and electrons are the actors in the microscopic world. With the theoretical development in describing the real time nuclear and electronic dynamics, and their interaction with light pulses that initiate and probe the dynamics, the joint experimental and theoretical effort would make the dream for *molecular movies* soon come true.

Acknowledgement

First of all, I am deepestly grateful to Dr. Oriol Vendrell for accepting the risk of taking me as his first Ph.D. student, to Prof. Robin Santra for co-supervising me as his Ph.D. student, and to Prof. Jochen Küpper for being my Ph.D. mentor. They guide me safely through the vibrant fields of ultrafast science. Their inspiring enthusiasm and devotion have made the three years of my Ph.D. the most productive period of my academic life.

I want to express my deepest gratitude to Prof. Hans-Dieter Meyer, Dr. Nikita A. Medvedev, Dr. Stefan U. Pabst and Dr. Karsten Balzer for their roles both as friends and as mentors to me in my life, I will never forget their kind hearts and friendship.

A special thanks goes to Dr. Mohammed El-Amine Madjet, Dr. Karsten Balzer, Dr. Nikita A. Medvedev, Dr. Stefan U. Pabst, Yi-Jen Chen, Henry Timmers, Prof. Martin Eckstein and Prof. Arvinder Sandhu, for the most interesting scientific discussions in the work accomplished by fruitful collaborations.

I also want to thank many colleagues at CFEL theory division, Jan Malte Slowik, Yi-Jen Chen, Victor Tkachenko, Pankaj Kumar Mishra, Antonia Karamatskou, Dao-Cheng Wang, Dmitrii I. Shedogubov, Malik M. Abdullah, Saqib Muhammad, Abid Hussain, Jason Khadka, Mirco Grösser, Mario Arkenberg, Berit Heiser, Otfried Geffert, Dr. Gopal Dixit, Dr. Ya-Jiang Hao, Dr. Sang-Kil Son, Dr. Zoltán Jurek, Dr. Vikrant Saxena, Dr. Daria Popova, Dr. Arina Sytcheva, Dr. Robert Thiele and Prof. Beata Ziaja-Motyka. Without their constant patience to answer my questions and to help me on difficult problems in physics, I could not have acquired enough knowledge to accomplish my Ph.D. thesis.

I am very grateful to Shih-Hsuan Chia, Wei Liu, Zhi-Peng Huang, Khalid Siddiqui, Peter Krötz, Nele Müller, Jens Kienitz, Thomas Kierspel, Claudia Busch, Dr. Hai-Yun Liu, Dr. Song-Bin Zhang, Dr. Shao-Bo Fang, Dr. Feng-Lin Wang, Dr. Guo-Qing Chang, Dr. Yuan-Pin Chang, Dr. Daniele Nicoletti, Prof. Henry Chapman, Prof. Franz X. Kärtner and many other colleagues at CFEL, as well as classmates of IMPRS graduate school, who have never hesitated to offer me warm-hearted help at all time.

It is hard to imagine that I could be smoothly approaching my Ph.D. degree without the help of IMPRS coordinators Anja Bleidorn and Dr. Sonia Utermann, as well as the always warm-hearted help of Heiser Berit, Irmtraud Kleine, Bärbel Wegener from CFEL secretariat and Steffi Killough, Bernd Krempl, Nicole Kosian from DESY international office. For their kind heart I am very much obliged to express my gratitude.

I would also thank Dr. Oriol Vendrell and Dr. Nikita A. Medvedev for proof reading the thesis.

On the personal side, I have experienced great support from my parents You-Qiang Li and Li-Ke Zeng, as well as from all my dear family members. Most importantly, I want to thank my family for so many things. I am deeply indebted to my parents, who ignited my scientific interest by exciting stories of scientists pioneering bravely into the unknown areas of natural science. My dear family members and their love are and will be always accompanying me during my whole life time.

Eidesstattliche Versicherung
Declaration on Oath

Hermit erkläre ich an Eides statt, dass ich die vorliegende Dissertationsschrift selbst verfasst und keine anderen als die angegebenen Quellen und Hilfsmittel benutzt habe.

I hereby declare, on oath, that I have written the present dissertation by my own and have not used other than the acknowledged resources.

Hamburg, den Unterschrift